Development of a Linear Paul Trap for Ba-tagging in a nEXO upgrade

Hussain Rasiwala

A THESIS SUBMITTED IN PARTIAL FULFILLMENT OF THE REQUIREMENTS FOR THE DEGREE OF

Master of Science

Department of Physics
McGill University
Montréal, Québec, Canada

November 2, 2021

Abstract

The current research on neutrinos is motivated by the long-standing question of matter-antimatter asymmetry and the search for dark matter. We look at the different neutrino-related phenomena and interactions to better understand their properties and nature, i.e., are they Dirac or Majorana particles. One such important phenomenon is that of neutrinoless double-beta decay ($0\nu\beta\beta$). It is a hypothetical decay mechanism that, if observed, would prove that neutrinos are Majorana particles, which will have pronounced and far-reaching consequences for our understanding of the universe. nEXO is a tonne-scale experiment that aims at searching for $0\nu\beta\beta$ decay in 5-tonnes of liquid xenon enriched to 90% in ^{136}Xe, an isotope of xenon that undergoes double-beta decay. $0\nu\beta\beta$ decay is a rare decay mode yet to be observed, with only a handful of events expected per year with detectors of volume on the tonne scale. To reduce environmental backgrounds even further, the Ba-tagging technique is being developed as a potential future upgrade to nEXO for detecting the daughter isotope ^{136}Ba, resulting from the double-beta decay of ^{136}Xe. As part of the Ba-tagging development, a linear Paul trap is being developed to enable the cooling, trapping, and bunching of ions extracted from the detector volume. Here, the detection of barium ions is performed using fluorescence laser spectroscopy on the trapped ions. After identification, the barium ions are transferred to a mass spectrometer for precise determination of their mass. This thesis covers an account of the operating principle of the setup, simulation of the ion optics, and initial commissioning measurements using the setup.

Abrégé

Les recherches actuelles sur les neutrinos sont motivées par la question de longue date de l'asymétrie matière-antimatière et la recherche de la matière noire. Nous examinons les différents phénomènes et interactions liés aux neutrinos afin de mieux comprendre leurs propriétés et leur nature, c'est-à-dire, s'ils sont des particules Dirac ou Majorana. L'un de ces phénomènes importants est celui du $0\nu\beta\beta$. Il s'agit d'un mécanisme de désintégration hypothétique qui, s'il était observé, aurait des conséquences importantes et de grande portée sur notre compréhension de l'univers. nEXO est une expérience à l'échelle de la tonne qui recherche la désintégration $0\nu\beta\beta$ dans 5-tonnes de xénon enrichi à 90% en ^{136}Xe, un isotope du xénon qui subit une double désintégration bêta. La désintégration $0\nu\beta\beta$ est prévue comme étant un événement rare qui n'a pas encore été observé. Vue sa rareté, très peu d'événements par an sont prédits avec des détecteurs d'un volume de l'ordre de la tonne. Afin de réduire le bruit de fond de l'expérience, la technique de marquage du Ba est une amélioration proposée pour nEXO qui permettra de détecter le ^{136}Ba résultant de la désintégration bb du ^{136}Xe. Dans le cadre de l'ensemble de marquage du Ba, un piège linéaire Paul est en cours de développement pour permettre le refroidissement, le piégeage et le regroupement des ions extraits du volume du détecteur. Dans le piège, la détection des ions baryum est réalisée par spectroscopie laser à fluorescence sur les ions piégés. Après l'identification, les ions de baryum sont transférés vers un spectromètre de masse pour une détermination précise de leur masse. Cette thèse couvre le principe de fonctionnement de l'installation, la simulation de l'optique ionique, et les premières mesures de test utilisant l'installation mise en service.

Acknowledgements

First and foremost, I would like to thank Prof. Thomas Brunner for the opportunity to work under him and his continued guidance, without which this thesis would not have been possible. Despite his busy schedule, he always made time for troubleshooting and discussions. I want to thank Dr. Christopher Chambers and Mr. Xiao Zhang for their continued support at every assembly and commissioning stage. I could always look to them for help, confirmation and received much valuable feedback. Mr. Eamon Egan greatly supported the development of electronics, and his expertise in the area was invaluable. I want to thank Dr. Yang Lan for all his work in developing the current setup design, on which this thesis further builds on and for providing his simulations on the linear Paul trap (LPT) prototype. I want to thank Mr. Xiao Zhang for preparing drawings of the LPT setup and the machine shop at Université de Montréal (UdeM) for carefully machining the LPT setup components. I want to thank Mr. Kevin Murray for helping align the LPT setup and troubleshooting the LPT simulations.

Finally, I would like to thank my parents and my brother for always being there for me. I could not have gotten to this point without their continued support.

Contribution of Authors

The entire thesis is written by the author. Additionally, all data analysis and results presented here were done by the author unless specified otherwise.

The prototypes of the presented Linear Paul Trap (LPT) setup were designed by Dr. Yang Lan as part of his Ph.D. thesis and later modified by him and Mr. Xiao Zhang for the current setup. Most of the electronics used in the discussed setup were designed at McGill University by Eamon Egan, including the circuits for DC-coupled RF and the voltage switches for the LPT-buncher.

The LPT setup was assembled by the author together with Mr. Xiao Zhang. Xiao Zhang also assembled and installed the helium inlet into the vacuum system. Dr. Christopher Chambers and the author connected the helium line on the atmospheric side. The SIMION simulation of the LPT was initially prepared by Yang Lan (for his prototype at UBC). The author later modified it to optimize LPT potentials to study ion bunch properties, trapping, and ejection timing. The LabVIEW programs used in controlling waveform generator and readout for pressure gauges were written by the author. Mr. Kevin Murray developed most of the program for controlling the timing of voltage switches.

Finally, the ion source assembly is based on previous ion source designs at the Brunner Neutrino Lab (BνL) except for a quadrupole bender, which the author designed and optimized in SIMION simulations.

Contents

List of Figures

List of Acronyms

$0\nu\beta\beta$	neutrinoless double-beta decay.
$\mathbf{2}\nu\beta\beta$	Two neutrino double-beta decay.
DC	Direct Current.
FPGA	Field Programmable Gate Array.
ICB	Ion Cooler and Buncher.
LAS	Laser ablation source.
LPT	Linear Paul Trap.
LXe	liquid xenon.
MRTOF-MS	multiple-reflection time-of-flight mass spectrometer.
PMNS	Pontecorvo-Maki-Nakagawa-Sakata.
PMT	photomultiplier.
QMF	Quadrupole Mass Filter.
RF	Radio Frequency.
SiPM	silicon photomultiplier.
SM	Standard Model.
TMP	turbo-molecular pumps.
TPC	Time Projection Chamber.
UHV	Ultra-High Vacuum.
VUV-SiPM	Vacuum Ultraviolet SiPM.

Chapter 1

Introduction

1.1 The Neutrino

Neutrinos are charge-neutral leptons that occur in nature in three flavors (ν_e, ν_μ, ν_τ) corresponding to the three charged leptons they weakly interact with, i.e., electron (e), muon (μ), and tau (τ). Neutrinos are the most abundant known matter particles in nature and the second most abundant particles after photons. One hundred billion is an approximate figure typically quoted, as how many neutrinos pass through our thumbnail per second [1]. Despite their abundance, we cannot feel their presence because they rarely interact with matter; for example, less than 10 neutrinos interact throughout a human lifetime. 'Elusive' is a term that has almost become a synonym for neutrinos in particle physics [2]. Neutrinos do not interact via strong nuclear force or electromagnetic forces since they have no charge; they only interact via weak interactions. They do feel gravitation, but as we know now, they are extremely light [3, 4]. Although this makes studying them extremely difficult, it enables neutrinos to probe physics in ways that are not possible with other particles [5, 6].

The conception of these ghostly particles took place in the 1930s as part of Wolfgang

Pauli's famous 'desperate remedy' to preserve energy and momentum conservation [7]. Reines and Coven later detected neutrinos (more specifically, electron antineutrinos) in their experiment, 'Project Poltergeist' in 1956 [8]. Following this discovery, several experiments were devised to confirm this observation. The muon neutrino was discovered in 1962 at Brookhaven National Lab using the first-ever neutrino beam [9, 10]. The third charged lepton, the τ particle, was first detected at the Stanford Linear Accelerator Center (SLAC) in 1975 [11], which then lead scientist to expect another neutrino flavor as an elusive partner of the heavy τ particle. The next major discovery was the measurement of neutrino rate from the sun by the Homestake experiment. It was the first experiment ever to detect solar neutrinos [12]. The experiment observed a difference between the predicted and observed solar neutrino rates (specifically ν_e), giving rise to the Solar neutrino problem [13]. This inspired further research in the neutrino producing mechanism in the Sun and the properties of the neutrinos being detected.

1.2 Neutrino Oscillations

The Homestake experiment failed to verify the theoretical predictions by consistently measuring about one-third of the expected number of neutrino events [13]. Several experiments following the Homestake experiment, such as Kamiokande-II [14], also observed large deviations from the expected count. It was later found that the difference between observed and expected neutrino fluxes matched the excess in other flavor channels; for example, a deficit in electron-neutrinos would appear as excess in muon or tau neutrino count. This indicated the change of neutrino flavor; a phenomenon now referred to as neutrino oscillation. Results from experiments such as Super-Kamiokande [15], and KamLAND [16], showed evidence of the possibility of neutrino oscillations through different neutrino sources. SNO experiment confirmed neutrino oscillation by being able to detect all three neutrino flavors, unlike past experiments [17], thus giving irrefutable proof

of the massive nature of neutrinos.

In the framework of neutrino oscillations, neutrinos change their flavor between $(\nu_e, \nu_\mu, \nu_\tau)$ as they travel. The major implication derived from this observation is that neutrinos have a non-zero mass, contrary to the assumption in the Standard Model (SM) where neutrinos were massless. The physics of neutrino oscillation is derived from the mixing matrix, called the Pontecorvo-Maki-Nakagawa-Sakata (PMNS) matrix [18], which depends on oscillation parameters like the mixing angles $(\theta_{12}, \theta_{13}, \theta_{23})$, the CP phase (δ_{CP}) and Majorana phases (α, β) [19]. In this formalism, flavor eigenstates $(\nu_e, \nu_\mu, \nu_\tau)$ and mass eigenstates (ν_1, ν_2, ν_3) of the neutrinos are related by the PMNS matrix as follows:

$$\begin{pmatrix} \nu_e(t) \\ \nu_\mu(t) \\ \nu_\tau(t) \end{pmatrix} = U \begin{pmatrix} \nu_1(t) \\ \nu_2(t) \\ \nu_3(t) \end{pmatrix},$$

where U is the PMNS matrix given as the product of three rotation matrices:

$$\begin{aligned} U &= \begin{pmatrix} 1 & 0 & 0 \\ 0 & c_{23} & s_{23} \\ 0 & -s_{23} & c_{23} \end{pmatrix} \begin{pmatrix} c_{13} & 0 & s_{13}e^{-i\delta} \\ 0 & 1 & 0 \\ -s_{13}e^{i\delta} & 0 & c_{13} \end{pmatrix} \begin{pmatrix} c_{12} & s_{12} & 0 \\ -s_{12} & c_{12} & 0 \\ 0 & 0 & 1 \end{pmatrix} P \\ &= \begin{pmatrix} c_{12}c_{13} & s_{12}c_{13} & s_{13}e^{-i\delta} \\ -s_{12}c_{23} - c_{12}s_{23}s_{13}e^{i\delta} & c_{12}c_{23} - s_{12}s_{23}s_{13}e^{i\delta} & s_{23}c_{13} \\ s_{12}c_{23} - c_{12}c_{23}s_{13}e^{i\delta} & -c_{12}s_{23} - s_{12}c_{23}s_{13}e^{i\delta} & c_{23}c_{13} \end{pmatrix} P. \end{aligned}$$

Here $c_{ij} = \cos\theta_{ij}$, $s_{ij} = \sin\theta_{ij}$ and P is either equal to unit matrix for Dirac neutrinos or

carries information about Majorana phases (α, β) as diagonal matrix:

$$P_{majorana} = \begin{pmatrix} 1 & 0 & 0 \\ 0 & e^{i\alpha} & 0 \\ 0 & 0 & e^{i\beta} \end{pmatrix}, P_{dirac} = \begin{pmatrix} 1 & 0 & 0 \\ 0 & 1 & 0 \\ 0 & 0 & 1 \end{pmatrix}.$$

Using this transformation, we can obtain the neutrino mass matrix M_ν:

$$M_\nu = U \begin{pmatrix} m_1 & 0 & 0 \\ 0 & m_2 & 0 \\ 0 & 0 & m_3 \end{pmatrix} U^T,$$

where (m_1, m_2, m_3) are are neutrino masses corresponding to the mass eigenstates (ν_1, ν_2, ν_3).

The neutrino oscillation probability can be derived by writing the neutrino flavor eigenstates as a superposition of mass eigenstates weighted by PMNS matrix elements as

$$\nu_\alpha = \sum_{k=1}^{3} U_{\alpha k} \nu_k, \qquad (\alpha = e, \mu, \tau; k = 1, 2, 3). \tag{1.1}$$

Re-writing them in bracket notation gives

$$|\nu_\alpha(t)\rangle = \sum_{k=1}^{3} U_{\alpha k} |\nu_k(t)\rangle . \tag{1.2}$$

The evolution of neutrino mass eigenstates with time is given by Schrodinger equation with no potential,

$$i\frac{\partial}{\partial t} |\nu_k(t)\rangle = E_k |\nu_k(t)\rangle \rightarrow |\nu_k(t)\rangle = e^{-iE_k t} |\nu_k\rangle . \tag{1.3}$$

Using results from Eqn. 1.3 and inverting Eqn. 1.1, the flavor eigenstate at time t can be

expressed as a superposition of flavor eigenstates as

$$|\nu_\alpha(t)\rangle = \sum_{k=1}^{3} U_{\alpha k} e^{-iE_k t} |\nu_k\rangle \,, \tag{1.4}$$

$$= \sum_{\beta=e,\mu,\tau} \left(\sum_{k=1}^{3} U_{\alpha k} e^{-iE_k t} U^*_{\beta k} \right) |\nu_\beta\rangle \,. \tag{1.5}$$

Eqn. 1.5 can be used to calculate the probability P of transition $(\nu_\alpha \to \nu_\beta)$

$$P_{\nu_\alpha \to \nu_\beta}(t) = |\langle \nu_\beta | \nu_\alpha(t) \rangle|^2 = \sum_{k,j=1}^{3} U_{\alpha k} U^*_{\beta k} U^*_{\alpha j} U_{\beta j} e^{-i(E_k - E_j)t}, \tag{1.6}$$

where (α, β) represent indices corresponding to two of the three neutrino flavors and (k, j) indices corresponding to the mass eigenstates. Since it is known that the neutrino masses are of the order of eV [20], detected neutrinos are ultrarelativistic. In this limit, we can write:

$$E_k - E_j = \frac{\Delta m^2_{kj}}{2E}, \qquad (E \to \bar{p}).$$

Replacing time t in terms of the distance traveled, specifically, the distance between source and detector L in Eqn. 1.6 gives the oscillation probability as a function of neutrino energy E, distance traveled L and squared mass differences Δm^2_{kj},

$$P_{\nu_\alpha \to \nu_\beta}(t) = \sum_{k,j=1}^{3} U_{\alpha k} U^*_{\beta k} U^*_{\alpha j} U_{\beta j} exp\Big(- i \frac{\Delta m^2_{kj}}{2E} L \Big).$$

Substituting the oscillation parameters and other experiment-specific parameters, the measured oscillation probability can be used to obtain bounds on the squared mass differences [21]. The squared mass differences $(|\Delta m^2_{21}|, |\Delta m^2_{31}|)$ give the differences in the neutrino masses but do not define the hierarchy, i.e., whether $\Delta m_{ij} < 0$ or $\Delta m_{ij} > 0$. Thus, the current framework allows for two types of neutrino mass orderings: normal ordering $(m_1 < m_2 < m_3)$, inverted ordering $(m_3 < m_1 < m_2)$. The two orderings result

from the convention adopted that $\Delta m^2_{21} > 0$, leaving $m^2_{31} > 0$ or $m^2_{31} < 0$. Fig. 1.1 shows a representation of the two possible ordering along with current estimates of the mass differences. Neutrino oscillations are discussed in greater detail in [18, 22, 23].

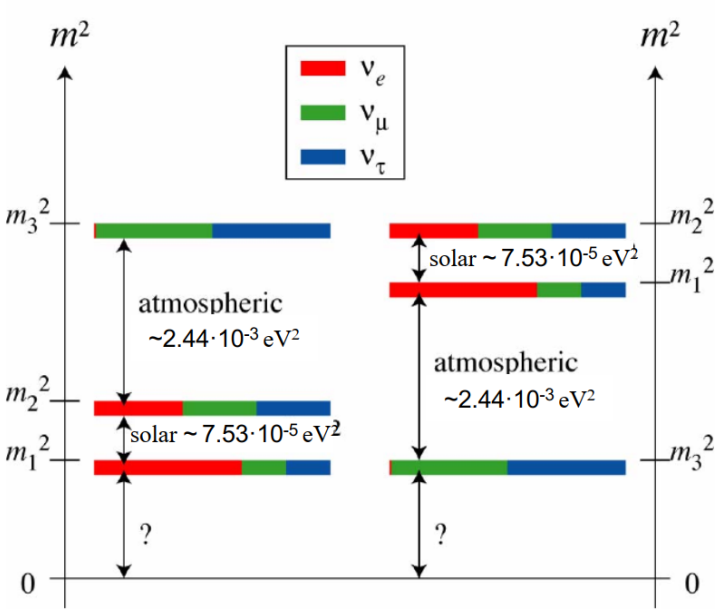

Figure 1.1: Schematic showing the different neutrino mass orderings. Based on the convention followed, $m^2_{21} > 0$ is kept fixed with $\Delta m^2_{31} > 0$ or $\Delta m^2_{31} < 0$ giving rise to two ordering schemes: normal ordering (left) and inverted ordering (right). The schematic shows the current values of the squared mass differences from experiments looking for neutrino oscillations in solar and atmospheric neutrinos. The absolute mass scale remains undermined, indicated by the '?' (Fig. from [24]).

In this past decade, various experiments (K2K [25], MINOS [26], T2K [27], Daya Bay [28], NOvA [29], etc.) have probed into many of these oscillation parameters. Bounds on neutrino masses are also provided by direct kinematic searches such as the KATRIN experiment [20] and from cosmology [30]. However, the neutrino mass scale and mass hierarchy remain unknown to date.

1.3 Neutrinoless Double Beta Decay

In the SM, neutrinos are assumed to be massless [31]. The reasoning behind this stems from the fact that only left-handed neutrinos were detected. The handedness or chirality of neutrinos is related to the direction of their spin relative to their motion. At the time SM was developed, it was known that neutrinos were left-handed and anti-neutrinos right-handed [32], and hence neutrinos were assumed massless like photons. It was later proven incorrect by the observation of neutrino oscillations which are only possible for non-zero neutrino masses. As a consequence of this, there is no hard requirement for neutrinos to be only left-handed. As shown in Fig. 1.2, for non-zero neutrino mass, based on the reference frame, a neutrino can be both observed to be either left-handed or right-handed. This opens the possibility for neutrinos to be Majorana particles [33]. As Majorana particles, neutrinos would be their own antiparticle. The search for the Majorana nature of neutrinos is currently being pursued via the search of neutrinoless double-beta decay ($0\nu\beta\beta$).

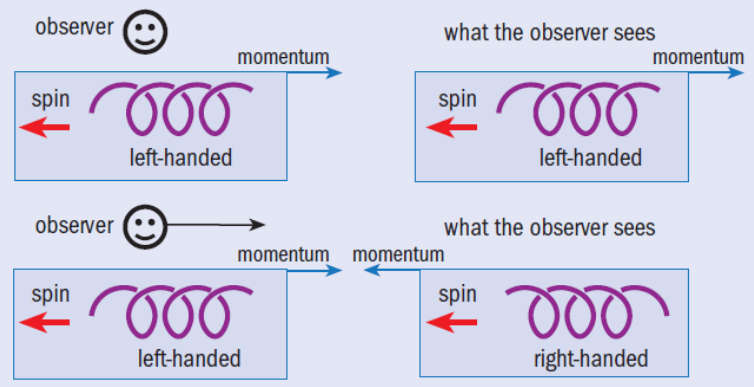

Figure 1.2: Schematic showing the effect of non-zero neutrino mass on its observed chirality. When observed from a reference frame moving faster than the neutrino, it appears as right-handed instead of conventional left-handed (Fig. from [34]).

Two neutrino double-beta decay ($2\nu\beta\beta$) is a second-order weak nuclear decay observed in even-even type nuclei such as ^{48}Ca, ^{76}Ge and ^{136}Xe to name a few examples [35]. In

these nuclei, single-beta decay is energetically forbidden, instead the nucleus undergoes two (simultaneous) beta decays, as shown for a ^{136}Xe nucleus

$$^{136}_{54}\mathrm{Xe} \longrightarrow {}^{136}_{56}\mathrm{Ba}^{+2} + 2e^- + 2\bar{\nu}_e + Q_{\beta\beta}. \tag{1.7}$$

The ^{136}Xe nucleus decays to ^{136}Ba under the emission of two electrons, two electron-antineutrinos and energy (which will henceforth be referred to as $Q_{\beta\beta} = 2458\,\mathrm{keV}$) in the form of their kinetic energy. Fig. 1.3 shows the energy levels of ^{136}Xe; note how a single beta decay to ^{136}Cs is energetically forbidden.

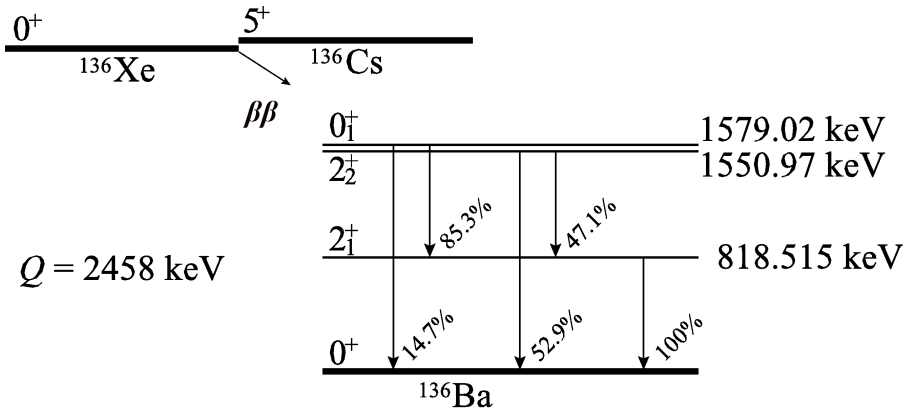

Figure 1.3: Schematic showing the energy level of ^{136}Xe and its decay products. The energy level for ^{136}Cs is higher than its parent nucleus, hence, ^{136}Xe undergoes double beta decay to ^{136}Ba rather than the forbidden single β-decay to ^{136}Cs (Fig. from [36]).

Neutrinoless double-beta decay ($0\nu\beta\beta$) is a special case of this nuclear decay where the double beta decay results in the release of two electrons without any accompanying antineutrinos. Using the example of ^{136}Xe ,

$$^{136}_{54}\mathrm{Xe} \longrightarrow {}^{136}_{56}\mathrm{Ba}^{+2} + 2e^{-1} + 0\bar{\nu}_e + Q_{\beta\beta}. \tag{1.8}$$

This decay is forbidden in the SM as it violates lepton number conservation. Fig. 1.4

compares the $2\nu\beta\beta$ and $0\nu\beta\beta$ decays. The Feynman diagram for $0\nu\beta\beta$ decay shows the recapture/annihilation of the antineutrino from one beta decay vertex with another, resulting in a lepton number violation ($\Delta L = +2$).

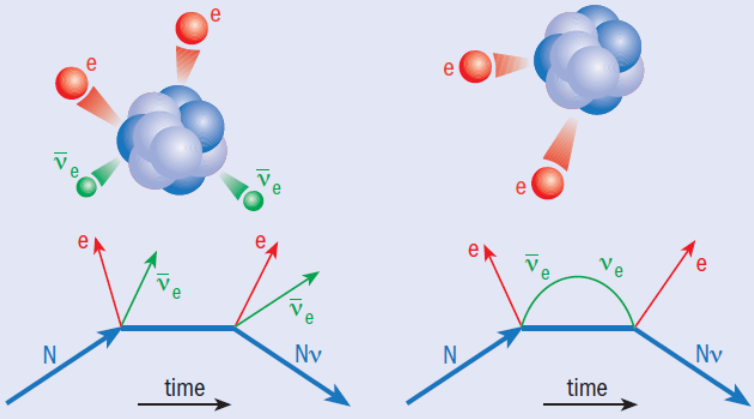

Figure 1.4: Comparing Feynman diagrams of $2\nu\beta\beta$ decay (left) with $0\nu\beta\beta$ decay (right). In neutrinoless double-beta decay case, the emitted antineutrino ($\bar{\nu}_e$) is annihilated/recaptured (shown as an exchange of a virtual particle between vertices on the right), resulting in no neutrino emission, building on the relative handedness argument from Fig. 1.2 (Fig. from [34]).

The observation of such an event would have far-reaching consequences on our understanding of these elusive neutrinos and the evolution of the universe [37]. $0\nu\beta\beta$ decay implies that neutrinos are Majorana particles and is proof of lepton number violation, which otherwise is an assumed conservation law in the SM. $0\nu\beta\beta$ decay thus could help explain why the universe we live in is matter-dominated while the Big Bang should have resulted in equal quantities of matter and antimatter [38].

Several international experiments are searching for $0\nu\beta\beta$ decay by using large quantities of double-beta decaying isotopes, like ^{76}Ge (GERDA [39]), ^{136}Xe (EXO-200 [40]). Half-life limits for some of the current experiments, using different $0\nu\beta\beta$ isotopes are listed in Table 1.1.

Isotope	Sensitivity ($\times 10^{25}$ years)	$T_{1/2}^{0\nu\beta\beta}$ ($\times 10^{25}$ years)	$m_{\beta\beta}$ (eV)	Experiment
^{48}Ca	1.8×10^{-3}	$> 5.8 \times 10^{-3}$	$< 3.5 - 22$	ELEGANT VI [41]
^{76}Ge	18	> 18	$< 0.08 - 0.18$	GERDA [39]
^{130}Te	2.8	> 2.2	$< 0.09 - 0.31$	CUORE [42]
^{136}Xe	5.0	> 3.5	$< 0.09 - 0.29$	EXO-200 [43]

Table 1.1: Sensitivity limits of current experiments along with their $0\nu\beta\beta$ decay half-life ($T_{1/2}^{0\nu\beta\beta}$) and Majorana neutrino mass ($m_{\beta\beta}$) estimates.

The current experiments have been able to probe $0\nu\beta\beta$ decay half-life to $\sim 10^{26}$ years, but so far have not discovered $0\nu\beta\beta$ decay. The massive detector quantity requirement for the next generation experiments can be justified through the following equation:

$$N = \ln 2 \frac{N_a}{W} \left(\frac{a\epsilon M t}{T_{1/2}^{0\nu\beta\beta}} \right) \text{(from [44])}. \tag{1.9}$$

Here, $T_{1/2}^{0\nu\beta\beta}$ is the half-life of $0\nu\beta\beta$ decay, (N_a,W,a) are Avogadro's number, molar mass, and isotopic abundance of source, ϵ is the detection efficiency, and t is the duration of the data taking. Eqn. 1.9 shows that to reach higher $0\nu\beta\beta$ decay half-life sensitivity, which depends on number of candidate events N, the detector mass M needs to be increased.

The half-life of $0\nu\beta\beta$ decay ($T_{1/2}^{0\nu\beta\beta}$) depends on several factors like phase space factor G, nuclear matrix element M and effective Majorana mass $m_{\beta\beta}$

$$T_{1/2}^{0\nu\beta\beta} = \left(G|M|^2 \langle m_{\beta\beta} \rangle \right)^{-1} \approx 10^{27-28} \left(\frac{0.01\text{eV}}{\langle m_{\beta\beta} \rangle} \right)^2 \text{(from [44])}. \tag{1.10}$$

Based on our current values for (G, M), to probe into the sub-eV neutrino mass scale (0.01eV in Eqn. 1.10), the detectors need to reach the 10^{28} years sensitivity limit for $0\nu\beta\beta$ half-lives [45, 46]. Thus the next generation experiments require to push the current limit of

$T_{1/2}^{0\nu\beta\beta} \sim 10^{26}$ years sensitivity by another two orders of magnitude or discover $0\nu\beta\beta$. Among the upcoming experiments, the nEXO experiment is a tonne scale experiment designed to reach this half-life limit after ten-year of data-taking.

1.4 nEXO Experiment

nEXO is a next-generation experiment, the successor to the EXO-200 experiment [43], that searches for $0\nu\beta\beta$ decay in liquid xenon (LXe). The nEXO detector design consists of a Time Projection Chamber (TPC) containing five tonnes of LXe, 90% enriched in the isotope ^{136}Xe.

The TPC is located at the center of a refrigerant-filled (HFE 7000) inner cryostat vessel, as shown in Fig 1.5a. The inner vessel is separated from the outer cryostat vessel by a vacuum cavity. Support rods hold the outer cryostat at the center of the cylindrical water tank (referred to as the outer detector), which shields the inner detector components from external γ-rays and neutrons. The outer detector is instrumented with photomultipliers (PMTs) to detect and veto muons. The entire experiment is located deep underground to shield from cosmic radiation background [47]. The SNOLAB-cryopit is the preferred site for the experiment, with a rock overburden equivalent to 6010 m of water and a very low muon rate of 0.27 muon/day/m^2 [48].

The nEXO experiment uses a single-phase, single-sided, cylindrical TPC with charge-collection tiles at the anode and silicon photomultipliers (SiPMs) on the cylindrical wall [47]. Events in the TPC can cause excitation or ionization of the xenon atoms which result in the formation of excited xenon dimers [50]. The decay of these excited xenon dimers results in the emission of 175nm scintillation light. Thus, the SiPMs used in the TPC are special Vacuum Ultraviolet SiPMs (VUV-SiPMs) for collecting the 175nm scintillation light produced in LXe [51]. A uniform drift field exists between the cathode and anode. The charge information (electrons) from an event in the TPC is collected at the charge-collection tiles. Based on

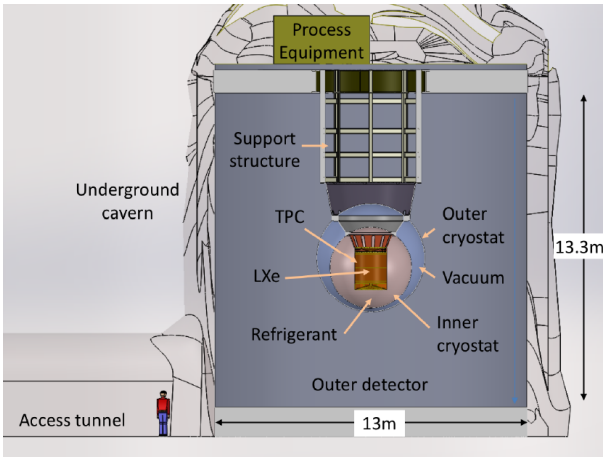

(a) Artist sketch of the nEXO detector concept showing cross-section of the entire experiment and SNOLAB's Cryopit wall (Fig. from [47]).

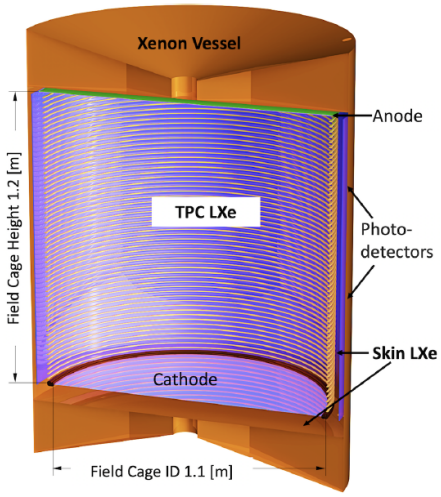

(b) nEXO TPC design of the copper vessel filled with LXe and instrumented with charge and light sensors (Fig. from [49]).

Figure 1.5: nEXO detector cross-section.

our knowledge of electron drift in LXe [52,53], the event position can be reconstructed. The scintillation light collected by the Vacuum Ultraviolet SiPM (VUV-SiPM) provides timing information of an event. $x-y$ position is obtained by locating charge at the charge collecting tiles on the anode, while z-position is reconstructed by comparing the time of arrival of electrons on the anode with the signal from the SiPMs. The combination of ionization and scintillation light is used to achieve an energy resolution of better than 1% i $Q_{\beta\beta}$ [54] by exploiting the anti-correlation of ionization charge and light yield [55]. The field shaping rings (Fig. 1.5b) located inside the chamber ensure the uniformity of the field and thus high spatial resolution in position reconstruction. The design of the chamber is made to limit the radioactivity in the bulk of the chamber. Limited convection in the chamber further prevents radionuclides from traveling to the central fiducial volume [49].

nEXO is being designed to reach the 10^{28} years sensitivity limit, which, using Eqn. 1.10

can be converted to an effective Majorana neutrino mass of less than 15 meV. nEXO will be able to fully explore the inverted hierarchy parameter space as this mass range lies below this parameter space for most nuclear matrix elements, as shown by the green band in Fig. 1.6a (see discussion in [56]). After a livetime of 10 years, nEXO's 90% Confidence Level (CL) sensitivity is projected to be 1.35×10^{28} years and the 3σ discovery potential is estimated as 0.74×10^{28} years [54], as shown in Fig. 1.6b.

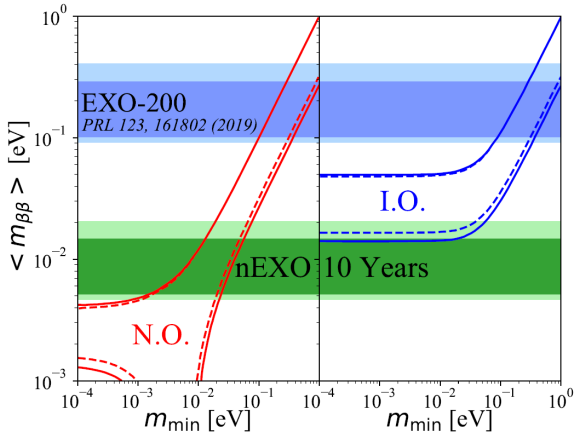

(a) Sensitivity reach of nEXO to the effective Majorana neutrino mass ($m_{\beta\beta}$) as a function of the lightest neutrino mass for (left) normal hierarchy (N.O.) and (right) inverted hierarchy (I.O.).

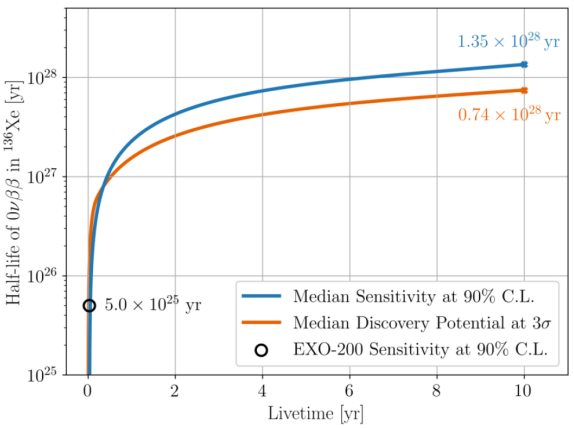

(b) nEXO $0\nu\beta\beta$ senitivity versus livetime. Shown here is the projected sensitivity and discovery potential of nEXO to $0\nu\beta\beta$ decay over its 10-year livetime period.

Figure 1.6: Plots showing projected sensitivity of nEXO to $0\nu\beta\beta$ decay half-life and effective Majorana neutrino mass (Fig. from [54]).

Although the massive detector volume enables one to probe for $0\nu\beta\beta$ with a sensitivity of 10^{28} years, the experiment is limited by backgrounds. These backgrounds are comprised mainly of four types of sources: Long-lived radionuclides, cosmogenically-created radionuclides, neutrino-induced backgrounds, and radionuclides from (α,n) reactions. The primary feature of these sources is that the energy spectrum of emitted gammas or β^- radiation overlaps with the $Q_{\beta\beta}$ energy of ^{136}Xe double-beta decay. A simulated spectrum

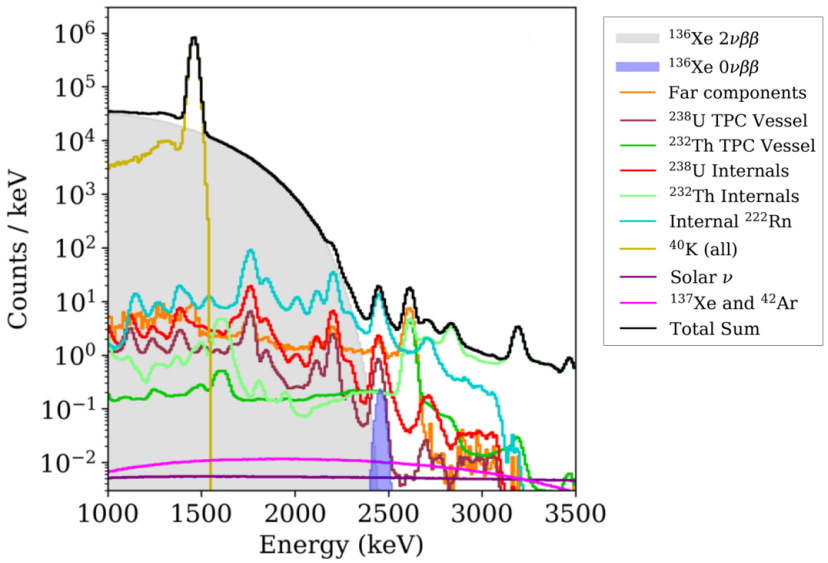

Figure 1.7: Simulated nEXO energy spectrum showing realistic assumptions for background contributions. Events from simulation corresponding to the reconstructed energy range of (1000-3500) keV that pass the fiducial volume cut and diagonal cut are included here. The $0\nu\beta\beta$ decay signal (purple) corresponds to a half-life of 0.74×10^{28} years. (Fig. from [54]).

of nEXO is shown in Fig. 1.7. Background signals contribute counts to the region of interest and limit nEXO's sensitivity. Additionally, the two neutrino double-beta decay itself is an irreducible background.

Several of the design choices of nEXO aim to minimize the number of radionuclides present inside the detector, e.g., an open field cage to reduce cage material and a single-sided TPC to avoid requiring a central cathode. Despite these efforts, some background contributions will remain, which ultimately limit the sensitivity of nEXO. To overcome these, an active background rejection technique called Ba-tagging is being developed as a potential future upgrade to nEXO. In addition to reducing backgrounds, a successful Ba-tagging technique allows verification of a potential $0\nu\beta\beta$ signal as a true $0\nu\beta\beta$ decay event.

1.5 Barium Tagging

The search for $0\nu\beta\beta$ decay with ^{136}Xe offers the possibility to extract and identify the double-beta decay daughter nucleus ^{136}Ba, an idea first introduced in 1991 by M. Moe [57]. The double-beta decay daughter ^{136}Ba can be used to differentiate double-beta decay events from background events. Fig. 1.8 shows the dependence of the sensitivity to $0\nu\beta\beta$ half-life as a function of background rates in the inner 2000 kg of LXe over 10 years of data-taking. In a scenario where only $2\nu\beta\beta$ backgrounds contribute to the $0\nu\beta\beta$ signal, a factor of four improvement in sensitivity compared to the 2018 baseline design can be achieved [56].

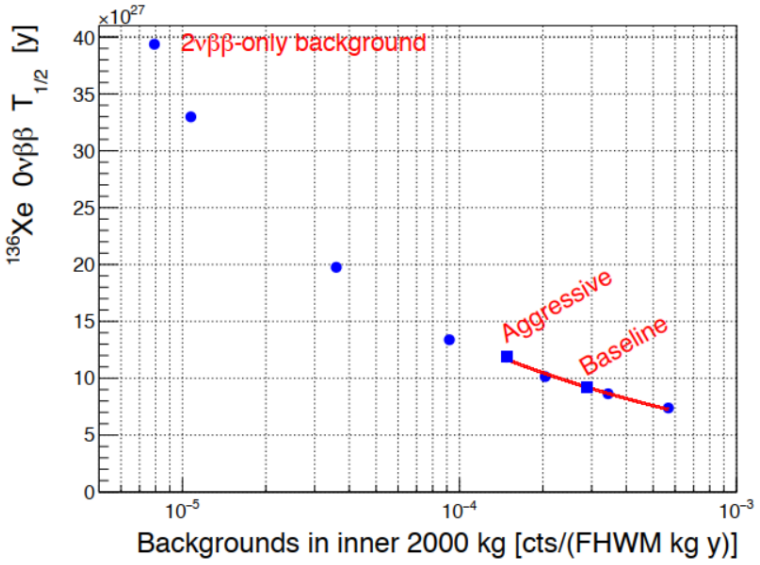

Figure 1.8: Plot showing the variation of detector sensitivity to $0\nu\beta\beta$ half-lives as a function of background rates (Fig. from [56]). A 100% efficient Ba-tagging scenario would result in a sensitivity labeled $2\nu\beta\beta$-only background, which is a factor four improvement on the 2018 baseline design sensitivity.

A flow chart in Fig. 1.9 shows the procedure for the tagging of ^{136}Ba ions. When a potential $0\nu\beta\beta$ event is registered, that particular site is located in Step I. A small quantity of detector volume is extracted from this location to look for the ^{136}Ba daughter nucleus in

Step II. The ^{136}Ba is then separated from the accompanying xenon in Step III, followed by Step IV where ^{136}Ba is identified. Verifying the presence of ^{136}Ba at the location of a potential signal inside the detector will provide definitive proof for excluding all non-double-beta decay backgrounds.

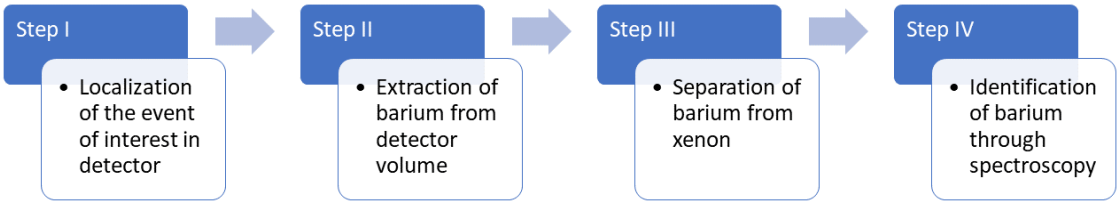

Figure 1.9: Overview of the processes involved in the tagging of ^{136}Ba .

Ba-tagging is made possible by the fluorescence property of Ba^+ ion when illuminated with a specific wavelength of light. In fact, some of the oldest experiments from the 1980s that developed imaging of trapped ions were based on $^{136}Ba^+$ ions [58]. In the laser spectroscopy scheme adopted here, two lasers are directed at trapped $^{136}Ba^+$ ions. The combination of lasers excites the ground state $^{136}Ba^+$ ($\lambda = 493.545\,\text{nm}$) while preventing the ion from ending up in the meta-stable state ($\lambda = 649.869\,\text{nm}$) [59, 60]. While laser spectroscopy of ^{136}Ba is well developed, the extraction and separation of ^{136}Ba from ^{136}Xe is difficult. Thus, the nEXO collaboration is pursuing different approaches using RF-funnels [61], electrostatic probes [62], or laser spectroscopy on barium atoms trapped in xenon ice [63, 64]. Most recently, the NEXT collaboration demonstrated Ba^{2+} identification in xenon gas using a molecular fluorescence imaging technique [65]. The approach relevant for this thesis is the one pursued by the Canadian group that utilizes RF ion transport and trapping technology for extracting and isolating the ion and laser fluorescence and mass spectroscopy for ion identification. A schematic of the Ba-tagging scheme is shown in Fig. 1.10.

The technique requires first the extraction of ions from the location of a $0\nu\beta\beta$ signal. A particular capillary is currently being developed at Carleton University to achieve extraction. The design for the capillary is at a conceptual stage; during operation, it will be moved into

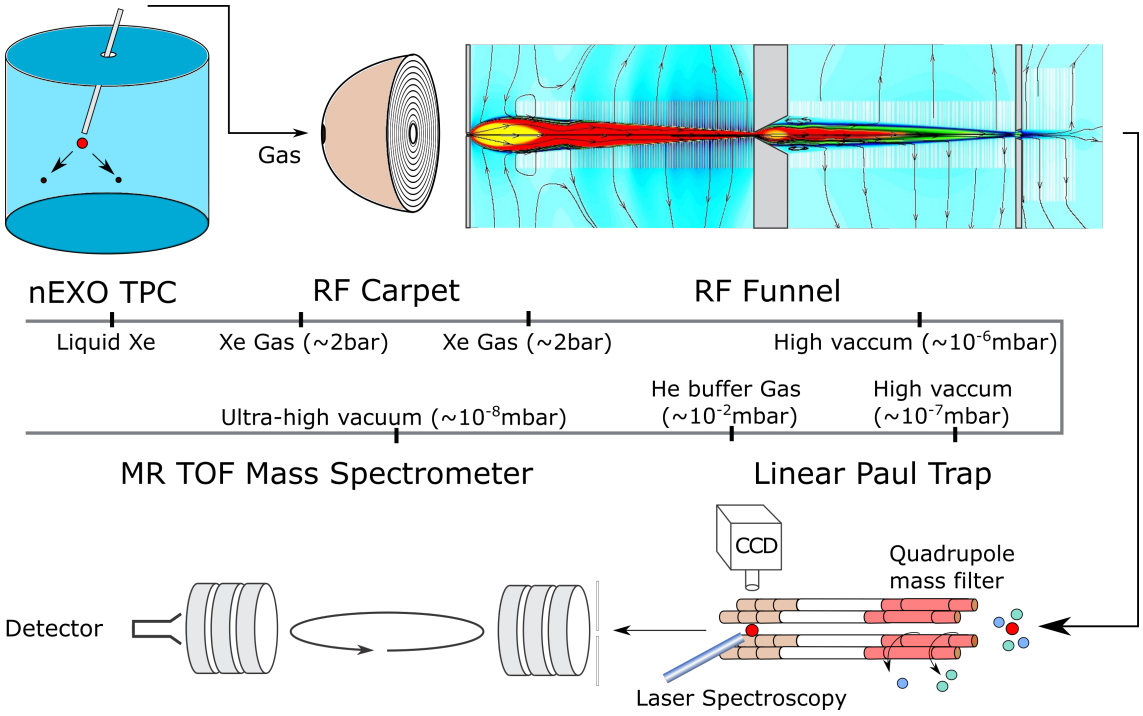

Figure 1.10: Schematic of the entire Ba-tagging scheme. The ^{136}Ba ion is extracted from the TPC along with LXe. After extraction, the ^{136}Ba is present with accompanying ^{136}Xe at high pressure. An RF carpet facilitates ion injection into the RF-funnel, which brings the ^{136}Ba from high pressure to high vacuum. ^{136}Ba is then transferred to a linear Paul trap for filtering and trapping. Here the ^{136}Ba ion is identified using laser fluorescence spectroscopy and then transferred to a mass spectrometer to determine its mass.

the TPC to extract a small quantity of xenon from the detector volume at the site of a potential $0\nu\beta\beta$ event. The extracted LXe phase transitions to gas while carrying the $^{136}Ba^{+}$ along with it. Ba^{+} is expected and not Ba^{2+} because at this stage Ba^{2+} is expected to convert to Ba^{+} through an electron exchange with xenon [57]. After the phase transition, the ion is present with accompanying Xe gas at pressures of (1-10) bar. The high pressure poses a challenge in separating the ^{136}Ba ion to vacuum due to high collision rates with atoms of comparable masses. This task is made possible through an RF-only ion funnel. The function of the RF-funnel is to transport the ion from high pressure ($\approx$ 10 bar) to vacuum

($\approx 10^{-6}$ mbar) [61]. The RF-only feature limits the requirement of extra elements, such as DC drag fields. For accepting the ions into the funnel, an RF carpet is being developed that utilizes optimized RF potential and electrode geometry to guide ions towards the axis.
The $^{136}Ba^{+}$ ion is then transferred to the linear Paul trap, where the ions are trapped for element-specific identification using laser fluorescence spectroscopy. The ion is then transferred to a downstream multiple-reflection time-of-flight mass spectrometer (MRTOF-MS) to accurately determine its mass [66].

Chapter 2

The Linear Paul Trap for Ba-tagging

The invention of ion trapping dates back to the 1950s, when there was a requirement for isolated systems for studying properties of chemical reactions, molecules, and lifetimes of metastable nuclei [67]. This required the system to store particles for an extended duration which gave rise to the field of ion trapping. A conventional ion trap uses electric fields, magnetic fields, or their combination to achieve three-dimensional confinement of charged particles [68]. Ion traps find use in various physics disciplines such as the study of the lifetime of radioactive nuclei, qubits for quantum computing [69], storing antimatter, and recently even cooling antimatter [70].

In 1989, Nobel prize was awarded to Hans G. Dehmelt (for the Penning trap) and Wolfgang Paul (for the Paul trap) for their contributions in developing ion trapping techniques. 3D confinement of ions cannot be performed using solely electrostatic fields based on Earnshaw's theorem, which states, 'A charged particle cannot be held statically in stable equilibrium by electrostatic forces alone' [71]. The Penning trap, shown schematically in Fig. 2.1, uses an axial magnetic field for radial confinement while the DC voltage across the end caps and the ring (U) axially confines the ions. The radial restoring force for the Penning trap comes from the force resulting from the radial velocity

component of the ion motion in an axial magnetic field.

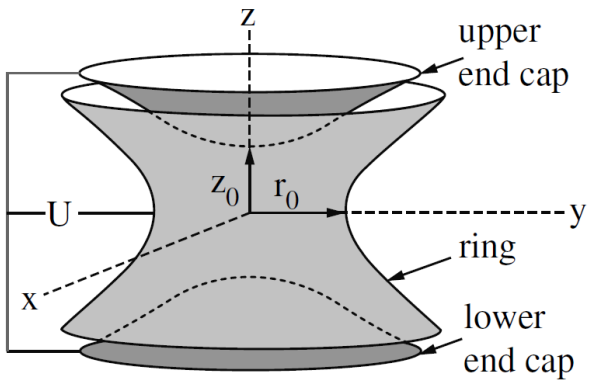

Figure 2.1: Basic electrode arrangement for Paul and Penning traps. Trapping potential is created by hyperbolic shaped end cap electrodes and ring surface at the trap-center (Fig. from [72]).

The idea for the Paul trap originated from the work on focusing of atomic and molecular beams [68]. A Paul trap is the extension of this two-dimensional focusing to three-dimensions. Fig. 2.1 shows the basic geometry of both Paul and Penning traps. There are three electrodes in total; two end caps and a ring. These electrodes are hyperbolic in shape for creating the required trapping potential at the trap center. The Paul trap replaces the magnetic field of the Penning trap with an alternating electric field, with frequencies usually at Radio Frequency (RF) range, hence also called an RF Paul trap.

From Earnshaw's theorem, it is already known that electrostatic fields cannot confine ions. The RF potential applied to the Paul trap focuses the ions in a direction while defocusing them at the other (see Fig. 2.2). The oscillating potential results in the rapid change of the focusing and defocusing direction at saddle point at the center, thus trapping the ions (see Section 2.1 for a detailed explanation).

A modified geometry based on the principles of the Paul trap is the Linear Paul Trap (LPT). Section 2.1 describes the theory of RF-based ion guides, which form the basis of radial confinement in the LPT or trapping in the Paul trap. This theory is extended in Section 2.2

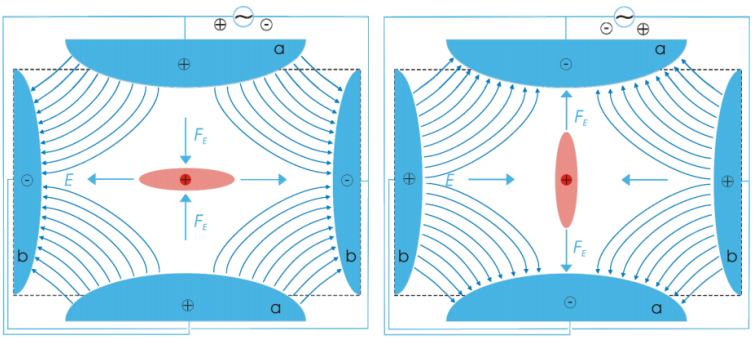

Figure 2.2: The two figures showing the potential inside a Paul trap at two different points during an RF cycle, and the corresponding expected shape of ions trapped within. The electrodes are shown in solid blue, and the arrows indicate the direction of the field lines between them. The red ellipse at the center represents the trapped (+ve) ions. At different phases of an RF cycle, the trapped ions are focused in a particular direction while being defocused in the other (Fig. from [73]).

to exploits the stability of ion guides for filtering ions. Finally, in Section 2.3 the operation of the ion trap is described.

2.1 RF Quadrupole Ion Guide

In 1842, Samuel Earnshaw introduced the theory that explained the absence of maxima (or minima) in an electrostatic field [74]. Hence, although electrostatic fields cannot confine charged particles, the theory allows 'saddle points', which is exploited to trap ions. Among the first electrode geometries studied for charged particle manipulation and transport were multipole fields, the most basic among them being a quadrupole configuration. Fig. 2.3 shows the arrangement and polarity of electrodes in a basic quadrupole.

Potentials from electrodes in the quadrupole configuration create a saddle point at the center, as seen in Fig. 2.4. Thus, although the particles cannot be focused in all directions, they can be focused in one direction while being defocused in the other. The use of RF voltage

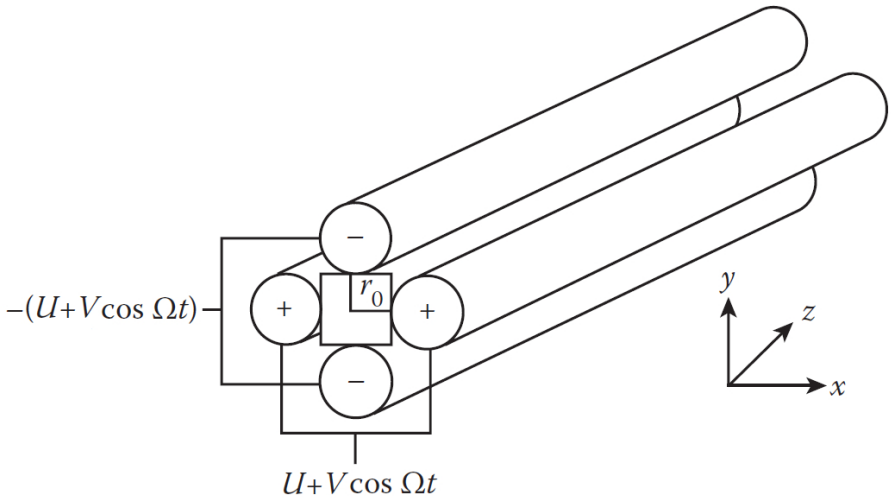

Figure 2.3: Schematic of the electrode arrangement in a quadrupole. The quadrupole consists of four electrodes, uniformly positioned parallel and at equal distance r_o from the central axis. The four electrodes are grouped such that diametrically opposite electrodes have the same polarity while adjacent electrodes have the opposite polarity.

exploits this feature of a quadrupole, where, by alternating the potential, the direction of divergence and convergence are switched (shown in Fig. 2.2).

Fig. 2.4 shows the motion of a charged particles under the influence of quadrupole potential with origin as the center of ion trap. The high frequency of the oscillation thus results in the particles being restricted to the center of the quadrupole providing means for ion trapping.

The particles are focused at the axis with a force that acts to return them towards the axis and scales with the distance from the axis,

$$F = -kx, \tag{2.1}$$

where k is a proportionality constant, the force F scales linearly with distance x from the equilibrium position (in this case, the distance from the center axis). This requires an

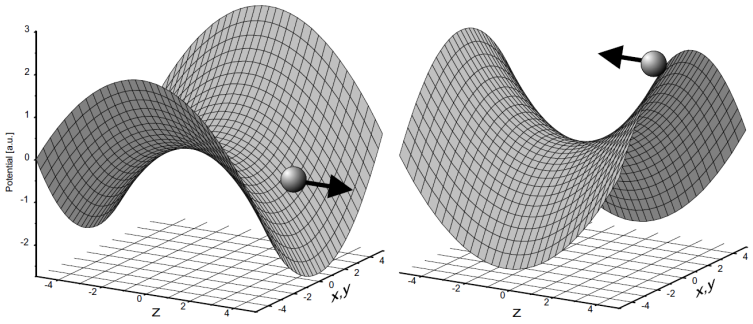

Figure 2.4: Motion of a charged particle under the influence of alternating potential applied to electrodes of Paul trap. The particle is confined at the center of the trap due to the rapid oscillation of converging direction at the saddle point (Fig. from [75]).

electrostatic potential of the form.

$$\Phi = c(\alpha x^2 + \beta y^2 + \gamma z^2), \tag{2.2}$$

where, α, β, γ are constants; c is the time dependant part of the potential ($c = \phi(t)$) and (x, y, z) are the position coordinates. Using the potential from Eqn. 2.2 in the Laplace equation, one can see that

$$\alpha + \beta + \gamma = 0. \tag{2.3}$$

Assuming the ion trap is symmetric about the z-axis, the field is identical along x and y-axes. Thus, the simplest solution to Eqn. 2.3 is

$$\alpha = \beta; \gamma = -2\alpha. \tag{2.4}$$

Fig. 2.1 shows the geometry of a conventional Paul trap. z_0 is the distance of endcap center from the trap center, r_0 is the distance of the ring from the center. The surfaces can

thus be described as,

$$\text{Endcaps} : r_o^2 = r^2 - 2z^2, \tag{2.5}$$

$$\text{Ring} : 2z_o^2 = 2z^2 - r^2. \tag{2.6}$$

Here a choice of $r_o/z_o = \sqrt{2}$ (Eqn. 1.21 in [76]) is usually made to achieve electrical symmetry between the endcaps and the ring electrode. Finally, the expression for the electric potential can be rewritten using Eqn. 2.2, 2.4, 2.5 and 2.6 as,

$$\Phi = \Phi_o\left(\frac{r^2 - 2z^2}{d^2}\right), \tag{2.7}$$

where $r^2 = x^2 + y^2$, and d is defined as,

$$d^2 = \left(z_o^2 + \frac{r_o^2}{2}\right). \tag{2.8}$$

The first term Φ_o in Eqn. 2.7 constitute the potential applied to the electrodes such that

$$\Phi_o = U + V\cos\Omega t. \tag{2.9}$$

Here, U is the DC voltage and V the amplitude of the RF voltage with oscillation frequency Ω and varying with time t. The other possible solution to Eqn. 2.3 is,

$$\alpha = -\beta; \gamma = 0. \tag{2.10}$$

Eqn. 2.10 implies that the potential is independent of the z-position, which is the case for RF ion guides. The Paul trap electrodes are replaced with a quadrupolar arrangement of hyperbolic electrodes, which (in theory) extend infinitely along the z-axis for the potential to be independent of z-position. Fig. 2.3 presents the typical setup for an RF ion guide. Here,

the electrodes shown are cylindrical rather than hyperbolic, as required by theory. However, the electric potential characteristics close to the central axis are a good approximation of hyperbolic potential for some specific r_o and rod radius. The use of cylindrical rods is common due to the ease of machining. In the case of cylindrical electrodes, Eqn. 2.7 changes to

$$\Phi = (U + V\cos\Omega t)\left(\frac{x^2 - y^2}{r_o^2}\right), \tag{2.11}$$

where r_o is the radial distance of the electrodes from the central axis. Using Eqn. 2.11 the electric field from the potential is derived as,

$$E(x,t) = -(U + V\cos\Omega t)\left(\frac{2x}{r_o^2}\right), \tag{2.12}$$

$$E(y,t) = -(U + V\cos\Omega t)\left(\frac{-2y}{r_o^2}\right). \tag{2.13}$$

Thus, for a particle of charge Q and mass m, the equations of motion are

$$\frac{d^2x}{dt^2} + \left(\frac{Q}{m}\right)(U + V\cos\Omega t)\left(\frac{2x}{r_o^2}\right) = 0, \tag{2.14}$$

$$\frac{d^2y}{dt^2} - \left(\frac{Q}{m}\right)(U + V\cos\Omega t)\left(\frac{2y}{r_o^2}\right) = 0. \tag{2.15}$$

The motion in the two directions perpendicular to the axis of the ion guide is independent of each other. The solution of Eqn. 2.14 and 2.15 takes the form of Mathieu functions [77] when arranged in differential form

$$\frac{d^2u}{d\epsilon^2} + (a - 2q\cos 2\epsilon)u = 0, \tag{2.16}$$

where u is the displacement and ϵ is a dimensionless constant related to time t by $\epsilon = \Omega t/2$. Ω in this relationship is the oscillation frequency of the RF potential. Here, (a, q) are dimensionless constants called trajectory parameters, which influence the nature of the

solution to Eqn. 2.16 being either a convergent or divergent solution. For the ion motion, this translates to having either a stable or unstable trajectory for ions in the ion guide (or trapping capability for ion traps). Rewriting Eqn. 2.14 and 2.15 to match this different form by substituting t with ϵ gives:

$$\frac{d^2x}{d\epsilon^2} + \left(\frac{Q}{m}\right)\left(\frac{4}{\Omega^2}\right)(U + V\cos 2\epsilon)\left(\frac{2x}{r_o^2}\right) = 0, \tag{2.17}$$

$$\frac{d^2y}{d\epsilon^2} - \left(\frac{Q}{m}\right)\left(\frac{4}{\Omega^2}\right)(U + V\cos 2\epsilon)\left(\frac{2y}{r_o^2}\right) = 0. \tag{2.18}$$

Comparing Eqn. 2.17 and 2.18 to Eqn. 2.16 gives:

$$a_x = \frac{8QU}{mr_o^2\Omega^2}, \qquad q_x = \frac{-4QV}{mr_o^2\Omega^2}, \tag{2.19}$$

$$a_y = \frac{-8QU}{mr_o^2\Omega^2}, \qquad q_y = \frac{4QV}{mr_o^2\Omega^2}. \tag{2.20}$$

The motion of charged particles depends on the choice of trajectory parameters (a, q), which relate to the applied DC (U) and RF (V) potentials, respectively, for a given set of parameters (Q, m, r_o, Ω). In general, the solution of Mathieu's differential equation gives a stable solution in certain regions of the trajectory parameter space as shown in Fig. 2.5a.

The combined stability for two perpendicular directions (here referred to as x, y-axes) gives the blue region in Fig. 2.5b, where the (a, q) values result in a stable solution, simultaneously in both directions. This provides the radial confinement in an ion guide. Operating the quadrupole in this region ensures ion transmission without loss.

2.2 Quadrupole Mass Filter

The theory introduced in the previous section highlights the relation of stable ion trajectories to the stability region for an ideal quadrupole ion guide. Eqn. 2.19 shows the proportionality

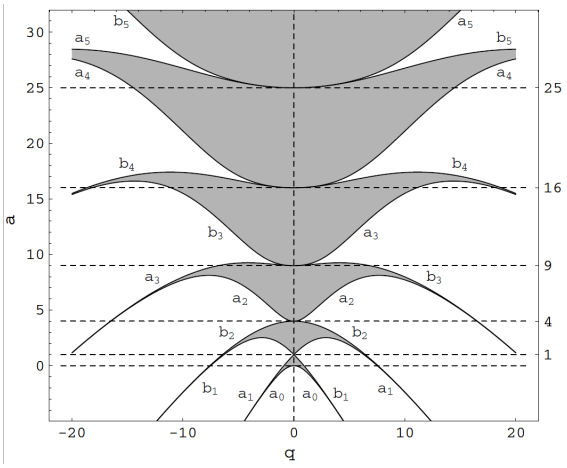

(a) Stable trajectory parameters for solutions of Mathieu differential equations. Only parameters from the shaded region yield convergent solutions (Fig. from [76]).

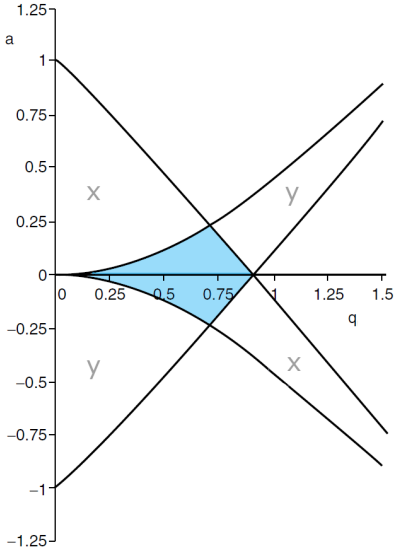

(b) Combined stability diagram for x-axis and y-axis for the ion guide. The blue shaded region represents the first overlapping region that yields stable solutions in both directions (Fig. from [77]).

Figure 2.5: Stable trajectory parameter space for solutions to Mathieu's equation. The figure on the left explores possible values of trajectory parameters (a_i, q_i) which give convergent solutions to Mathieu's differential equation. The figure on the right shows the combined stable regions for x-axis and y-axis shown by the region highlighted by blue.

between the trajectory parameters (a, q) and the DC, RF potentials (U, V) for a given charged particle of charge Q, mass m and RF potential of frequency Ω. The voltages can be selected to ensure (a, q) are in the stable region shown in Fig. 2.5b. The working principle of a Quadrupole Mass Filter (QMF) is an extension of this theory. Rather than guiding all ions, the potential can also be selected to reject specific ions. For a given value of DC (U) and RF (V) amplitudes as defined in Eqn. 2.9, a specific (Q/m) value or a range of (Q/m) values can be selectively allowed by a quadrupole [78]. This (Q/m) specific ion transmission allows the filtering of ions using a quadrupole.

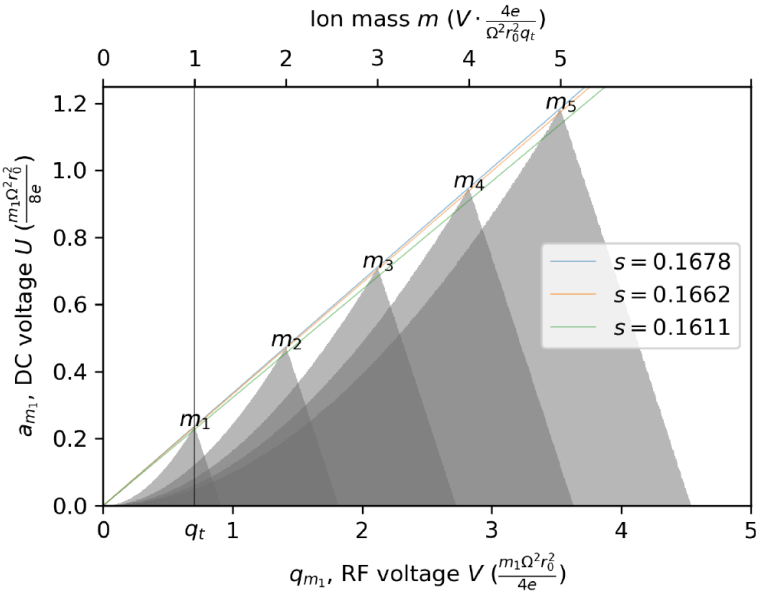

Figure 2.6: Variation of RF and DC potential values of stability region for different ion mass to charge ratios. In this figure, all voltages are set with reference to some ion of mass m1. $s = U/V$, is the slope of the mass scan line. (Fig. from [79]).

Fig. 2.6 shows the scaling of the accepted (a_{m1}, q_{m1}) values with the mass of the ion. In the figure, for (a_{m1}, q_{m1}) = (0.6,2), ions of mass 'm_3' are selectively allowed to pass while m_1, m_2, m_4 and m_5 are filtered out. On the other hand, for (a_{m1}, q_{m1}) = (0.2,2) transmits all masses for $m \geq m_3$ while the lighter ones like m_1 and m_2 are filtered. This can further be used to perform mass spectrometry. The peak of the stability regions for each ion mass can be scanned by varying the DC and RF voltages according to the lines shown in Fig. 2.6. Here, s represents the slope of the mass scan line. The resolving power R is related to the trajectory parameter q as

$$R = \frac{m}{\Delta m} = \frac{q}{\Delta q} \text{ [80]}, \tag{2.21}$$

where q is related to m by Eqn. 2.19 and Δq is the range of stable q values covered by the mass scan line at the tip region [81]. During the operation of LPT setup, a suitable point near the tip region will be used for the QMF, which provides the required resolving power

($R > 80$) required to filter out expected contaminants from the RF funnel [79].

2.3 Ion Trapping

The previous sections discussed the ion guide and filtering property of the quadrupole arrangement of electrodes. This involved the constraining of radial motion of the ions through a specific choice of DC and RF voltages while the axial motion is unconstrained.

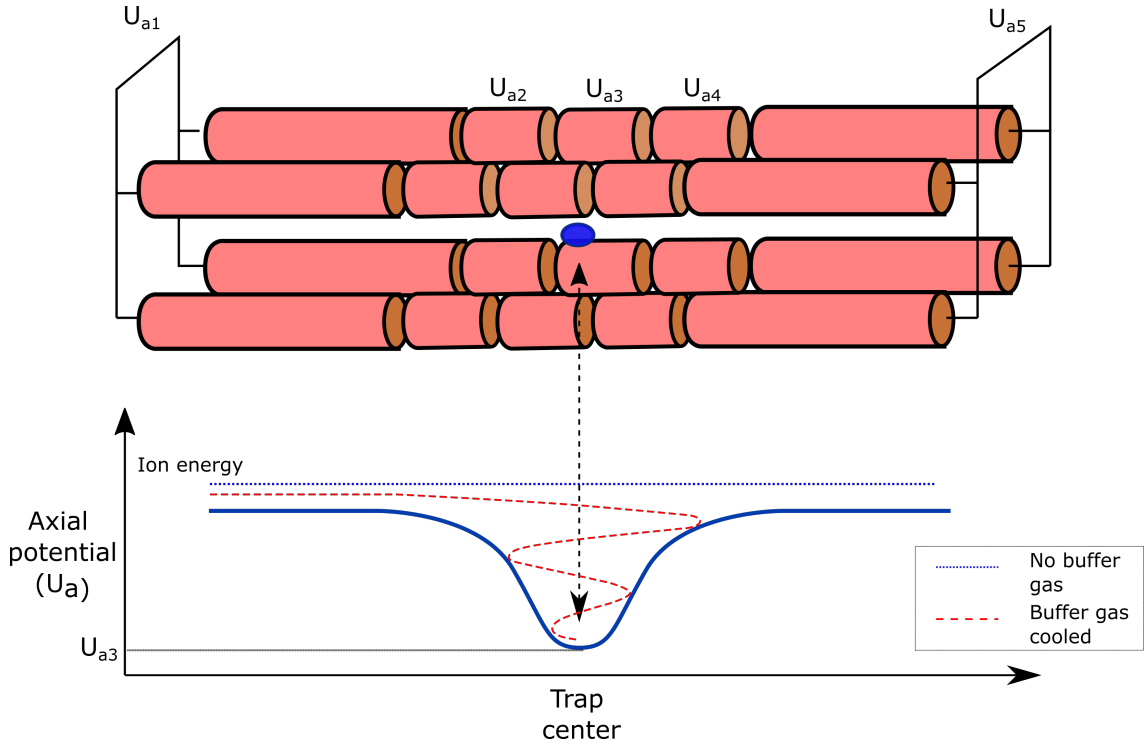

Figure 2.7: Schematic diagram of a typical linear Paul trap. The figure shows segmented quadrupole electrodes for varying the axial DC potential ($U_{a1}, U_{a2}..U_{a5}$) and creating minima at the trap center. Each set of quadrupole, additionally, has an RF voltage superimposed to confine the ions radially. As a consequence of the Liouville theorem, in the absence of a buffer gas, there is no net loss of total ion energy (blue dashed line). Therefore, to trap ions in the potential well, a buffer gas is used to collisionally cool the ions (red dashed line).

To trap ions using a quadrupole field, additional control in the axial direction is required. This control is introduced by forming a DC potential well in the quadrupole. By doing this, in addition to radial confinement, the axial motion of the ions can also be controlled. A general setup of this kind of trapping is shown in Fig. 2.7. The quadrupole electrodes are segmented here to float each at a different DC potential. By appropriate choice of voltages, a potential well is set up at the center of the trap. This additional axial DC potential (U_a) is superimposed onto the original potential as follows,

$$(+)\text{Electrode pair}: \quad (U + V\cos(\Omega t)) + U_a, \tag{2.22}$$

$$(-)\text{Electrode pair}: -(U + V\cos(\Omega t)) + U_a. \tag{2.23}$$

In Fig. 2.7, ions injected through either side follow the direction of the axial field towards the well. As a consequence of the Liouville theorem [82], under the influence of conservative forces (in this case, the electrostatic potentials), there is no net loss of total ion energy (blue dashed-line in Fig. 2.7). Therefore, even after entering the trap, the ions have enough energy to exit. Thus, some form of non-conservative force is required to make trapping possible. One could trap ions using the configuration in Fig. 2.7 by raising the surrounding potentials when the ion arrives at the center, but this requires very exact timing.

2.3.1 Buffer gas

The common method to slow or cool ions is the use of inert or non-interacting gas [83]. While traversing along the axis, ions undergo collisions with the buffer gas and lose energy. This results in the ions having less energy than the height of the potential well and get trapped. A popular choice of buffer gas is helium due to its inert nature and light atomic mass, which makes it more effective than other heavier gases like argon [84]. The mechanics of buffer gas

cooling can be modeled by a simple viscous drag model,

$$F = -\eta v, \tag{2.24}$$

where F is the drag force proportional to the ion velocity v and η being the proportionality constant. For ions in a buffer gas, drift velocity v_d is related to the electric field E by mobility κ as

$$v_d = \kappa E. \tag{2.25}$$

Substituting this in equation Eqn. 2.24 to force experienced by an ion of charge Q gives

$$F = QE = Q\frac{v_d}{\kappa} = \eta v_d. \tag{2.26}$$

Incorporating Eqn. 2.24 in Eqn. 2.16 gives

$$\frac{d^2u}{d\epsilon^2} + 2b\frac{du}{d\epsilon} + (a - 2q\cos 2\epsilon)u = 0, \tag{2.27}$$

where b $= Q/(m\kappa\Omega)$. Eqn. 2.27 can be rewritten to obtain Mathieu's differential equation through the introduction of an exponential term. Transforming $u = we^{-k\epsilon}$ leads to

$$\frac{d^2w}{d\tau^2} + (a - k^2 - 2q\cos 2\epsilon)w = 0. \tag{2.28}$$

Eqn. 2.28 is similar to Mathieu's equation in Eqn. 2.16 with a shift to the stability parameter a given by $a_d = a - k^2$. Thus, the presence of background gases introduces a shift in the stable region shown in Fig. 2.5b. Although this approach gives a clear picture of modifications needed to the undamped case, the above formalism has been found to only work for small damping ($k \ll 1$). For strong damping, distortions and shifts have been observed, which leads to instability in some regions where otherwise stability was expected [85].

2.4 Linear Paul Trap for Ba-tagging

The Linear Paul Trap setup being commissioned at McGill University consists of a collection of ion optics, a Quadrupole Mass Filter (QMF), two stages of ion coolers, and a buncher. A SolidWorks rendering of the model of the setup is shown in Fig. 2.8. Ions are generated

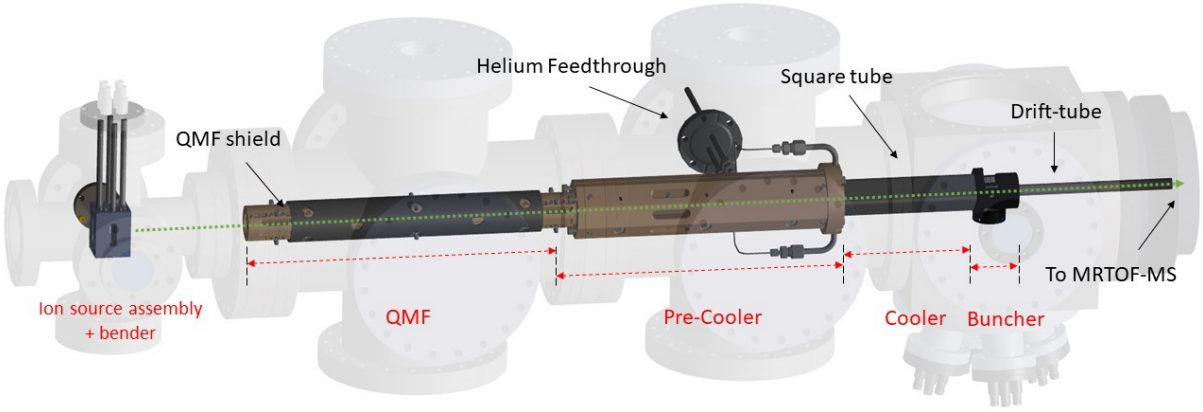

Figure 2.8: Rendering of the model of the LPT setup for Ba-tagging. Shown are the different segments of the LPT setup as installed in vacuum chambers (greyed out). The second 6-way cross houses the pre-cooler with a feedthrough for helium buffer gas. The cooler and the buncher are situated in the square cube at the end which has viewports installed on sides for directing the laser to the trap center. The QMF receives ions from the 4.5" cross housing the ion source assembly. After ions pass through the different segments, they are transferred to the MRTOF-MS located downstream from the LPT setup.

by the ion source assembly, which pass through the bender and enter the QMF. From here, the filtered ions pass through the cooler sections to reach the buncher. Ions are temporarily stored in the buncher to perform laser fluorescence spectroscopy. After identification, the ions are transferred to the downstream MRTOF-MS as shown in Fig. 1.10.

Fig. 2.9 shows the different electrodes starting from the ion source to the drift-tube at the end of the LPT setup. Fig. 2.9 also shows the nomenclature used to refer to the different elements including all bender electrodes, apertures, lenses, and quadrupole

electrodes. In Fig. 2.9 'a/b' suffix is used to indicate the polarity of the particular quadrupole electrode pair, such that electrodes with label 'a' are 180° out of phase with electrodes with label 'b'.

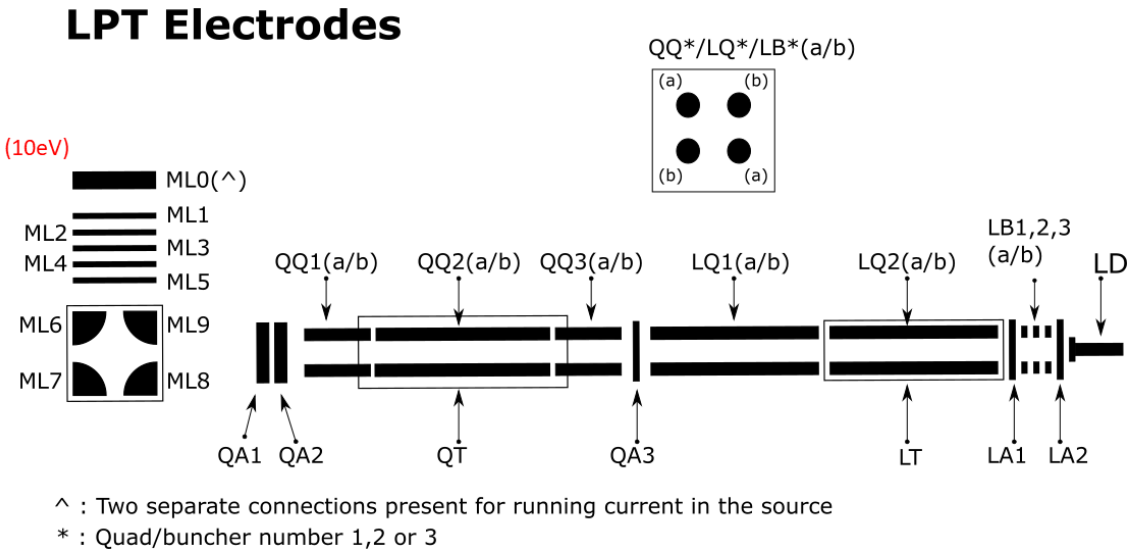

Figure 2.9: Schematic of the LPT setup showing only the electrodes present. All electrodes are named based on a convention to simplify use, a description for which is provided in Appendix D).

2.4.1 Ion source

Ion source refers to a device or apparatus that can produce atomic or molecular ions [86]. Ion sources are extensively used in several fields of nuclear and particle physics. Here, a thermal ion source (Model 101141 SIMS Cs Ion Source, HeatWave Labs) is used to produce ^{133}Cs ions. The ions produced have a charge-to-mass ratio close to ^{136}Ba and thus are ideal for testing out the LPT setup. Fig. 2.10a shows the complete ion source assembly consisting of a source holder and five lenses used with a quadrupole deflector for bending the generated

ions towards the LPT setup. Fig. 2.10b shows the shape and arrangement of the bender electrodes along with path of the ions shown by the green dashed line.

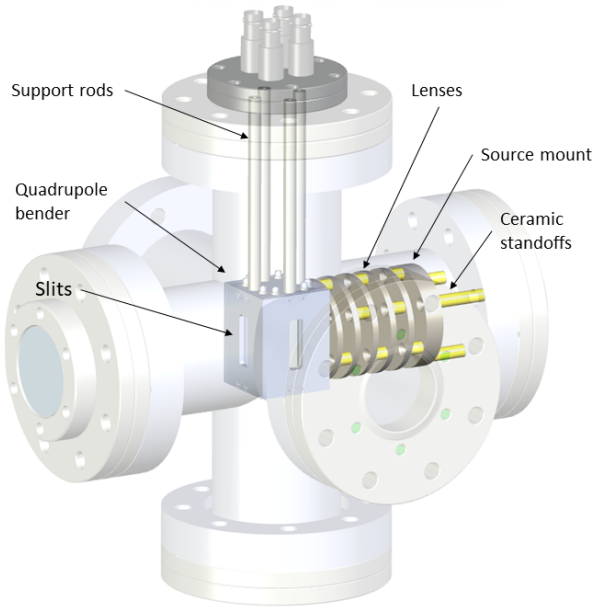

(a) Model of complete ion source assembly along with quadrupole deflector housed in a CF 4.5" 6-way cross.

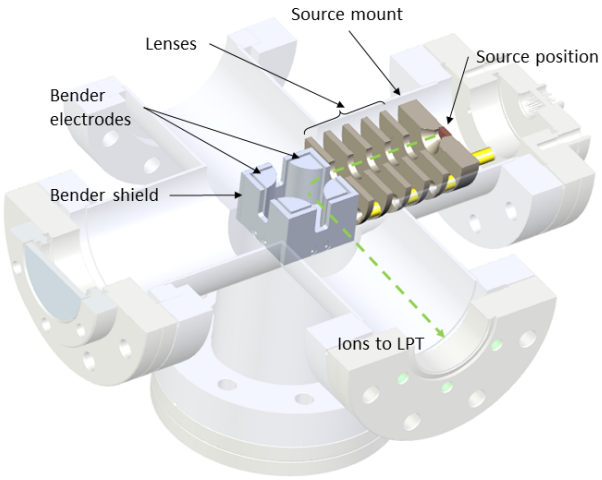

(b) Sectioned view showing bender electrodes, source position, and lens assembly.

Figure 2.10: Engineering rendering of the ion source assembly used for the LPT commissioning.

The thermal ion source generates ions through thermionic emission when supplied with ~3 A current. The generated ions are extracted from the source through a set of negative biases applied to the first two lenses (ML1, ML2 in Fig. 2.9). The source holder (ML0) itself is held at a positive bias of 12 V to prevent deposition of the positive ions. Following the first two lenses, the next three lenses are operated as Einzel lenses. The feature of this particular arrangement of lenses is to facilitate the focusing of the stream of ions generated by the thermal source. The focused ion beam then passes through a quadrupole deflector (ML6-8 in Fig. 2.9), which bends the ion beam towards the entrance lenses of the QMF

(QA1). The bender was specially designed to be used in a 4.5" 6-way cross (DN63CF (4.50" OD)) together with the ion source assembly (holder and five lenses). The bender consists of four rods, each quadrant cut from a cylinder of 1" diameter and ∼1.3" in length. The four electrodes are housed inside a stainless-steel box with slots cut out in the sidewalls for ions to enter and exit (see Fig. 2.10b). The design for the bender assembly has been optimized for ion transmission. The ratio of electrode curvature to inter electrodes spacing (r_{cyl}/r_o) is based on a 'magic number', which provides fields closest to hyperbolic electrodes as with the use of cylindrical electrodes, typically $r_{cyl}/r_o \in (1.14, 1.16)$ [87,88]. Additionally, the spacing of electrodes, bender shield, and lenses is greater than the threshold distance for dielectric-breakdown in vacuum. The source uses a quadrupole deflector, rather than being mounted in line of sight to the LPT setup to facilitate a future upgrade of the source assembly to a laser-ablation type source (see the window in the flange for laser entrance in Fig. 2.10a). The upgrade will enable the generation of ions of different masses using the targeted nature of ion production by laser ablation [89]. Through motorized control of the laser position on the target, different types of ions can be generated which will be useful in further studies of the capabilities of the setup for a range of ion masses [90]. The RF-funnel (described in Section 1.5) is located upstream from the LPT setup to supply ions extracted from high xenon pressure. The deflector also helps in choosing between ions produced by the ion source and ions from the RF-funnel. Images of the assembly taken during commissioning can be found in Appendix C.

2.4.2 QMF design

Ions generated from the source are first injected into the QMF for filtering based on the theory described in Section 2.2. The design consists of three sets of quadrupole electrodes as shown in Fig. 2.11.

Two of the three pairs are short quadrupole segments located at the start and end of the

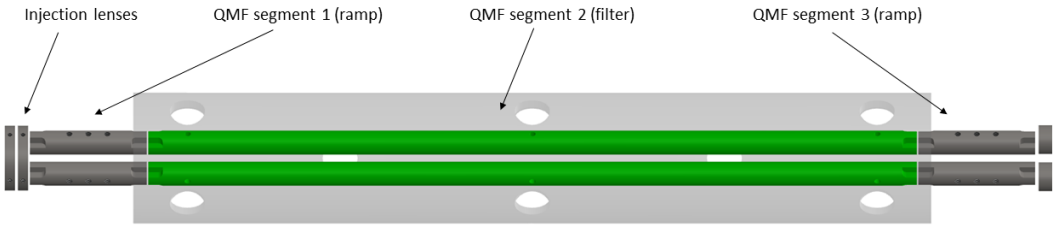

Figure 2.11: Rendering of the model of the QMF (plastic holder omitted) showing the three quadrupole segments along with lenses at the entrance. In green, the second segment is the longest of the three segments and is responsible for the filtering action.

main quadrupole shown in green in Fig. 2.11. This kind of arrangement is required to deal with the fringe fields of the QMF [91]. The QMF voltages are set to trajectory parameter values at the peak of the stability region, which provides high resolving power.

A problem with a single quadrupole is that the electrodes give rise to a fringe field at the entrance and exit of the quadrupole. Near the openings of the quadrupole, the ions see potentials that lie outside the stability region. Hence, additional segments are added, which act as ramps for the potential at the ends, to make the transition for the ions more gradual. This is typically done by setting the differential DC component (U from Eq. 2.9) of the quadrupole potential of the smaller segments (QMF segment 1 and 3 in Fig. 2.11) to zero. The operation of QMF is illustrated in Fig. 2.12 by the green dashed line. Since the DC voltage is linked to the stability parameter a, from Fig. 2.12 and Eqn. 2.19 we can see that the ion stays in the stability region even with the fringe field present. This is shown in Fig. 2.12 by the path from origin to point 'A'. Next, the ion enters the filter segment, during which it goes from 'A' to 'B' from within the stable region. In the absence of the small segments (1,3) the ions could end up in the unstable region (path shown in red in Fig. 2.12) before reaching the stable point 'B'.

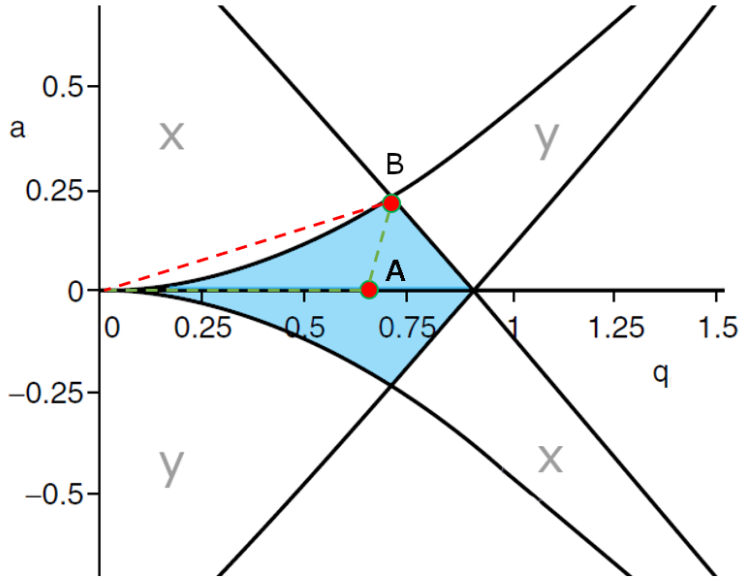

Figure 2.12: Scheme for circumventing the problem of fringing fields in the QMF. Ramp segments are used to gradually bring ions to the peak of the stability region. In this scheme, the ramp segment operates at point 'A' while the filter segment is at 'B'. The red dashed line depicts the path taken in the absence of the ramp segments that briefly go through the unstable region.

2.4.3 Ion cooler

The ions enter the QMF with a certain kinetic energy, mainly from the bias voltage applied to the source ($\sim 10\,\text{eV}$) in the case shown in Fig. 2.9. After passing through the QMF, ions need to be cooled down to sub-eV energy for efficient transfer and trapping operations. This requires a helium buffer gas pressure in the range of $(10^{-3} - 10^{-2})\,\text{mbar}$ scale as was shown in [79]. This buffer gas pressure is too high for the QMF, which requires a high vacuum for efficient operation. Thus, a pre-cooler stage is added between the cooler and QMF. The pre-cooler region thus has a pressure gradient due to differential pumping going from higher pressures inside the cooler to high vacuum ($\sim 10^{-5}\,\text{mbar}$) at the QMF [79]. The cooler stage is designed to have a potential gradient to guide the ions in forward direction while

simultaneously cooling them. It consists of a quadrupole arrangement of special tapered electrodes enclosed within a metallic tube held at negative potential ∼(-100 to -50). Fig. 2.13 shows the special electrodes and how they taper in width along the length. This feature allows a gradual increase in the potential that creeps into the axis, thus resulting in a potential gradient (shown in Fig. 3.9 in Chapter 4). The gradient is directed towards the next stage, the buncher, where ions are trapped.

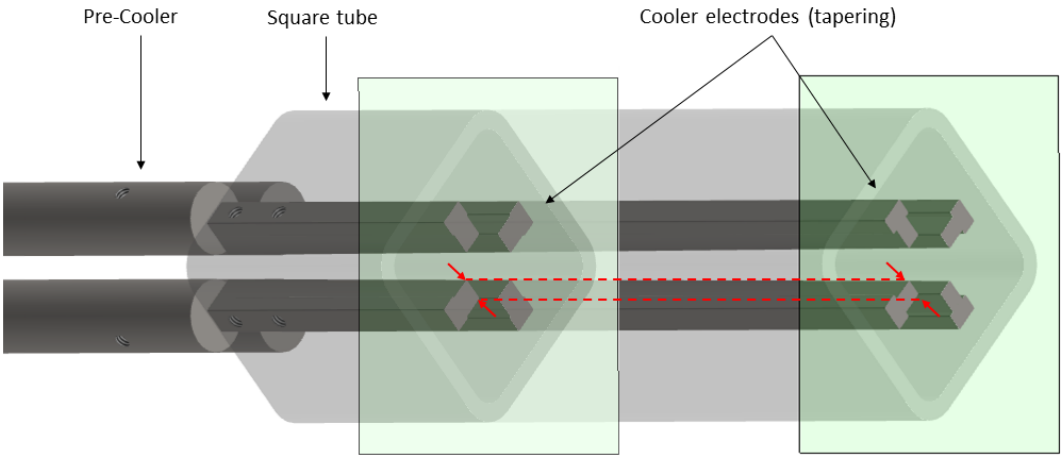

Figure 2.13: Sectional view of the special tapering electrodes of the cooler responsible for creating the potential gradient required for guiding ions towards the buncher. The square tube enclosing the electrodes is held at ∼(-100) V, and the width of the electrodes controls the penetration of this potential, gradually increasing as the width decreases moving towards the buncher.

2.4.4 Ion buncher

The buncher comprises of three sets of wedge-shaped quadrupoles, with apertures both upstream and downstream of it. The buncher constitutes the potential well of the conventional Linear Paul Trap shown in Fig. 2.7. Cooled ions from the cooler section are directed towards the buncher where they are temporarily stored upstream of the entrance

aperture. During this time, laser fluorescence spectroscopy is performed according to the scheme described in Section 1.5.

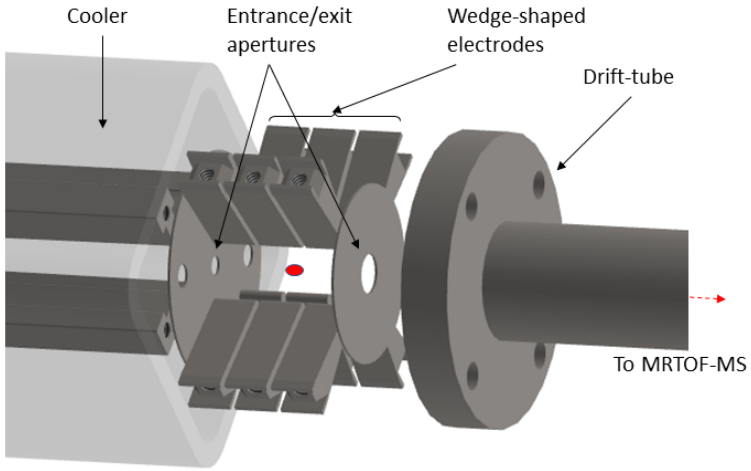

Figure 2.14: Stripped down view of buncher showing the electrodes involved in ion confinement. Apertures apply axial confinement, while wedge-shaped electrodes apply RF potential for radial confinement. The wedge shape adopted here facilitates greater access to the center of the trap while minimizing the scattering of the laser off the electrodes. Shown in red is a depiction of the ion bunch at the center of the trap, which after laser fluorescence spectroscopy, is transferred to the MRTOF-MS via the drift-tube.

The motion of the ions in the buncher is regulated by the entrance and exit apertures (see Fig. 2.14). Their voltages are controlled to allow the intake of ions inside the buncher for trapping and then eject the ions to transfer to the MRTOF-MS. The operation of the buncher is described in detail later in Section 3.4. The wedge-shaped electrodes of the buncher are designed to allow for large opening angles to reduce the scattering of laser light on the electrodes while allowing efficient fluorescent light collection by a PMT placed vertically above the buncher [79].

After spectroscopic identification, ions are then transferred to the downstream MRTOF-MS through a drift-tube used to bring the ion bunch energy to ($\sim 2\,\mathrm{keV}$) required for the operation of the MRTOF-MS [92]. The MRTOF-MS then separates the ions in the bunch

through repeated reflections by electrostatic mirrors at its two ends. Ions are time separated after several reflections based on their corresponding mass-to-charge ratio and hence provide accurate information of ion masses.

Chapter 3

Linear Paul Trap Assembly and Electronics Developments

The major focus of my Master's work is the assembly and commissioning of the Linear Paul Trap setup at the Brunner Neutrino Lab (BvL), McGill University. Fig. 3.1 shows the present status of the commissioned setup with annotations that show the relative positions of the LPT's composite segments inside the vacuum chamber. Section 3.1 describes the vacuum parts and devices used. Section 3.2 briefly discusses the assembling of the electrodes for the LPT. Section 3.3 describes the internal connections, electronics, and voltage switches used. Lastly, Section 3.4 discusses the different phases of operation of the LPT buncher - Trapping, Transfer, and Ejection.

3.1 Vacuum System

The LPT setup is designed with the goal of detecting a single ion. In order to prevent ion losses from collisions with background gas, the entire setup needs to be made with material of low outgassing rates. For the vacuum chamber, stainless-steel components with ConFlat copper gaskets are used. All components used for the vacuum chamber were sonicated with

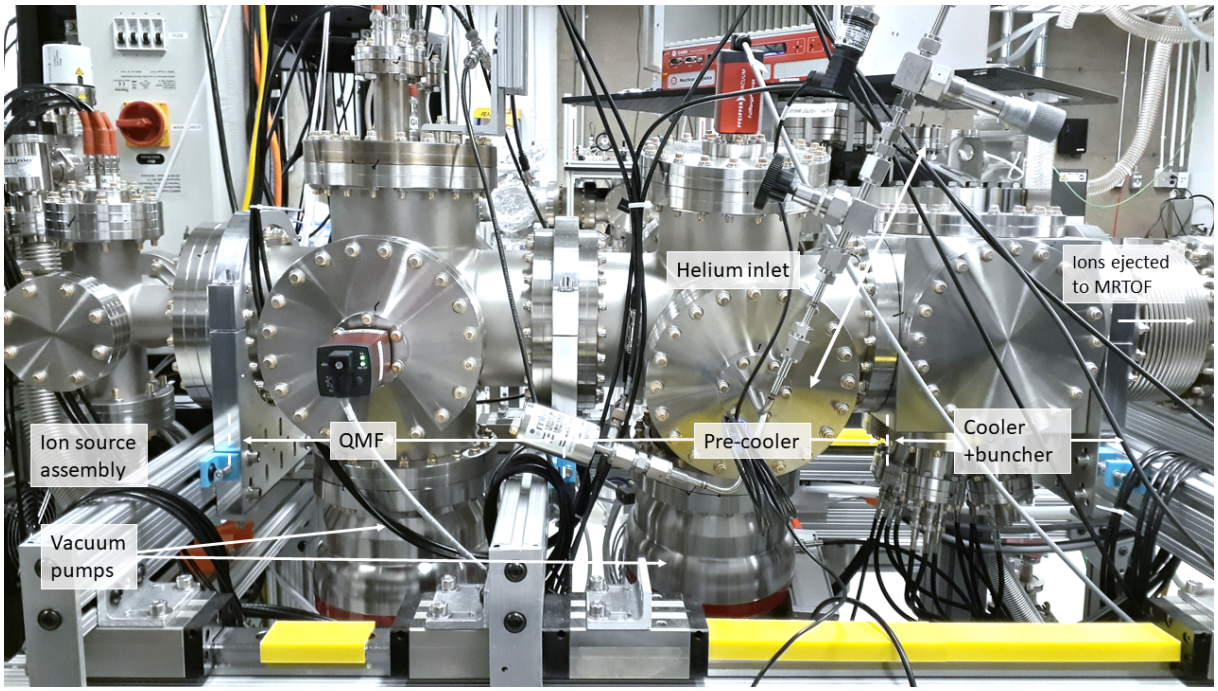

Figure 3.1: Picture of the commissioned LPT setup. The picture shows the crosses housing the ion source assembly, QMF, pre-cooler, cooler, and buncher. Additionally shown are the vacuum pumps installed on the two crosses for differential pumping between QMF and cooler. Each of the two crosses also has full-range pressure gauges installed. The QMF cross and the cooler cube have special multi-port flanges with SHV-feedthroughs for connection to electrodes inside the vacuum chambers. Also shown is the helium line used to supply buffer gas to the cooler.

acetone and again with isopropanol to remove potential dirt and grease resulting from either machining or handling. The cleaning protocol followed for all vacuum components is given in Appendix A.

Fig. 3.1 shows the LPT setup, which is enclosed by two CF 8" 6-way crosses (QMF, Pre-cooler) and a CF 8" cube (Cooler, Buncher). All parts are Ultra-High Vacuum (UHV) compatible, including the copper gaskets used to seal flanges. Fig. 3.2 shows a schematic overview of the LPT Vacuum system along with the gas line for supplying the helium buffer

gas. Two turbo-molecular pumps (TMP)[1] (TPM001, TMP002) are used to pump down the setup to high-vacuum. The TMPs are connected to a common roughing pump (ACP 15, Pfeiffer Vacuum) which evacuates the chamber to the ($\sim 10^{-2}$) mbar pressure range. The pressure inside the two 6-way crosses is measured using Pfeiffer full-range gauges (FRG005, FRG007) that operate from atmosphere pressure to ($\sim 10^{-10}$) mbar. Additionally, automated valves are installed to both TMPs for venting the vacuum chamber with dry nitrogen when required. Refer to Table E.1 for description of the mentioned vacuum hardware.

Of the two tubings provided at the feedthrough at the pre-cooler chamber in Fig. 3.1, one connects to a pressure transducer (BPT009 in Fig. 3.2) for monitoring the helium pressure inside the cooler. The other connects to a VCR valve, then to a needle valve to regulate the helium flow rates as per requirement. The needle valve is further connected to another high-pressure gauge and a Swagelok valve for measuring pressure and sealing the helium line respectively. The required helium flow rate (r_{He}) is calculated using the buffer gas pressure required in the cooler, pump speed, and conductance of internal apertures in [79].

The internal connection to the helium feedthrough is shown in Fig. 3.3. A (1/4)" tubing connects the inside of the cooler through the holder (shown in Fig. 3.3) to the helium tank on the air-side. On the air-side, a needle-valve along with a flow monitor regulates the flow of helium into the cooler ($\mathrm{r}_{He} \approx 3.57$ l/s).

3.1.1 Leak checking

After installation of the LPT components and wiring and closing all flanges, the entire setup was tested for leaks. Leaks in vacuum systems can occur in several forms, with the main categories being listed below:

1. Leaks due to detachable connections such as gauges, flanges, and feedthroughs.

2. Leaks due to mechanical defects such as cracks or pores.

[1] HiPace 700, Pfeiffer Vacuum

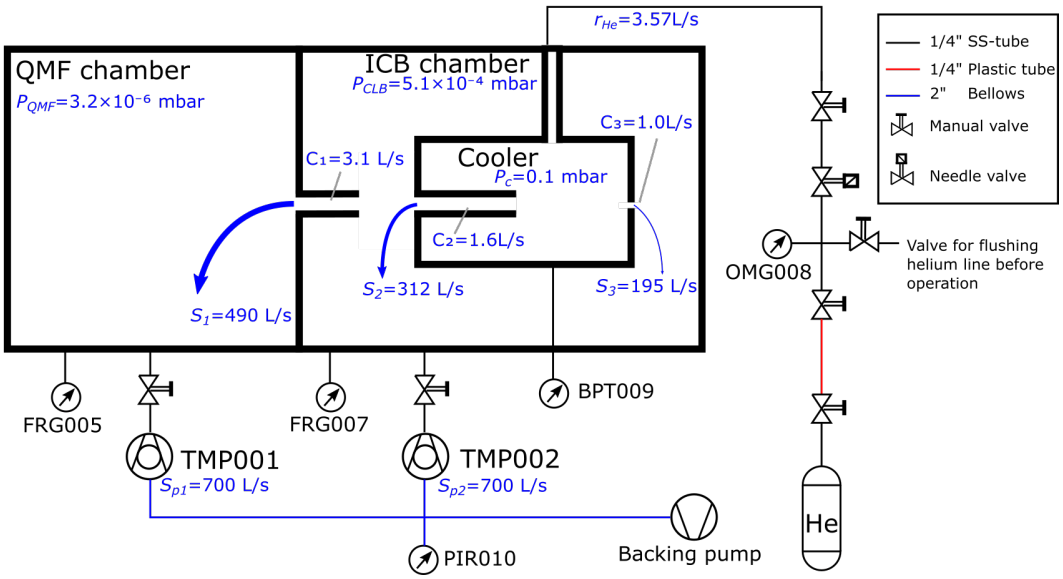

Figure 3.2: Schematic of the LPT Vacuum system. The sizes of the apertures, pump speed, and associated conductances are used in calculating the helium flow rate required for the required pressure in the cooler (Retrieved from [79]).

3. Virtual leaks, resulting from trapped air pockets resulting in continual outgassing.

Type-1 leaks are minimized by using new copper gaskets to form the vacuum seals with the flanges. Following the correct bolt tightening pattern ensures even sealing between the copper gasket and knife-edge on the flanges. Type-2 leaks are not as common as Type-1 as most of the setup uses loose commercial parts. Type-3 leaks are avoided through the use of vented bolts for fastening components and venting tapped holes.

Before initiating testing, the system was allowed to pump down for an entire weekend to ensure at least a high vacuum ($\sim 10^{-7}$ mbar) is achieved at the time of testing. Testing for leaks involved using a leak-checker machine, a mass analyzer calibrated to detect helium. The leak-checker was connected near the roughing pump since the roughing pump is common to both the TMPs. The test was focused on detecting any leaks from detachable parts. Helium gas was sprayed at all interfaces, and helium rate was monitored. Ultimately, no helium leak

(a) Image of the assembled cooler. Shown here is the cooler fixed to its holder (black) and tubing to connect the helium line to the cooler.

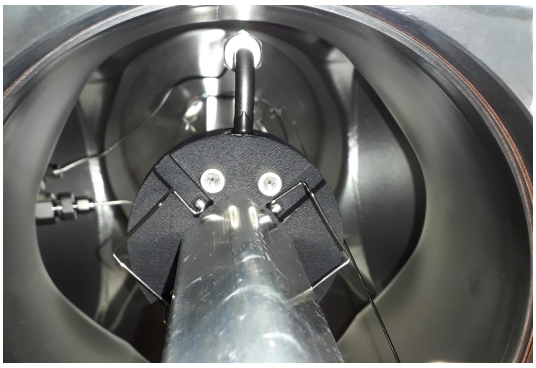

(b) Inside view of the vacuum chamber showing the cooler. The helium buffer-gas feedthrough connects to the outside helium line shown in Fig. 3.1.

Figure 3.3: Helium buffer gas feedthrough and tubing.

($> 10^{-12}$ mbar l/s) was detectable.

3.2 Electrode Assembly

The parts for the electrodes and their corresponding holders were designed by Dr. Yang Lan as part of their Ph.D. thesis [79]. The assembly was done as part of this thesis. Attention was paid to cleaning the parts and a clean assembly. Fig. 3.4 shows the components of the QMF, pre-cooler, and buncher prior to assembly. Wiring of the electrodes was done in parallel to the assembly before installation in the vacuum chamber. Fig. 3.5 shows the LPT sections before they were installed into their respective vacuum chambers and wires connected to the electrodes.

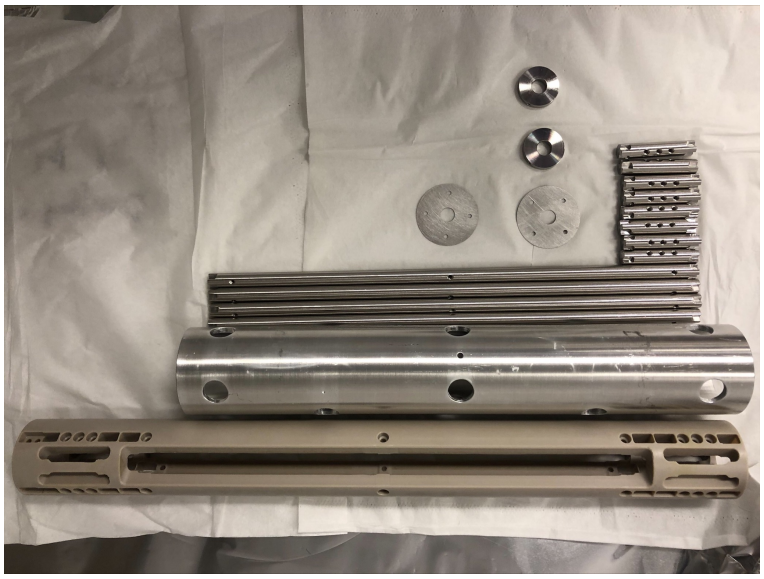

(a) Photograph of cleaned QMF components prior to assembly: QMF holder, QMF shield, quadrupole electrodes, lenses, and apertures.

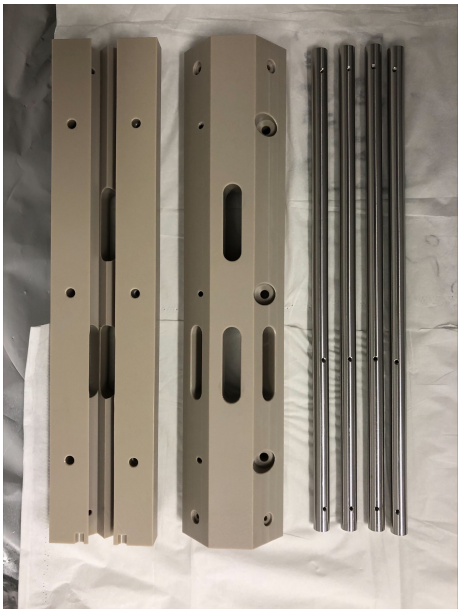

(b) Pre-cooler components: quadrupole electrodes and holder.

(c) Buncher components: wedge-shaped electrodes (3×4), aperture, ceramic spacer, buncher holder, and drift tube.

Figure 3.4: LPT components [Images taken by Xiao Zhang, prior to assembly].

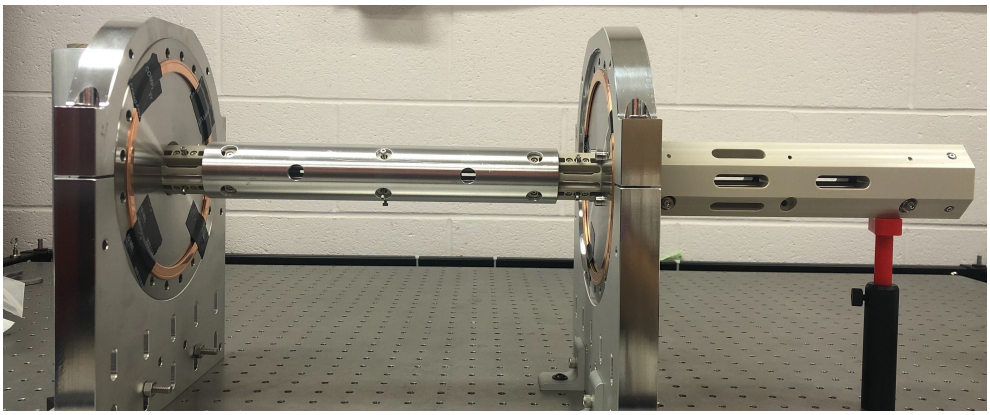

(a) Picture of assembled QMF (supported between the flanges) and pre-cooler (supported between the flange and an optical mount).

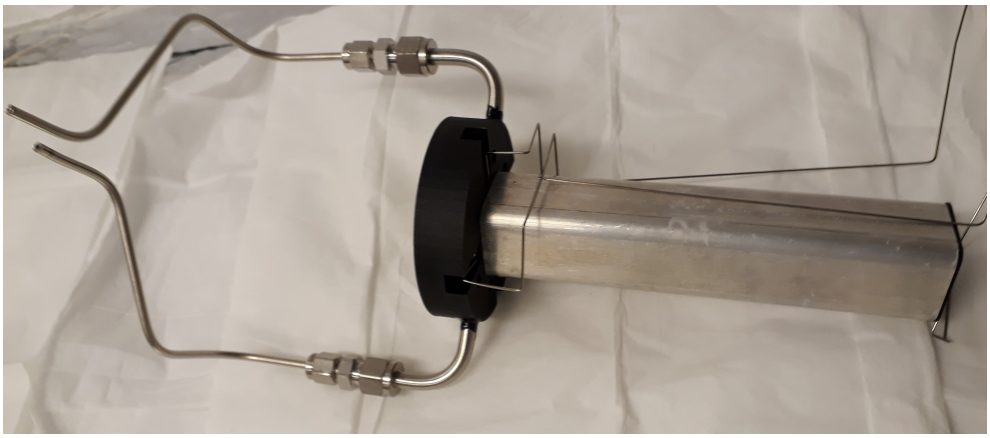

(b) Picture of the assembled cooler with tubing for helium buffer gas.

(c) Picture of buncher installed into the holder (black) with a drift-tube connected downstream.

Figure 3.5: Pictures of LPT sections [Images taken by Xiao Zhang and author prior to assembly of vacuum chambers].

3.3 Electronics

Most of the quadrupole electrodes in the LPT setup require DC potentials coupled to an RF voltages, as discussed in Chapter 2. The values for these voltages depend on the stability parameters mentioned in Eqn. 2.19. Thus, the operation voltages can be calculated for a given choice of these parameters. For Ba-tagging, the ion of interest is $^{136}Ba^{+}$ with $m = 136\,\mathrm{u}$. The design for the quadrupoles puts the electrode-axis spacing $r_o \approx 4\,\mathrm{mm}$. For an operating frequency of 1MHz and q parameter value of 0.5, the required RF amplitude is,

$$V = \frac{q \times m r_o^2 \Omega^2}{4Q} \quad \text{(from Eqn. 2.19)}, \tag{3.1}$$

$$= \frac{0.5 \times (136\mathrm{u})(931.5\mathrm{MeV}/c^2)(4 \times 10^{-3} m)^2 (2\pi \times 10^6 s^{-1})^2}{4e} \approx 111\,\mathrm{V}. \tag{3.2}$$

The above calculation shows that the requirements for operation require an RF voltage higher than the output of conventional waveform generators. Thus, RF amplifiers are used to amplify the waveform amplitude. The amplified waveforms are then transmitted to electronics boxes specific to the section of the LPT setup, i.e., the QMF box for all QMF related elements and the Ion Cooler and Buncher (ICB) box for all elements downstream from QMF, which constitutes the pre-cooler, cooler, and buncher quadrupole electrodes and apertures. Fig. 3.6 gives a schematic overview of the connections from each of the electronic boxes along with power supply units, waveform generator and RF power amplifiers used in driving the setup. The separation of electronics into the QMF and ICB boxes is due to the difference in the RF requirements. The QMF electrodes require a more flexible operation range for scanning different ion masses, while the ICB electrodes require higher stability but a smaller range of parameters.

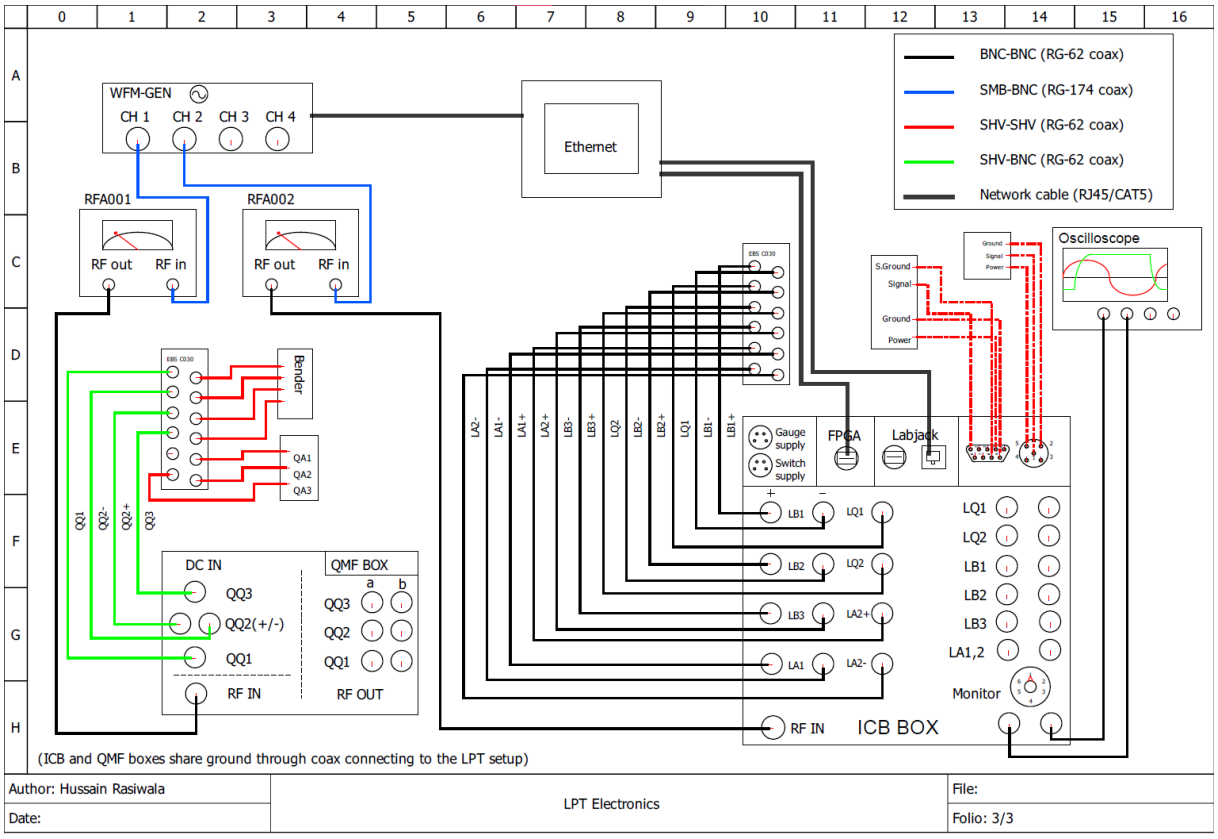

Figure 3.6: Wiring diagram for the LPT setup showing all the electronic equipment used for supplying RF/DC voltages, amplifiers for the RF potential supplied by a commercial waveform generator, and wires connecting the different components. The naming of the connections follows with the naming convention adopted in Table D.2. Description of the electronics is provided in Table E.1.

3.3.1 Wire routing

The vacuum-side wiring for all electrodes was done using 20 AWG bare stainless-steel welding rods as the conductor. The wires have great physical rigidity and lack electrical insulation, which reduces outgassing. The rods were bent into shape before installation because, in contrast to copper wire bending, stainless-steel rods are significantly more rigid and almost impossible to bend inside the vacuum chamber. Hence suitable shapes were made for the

required connections while keeping the overall wire length as small as possible. Additionally, all wires belonging to the same quadrupole were equal in length to minimize any difference in capacitance which could cause an imbalance in the RF signals within the quadrupole. In order to ensure balance within the same diagonal pair (either between '+' to '+' / '-' to '-'), a t-connection was made in the middle through spot welding another piece to ensure equal lengths (see Fig. 3.7).

Figure 3.7: Images of the cooler section prior to installation. Left: shows the jumper wire connecting opposite electrodes of the cooler quadrupole. Right: shows the t-connection made using a spot welder for the cooler wiring. The other electrode pair is connected with an identical jumper wire with a t-connection.

All connections were screwed to the electrodes. The buncher is an exception, where doing so was impossible due to its small size and clustered connections. Instead, crimp-connectors were used to make contact through the hole of the vented screws holding the wedge-shaped buncher electrodes (see Fig. 3.8).

SHV-SHV feedthroughs are used to couple the voltages into the vacuum chamber connected via push-on connectors. The air-side wiring is shown in Fig. 3.6. All cables connecting the feedthroughs to the corresponding boxes (QMF-box, ICB-box) are made from low impedance RJ62 cable.

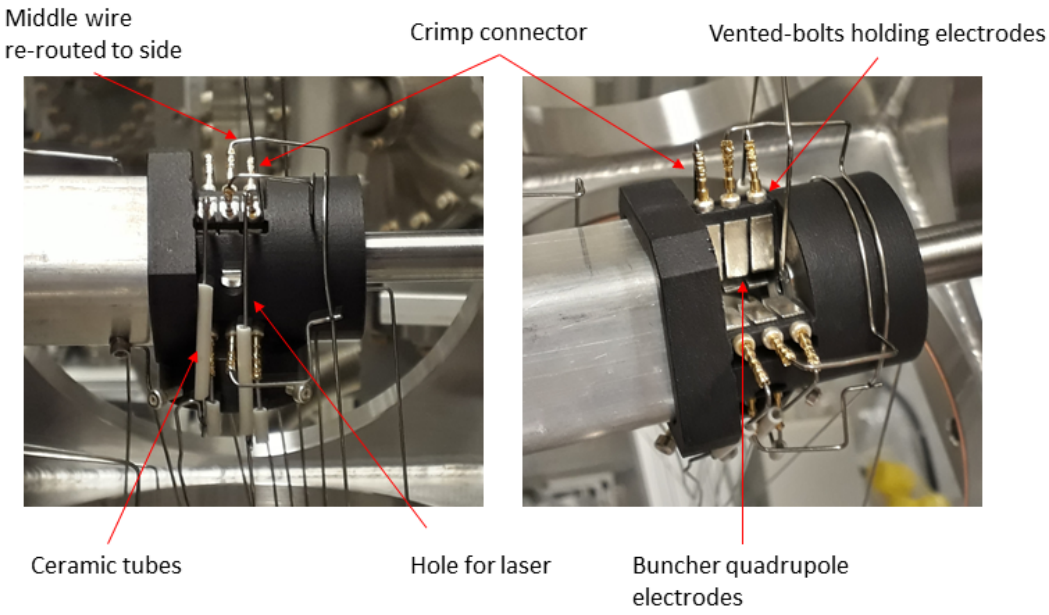

Figure 3.8: Images of the buncher with the wires connected to the quadrupole electrodes using crimp connectors (golden in color). The connector is wedged into the venting hole of bolts holding the wedge-shaped electrodes of the buncher. Wires for the buncher are routed from the under-side to keep the top side open for the collection of fluorescence light. The wires for the middle quadrupole are routed from the side to keep the laser path clear. Ceramic tubes are used for some connections to prevent shorting of adjacent wires.

3.3.2 QMF electronics

The QMF-box contains a transformer core for providing additional gain in RF amplitude while supplying RF to the three quadrupole segments of the QMF (QQ1,2,3 in Fig. 2.9). The RF is then coupled to a DC potential through capacitors, as shown in the electronics layout in Fig. B.2 in Appendix. The a/b notation used alongside quadrupoles indicates the polarity of the waveform. All outputs with suffix 'a' are in-phase with the waveform generator output, while all outputs with suffix 'b' are (180°) out of phase. The output of the DC-coupled RF voltage is connected to SHV bulkheads installed in the box (see Fig. B.1). The second quadrupole has two separate DC voltage inputs. This is to apply differential DC potential

for filtering ions, while the QQ1 and QQ3 quadrupoles are employed only as ramps for the RF potential, as explained in Section 2.4.2.

3.3.3 ICB electronics

The ICB box supplies voltage to all the electrodes downstream from the QMF. In addition to the DC-RF coupling, the ICB-box also houses circuitry and instrumentation that enables DC voltage switching and data acquisition. It also houses DC power supplies and a Field Programmable Gate Array (FPGA) module to control and operate the voltage switches. Refer to Fig. B.3 in Appendix B for images of the RF-DC electronics. All DC inputs are connected to the BNC-bulkheads while all outputs go to SHV-bulkheads installed on the ICB box. Also installed is a 2-pole 6-position rotary switch through which 10 RF/switched-DC outputs are routed. The outputs can be observed on an oscilloscope by setting the rotary switch to the corresponding position.

Voltages for the pre-cooler and cooler are coupled similarly to the QMF ramp quadrupoles. The RF potential is coupled with constant DC through a combination of capacitors and resistors and supplied to the quadrupole electrodes. The buncher apertures and quadrupoles, on the other hand, operate on switched-DC voltages. All switched DC voltages are two-state type, with an idle state and a switched state. The signal to trigger the change of state is provided by a FPGA module that controls the entire system's timing operation, i.e., LPT and MRTOF-MS. This is done to synchronize the operation cycle of the LPT with the MRTOF-MS cycle. Fig. B.4 shows the schematic of the electrical connections is similar to the scheme for QMF-box with the addition of voltage switches and two signal channels (EJECT, TRANSFER) coming from the FPGA module. Switching control is explained in detail in Section 3.4. Not included in the Fig. B.4 is an upgrade, a monitoring circuit, being developed to correct for any imbalance or lag in the voltages that may develop during operation. The circuit will come with a built-in multiplexer to enable

monitoring of all buncher voltages through periodic measurements of each voltage channel. To scan all multiplexer channels, the monitoring circuit will use a LabJack T7 module which is already installed for data acquisition of pressure gauges.

3.4 LPT Operation

The LPT setup has been assembled as part of this work and is being optimized for best performance. The ion source assembly described in Section 2.4.1 produces an ion current of about 5nA that gets injected into the QMF. The two lenses at the entrance function as an immersion lens to focus the incoming ions. The ions then pass through the QMF with relatively constant velocity due to the absence of buffer gas. Filtered ions make their way into the pre-cooler, where they begin slowing down under the influence of helium pressure, which gradually increases towards the cooler. Because the ions lose kinetic energy in collision with the buffer gas, the potential of the pre-cooler is held lower than the QMF. This prevents potential back-flow of ions, allowing only transmission in the forward direction. The next potential step is applied to the cooler segment, which has higher gas pressure ($\sim$0.01 mbar). As described in Section 2.4.3, in addition to the potential step, the cooler has a potential gradient along its length. Fig. 3.9 shows how DC potential varies along the axis of the setup to guide the axial motion of ions towards the trap. The first aperture peak blocks ions from entering the buncher continuously. Together with the gradient in the cooler, this peak facilitates ions to collect just outside of the buncher at the collection trap (see Fig. 3.9), awaiting transfer. From here, the ions are transferred into the buncher periodically, where laser fluorescence spectroscopy is performed on the ions. The ions are then ejected from the buncher to the MRTOF-MS.

LabVIEW programs were developed to control all variable parameters for operating the setup. This includes programs to control the settings of the function generator, enable real-time scanning of RF waveform parameters, and perform parameter scans for the QMF.

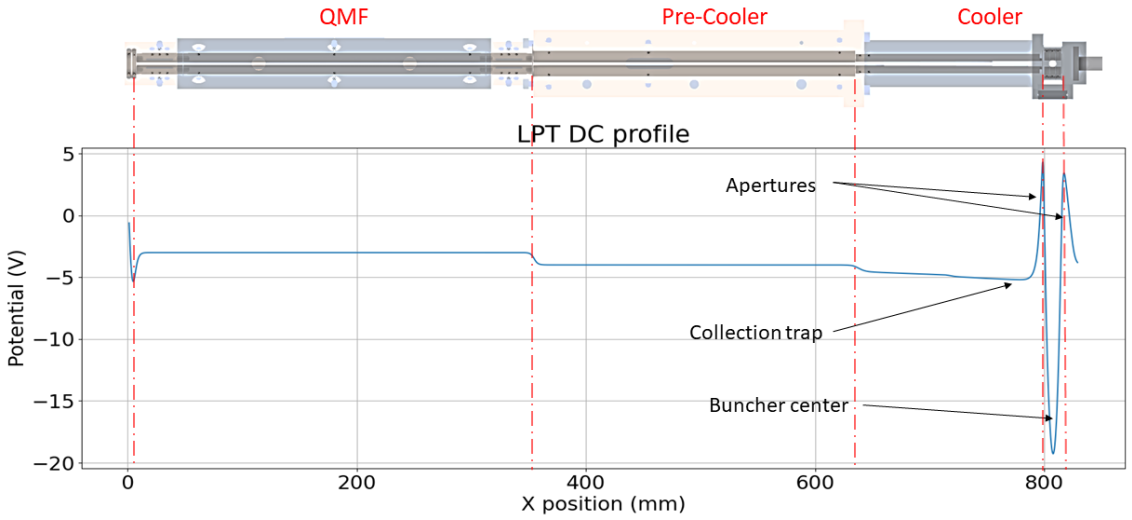

Figure 3.9: DC potential profile along the axis of the LPT setup. The DC potential is held constant inside the QMF and pre-cooler and only changes when moving from one section to other. The DC potential in the cooler has a gradient due to the tapered electrodes used, which directs the ion motion towards the collection trap prior to transfer to the buncher.

During operation, the QMF potentials will be calibrated to filter out all ions except $^{136}Ba^{+}$ ions. The operation of the buncher is sub-divided into 3 phases: Trapping, Transfer, and Ejection. The buncher goes through these three phases during a single operation cycle. The cycle-time (t_c) shown in Fig. 3.10 is the duration of one cycle of trapping and ejecting ion to the MRTOF-MS. t_c is fixed at around 1 ms, equal to the time duration required for the MRTOF-MS.

The three phases are described in Fig. 3.11, showing the potentials during each of these phases and their corresponding role in the operation of the buncher.

3.4.1 Transfer phase

The transfer phase corresponds to the loading of the buncher with ions from the cooler. Before the transfer signal arrives, the potential of the aperture (LA1) separating the buncher

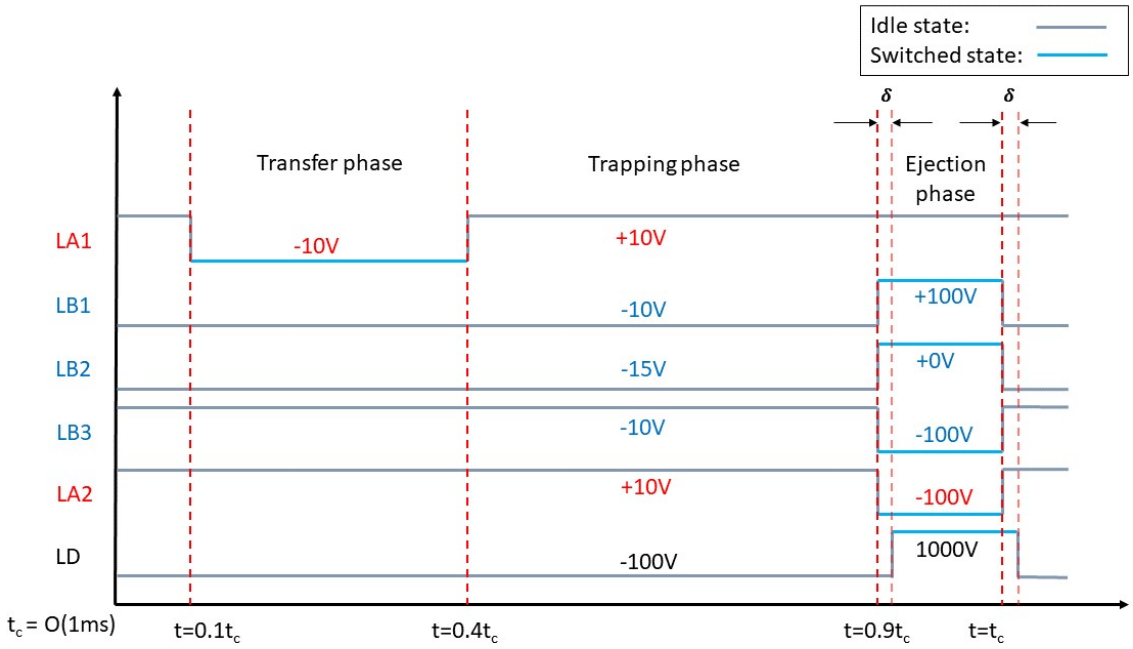

Figure 3.10: Timing diagram for the buncher operation. y-axis tracks the state of a given electrode depending on the time elapsed based on a cycle-time t_c

and cooler is held at a high potential. This enables the collection of ions in the cooler prior to trapping. The high potential prevents any ions already loaded in the buncher trap from escaping into the cooler. When the TRANSFER pulse arrives, the voltage on the aperture is lowered to the buncher potential to allow the entry of ions from the cooler as shown in Fig. 3.11. The duration of the TRANSFER signal is currently around 200-300 μs after which the potential for LA1 is raised back to its initial potential. This seals off the buncher and prevents the escape of transferred ions, marking the start of the trapping phase.

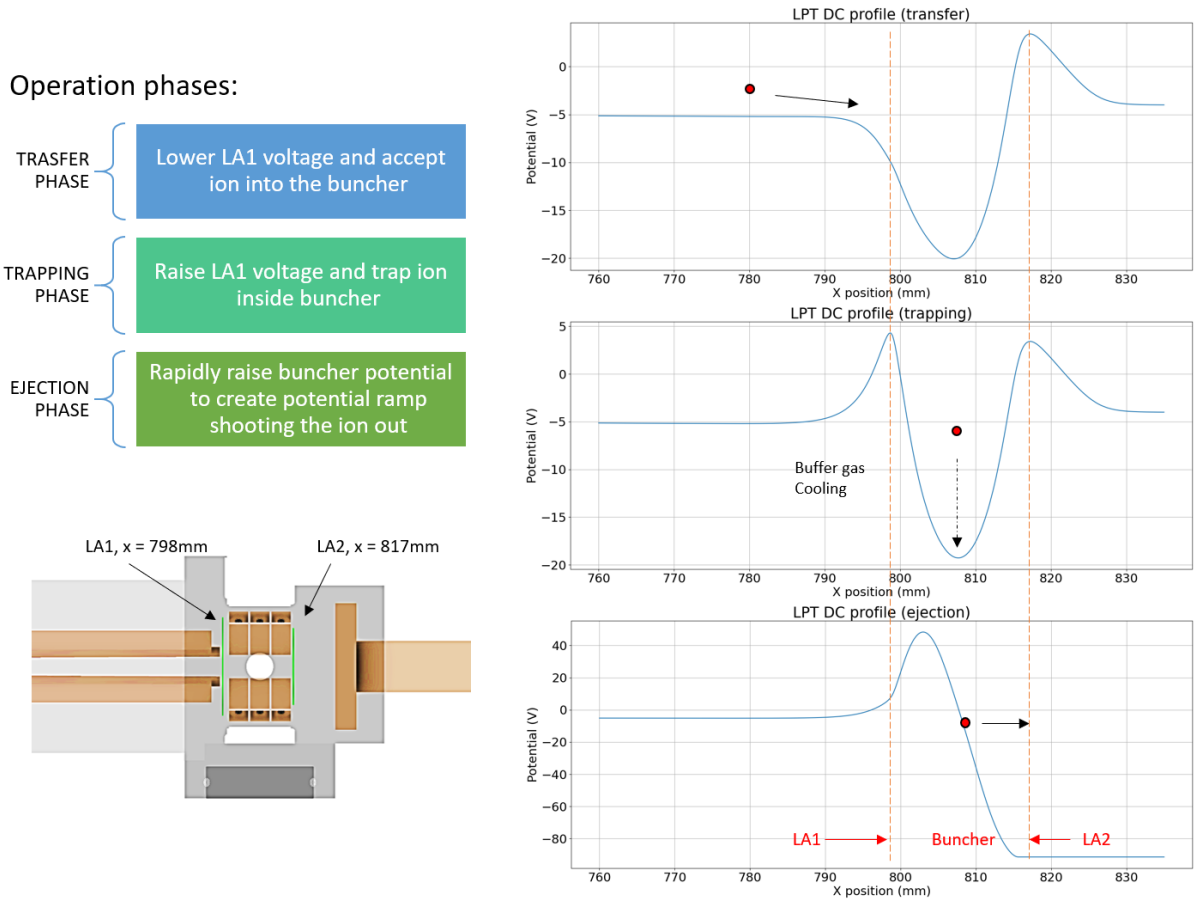

Figure 3.11: LPT operation scheme. The buncher electrodes operate with switched voltages to control the axial motion of ions. The three phases represent the three-stage manipulation of ions in order to trap them in the buncher for spectroscopic identification. The ions are simultaneously cooled and later transferred to MRTOF-MS with specific energy and low temporal spread.

3.4.2 Trapping phase

After the transfer, ions are stored inside the buncher trap, where they continue to cool down through collisions with the helium buffer gas. The holder for the buncher electrodes has a cavity to allow visible access to the trap center. This is required for laser fluorescence

spectroscopy. The potentials of the buncher segments are therefore set to create a potential well exactly at the center of the buncher. The laser fluorescence scheme, described in Section 1.5, is then followed to search for the presence of Ba^+ ions. In addition to trapping ions for fluorescence studies, the buncher also cools the ions into a tight bunch (hence the name - Buncher). In this phase, the voltages remain constant, and due to the low spatial and temporal spread requirement, the ions are cooled here for as long as possible ($\sim$ 500 μs).

3.4.3 Ejection phase

As the final phase in the operation cycle of the LPT, the ejection phase is responsible for unloading the buncher. The potential inside the buncher is rapidly raised (with transition time $\sim$ 0.1-0.3 μs) to create a potential ramp. The left buncher quadrupole (LB1) is raised to a voltage as high as 100 V while the right buncher quadrupole (LB3) is set to (-100) V. The potential ramp (shown in Fig. 3.11) accelerates the ion bunch out of the buncher and into the drift tube. δ is a time delay added to the EJECT pulse to allow ions ejected from the buncher to reach at least halfway through the length of the drift tube. When inside, the drift tube potential is raised to about 1 kV from (-100) V. This gives the final potential boost to the ion before arriving at the MRTOF-MS. The potential is set to a very specific voltage that defines the energy of ions in the ion bunch. This is important because it impacts the MRTOF-MS operation. At the exit of the drift tube, the ion bunch goes from $\sim$1 kV potential to ground level and hence gains an additional 1keV in kinetic energy. The exact kinetic energy, 1163 eV, is based on MRTOF-MS simulations, a fraction of which is imparted in the buncher and remainder in the drift-tube. This two-stage acceleration scheme helps in controlling the location of the time focus plane, which further supports the resolution of the MRTOF-MS (see [93] for discussion about the time focusing of the ion beam).

Chapter 4

Operation Optimization and Simulations

Simulations were performed to optimize the voltages used for operating the LPT setup together with the ion source assembly and bender. The SIMION software (version 8.1), a field and particle trajectory simulator, is used for simulating the entire setup. The software uses techniques like Runge-Kutta and finite difference method to solve Laplace equations and to track particle position and trajectory. The field potential is iteratively calculated at all points in the geometry defined by the potential arrays (PA). PAs are a 2D/3D grid that spans the entire defined geometry and are used for recording the potential and defining electrode shapes (see their online documentation [94] for more details). The simulations use geometry files, coded in SIMION-specific syntax, that define the position, shape, and size of the electrodes. Simulations discussed below are based on the design developed as part of [79] and build on it to optimize the operation voltages and switching times. Sections 4.1 and Section 4.2 present simulation results that determine the appropriate operating voltages, while Section 4.3 covers the simulation of ion cooling and the subsequent effect on the phase-space distribution of the ions.

4.1 Ion Source Optimization

The design and motivation for the ion source were given in Section 2.4.1. Simulations are performed with this source assembly and bender geometries to maximize their ion transport efficiencies. The theory behind the use of lenses and apertures is very well understood. Like ray optics, ion optics can be modeled through matrix formulation [95]. A problem with the direct implementation of the matrix formulation is that the theory requires the aperture diameter to be small compared to the inter-aperture spacing, which is not the case with this ion source assembly. Thus, the entire assembly is modeled in the SIMION 8.1 simulation software for optimizing the voltages to maximize transport efficiency.

The ion source assembly in the SIMION workbench consists of a source holder and five lenses, as shown in Fig. 4.1. The first two lenses are used to extract ions produced at the source holder towards the bender. The remaining three lenses are operated together as an Einzel lens as described in Section 2.4.1. In this arrangement, the outer lenses operate at the same voltage (V1) while the middle lens, which controls the focusing of the beam, operates at a different voltage (V2). There are two modes possible for an Einzel lens based on the choice of the two voltages. If the middle lens is held at positive potential relative to the other two (V2>V1), this configuration is called decel-accel mode. Conversely, if the middle lens is held at relatively lower potential (V1>V2), this is called the accel-decel mode since the ion will accelerate between the first and second lens and then decelerate towards the third lens. The second mode is preferred over the former because spherical and chromatic image aberration (the ion optics equivalent) are smaller [95].

The procedure adopted for optimizing electrostatic fields together with the bender is as follows.

1. Generate 100 ions at the source position uniformly distributed over a 2 mm radius circle centered at the source center, with constant energy of 0.01 eV and direction vector normal to the holder surface. The choice of the small kinetic energy of 0.01 eV

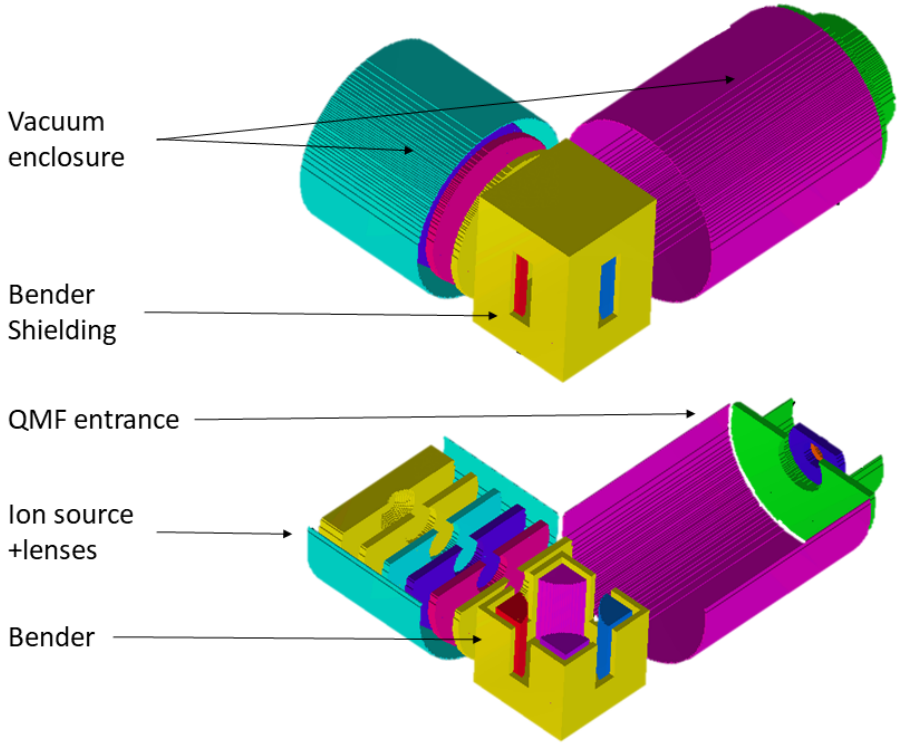

Figure 4.1: Simulation setup for ion source assembly. All elements are created using actual measurements along with a vacuum enclosure to terminate field lines.

is based on the fact that most of the ion energy comes from the bias voltage of 12 V applied to the source holder. All lenses are held at the ground potential here. The bender voltages are randomly sampled from an interval centered at the source holder voltage.

2. Using the set of potentials with the best performance for the bender, the lens potentials are now varied to focus the ion beam at the QMF lens located at the far end. For this step, the direction of ions generated is randomized over angles (0° to 90°) made with the source holder normal.

3. With bender and lens voltages optimized, QMF lens potentials are varied to maximize

ion acceptance into the QMF.

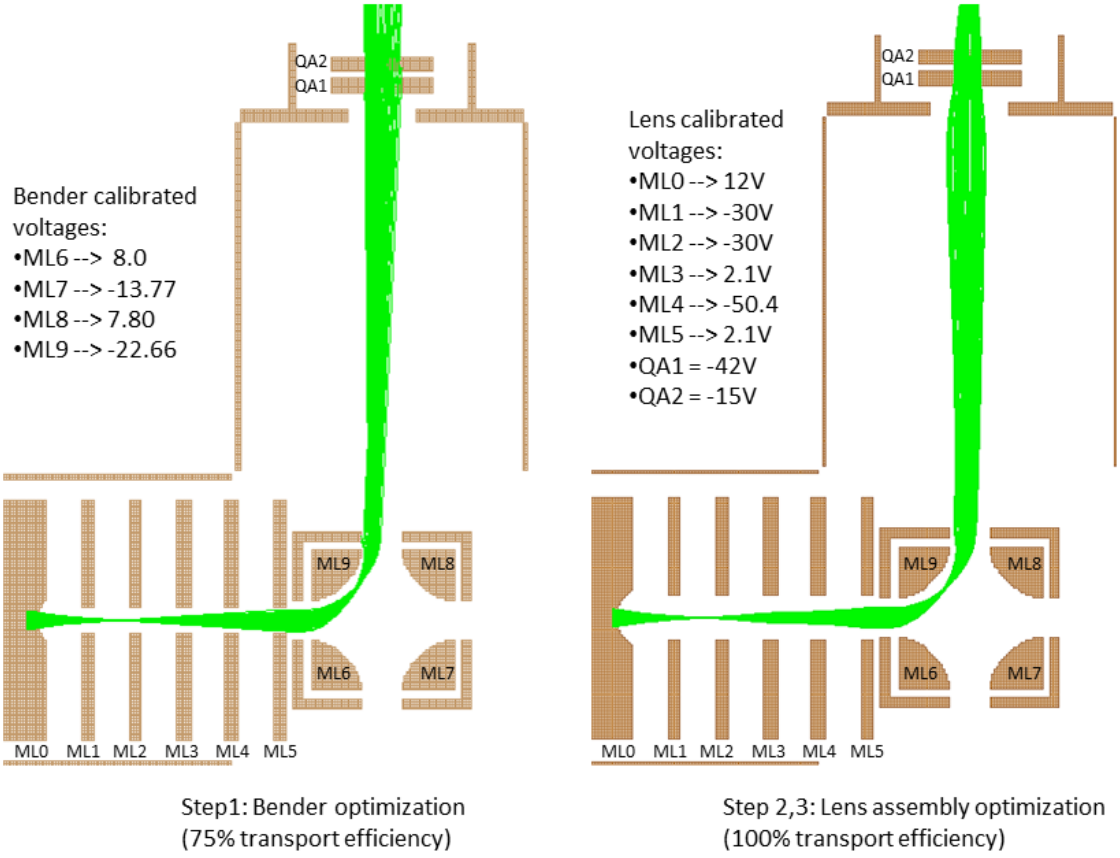

Figure 4.2: SIMION simulation for ion source assembly voltage-optimization. Green lines represent the trajectories of the 100 ions generated in a simulation run with the direction perpendicular to the source and kinetic energy of 0.01 eV. On the left is a visualization of the ion trajectories after Step 1 of optimization where all the lenses (including QMF lenses) are held at ground potential, source holder at 12 V potential, and only the bender voltages are varied. To the right is a visualization of ion trajectories after optimizing the source assembly and QMF lens potentials. Here the direction of the ions were randomized, and lens voltages varied to find optimal values that maximize ions entering the QMF.

Under normal operation, the source is able to produce ion currents of up to 5 nA. Therefore, even at a measured 10% transport efficiency, as discussed in Section 5.2, the source provides enough ions for performing all planned LPT tests. Additionally, following the completion of testing the LPT setup, the source assembly will be replaced by a CF 8" cross with a bender to couple the setup to the RF-funnel assembly upstream of the LPT setup. Hence, most of the simulation work will be re-done to optimize the best ion properties when they enter the QMF. Properties of the ions entering the QMF are shown in Table 4.1.

Ion property	Radial spread	Angular spread	Average kinetic energy
Value	3.5 mm	2.49° ± 1.38°	11.4 ± 1.56 eV

Table 4.1: Ion properties at the entrance of QMF calculated from the ion source assembly simulations.

These ion beam properties are then used in simulations for the LPT setup. The optimized voltage values in Fig. 4.1 are used to operate the source assembly and bender during actual operation.

4.2 QMF Simulations

LPT setup simulations are run using a monolithic geometry that contains all QMF and ICB electrodes. Two main aspects of the QMF studied using the simulations are the effect of balance of RF potentials and the transport efficiency when scanning over the trajectory parameters (a, q) from Fig. 2.5b.

4.2.1 QMF scanning

The stability of ion trajectories was introduced in Section 2.1 and extended in Section 2.2 for the QMF. Simulations were done to study the stable region of the trajectory parameter space for the current thermal ion source (Cs-133). The ions are simulated with properties based on ion source assembly simulations in Table 4.1. The RF and DC potentials defined in Eqn. 2.7 are iteratively varied across the entire region of ($q \in (0, 1.1)$, $a \in (0, 0.25)$) related to the potentials by Eqn. 2.19. Ions are allowed to traverse the QMF, and the number of ions that make it into the pre-cooler is used to compute the transmission efficiencies shown in Fig. 4.3.

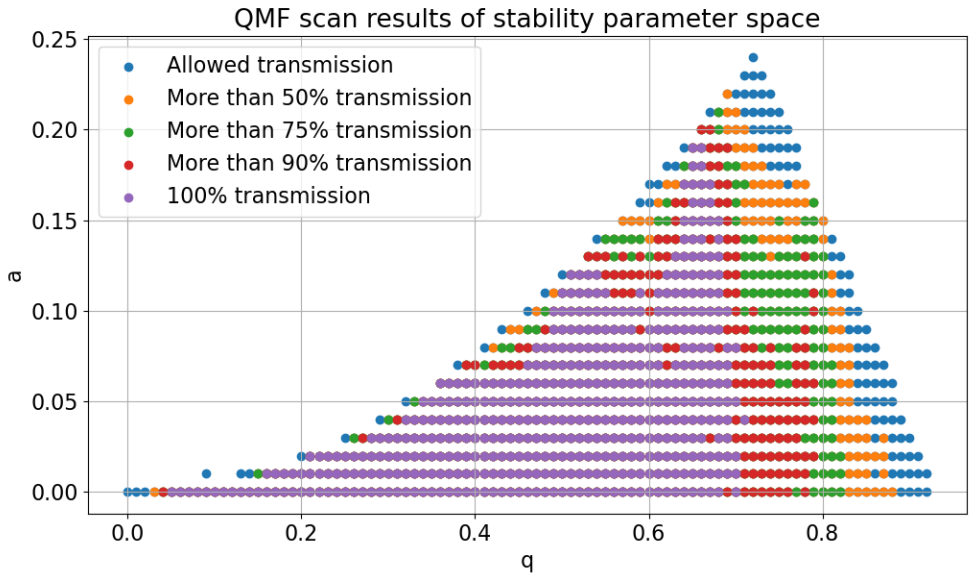

Figure 4.3: Results from simulations exploring the stability parameter space for the QMF for the Cs-133 ion source. The overall shape of the stability region follows well the one expected from theory (see Table 4.2), but due to the finite size of the QMF, certain regions have better transmission efficiency. The points in blue (allowed transmission) correspond to (a, q) values with at least one ion making it across the QMF and into the pre-cooler. Regions with higher ion transmission are highlighted similarly.

Parameter	q, tip region	a, tip region	q, maximum
Theory [79]	0.706	0.237	0.908
Simulation	0.72	0.24	0.92

Table 4.2: Comparison of results from QMF simulation compared with theory. The parameter (a, q) at the tip region of the stability regions and the maximum q value are compared.

The results of these simulations compare well with the expected region's shape and maximum (a, q) values. This can be seen by the comparison of the (a, q) values in Table 4.2, between simulations and theoretical values. Deviations from theory are observed which mainly arise due to the finite size of the quadrupole but overall no distortions in the stability region were observed.

The theory developed in Section 2.1 is based on an ideal ion guide that assumes an infinite length guide. However, the studied QMF is only 34.4 cm long. Therefore, losses in transmission can be expected for the outlying regions of the stable parameter space, as is seen in Fig. 4.3. Based on these results, high DC and RF voltage settings are more prone to losses. The different colored regions in Fig. 4.3 help determine the transmission to be expected for a given setting of the DC and RF potentials, as well as regions of high stability for operating the pre-cooler and cooler for the highest possible transmission efficiency. These simulation results are later compared to data collected from performing the experiment in Section 5.3.

4.2.2 RF balance

Apart from the choice of voltages, the performance of the QMF depends on the nature of the RF voltage, particularly the balance and jitter of the supplied voltages. Balance in the context of RF potential refers to the matching of potential in the quadrupoles. Imbalance

negatively affects the ion transmission as the resulting RF amplitude is smaller than the expectation. Jitter in the supplied voltages is controlled by the use of metal enclosures and coaxial cables where possible. For balance, simulations were done to study the effect of imbalance in RF voltage on ion transmission. The two kinds of imbalances investigated are shown in Fig. 4.4. The two types consider the following possibilities:

1. *Within a quadrupole*: between the two different RF phases.

2. *Between quadrupoles*: phase lag between adjacent quadrupole segments.

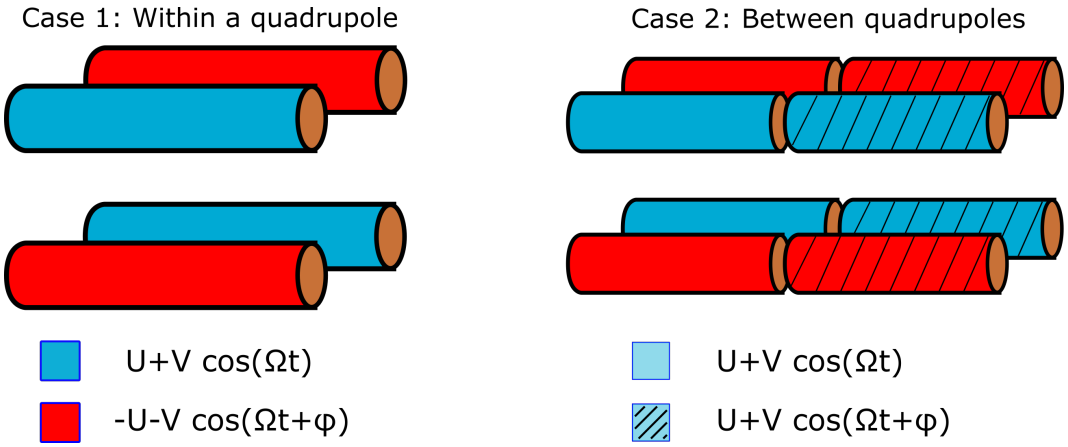

Figure 4.4: Schematic showing the two imbalance types and the method adopted to simulate the influence of imbalance. The red and blue colors indicate the polarity of the RF potential on the electrode pairs. Left: shows the first case where a phase difference is introduced between the two electrode pairs of a quadrupole. This phase ϕ is varied from 0° to 360° in increments of 2° per run. Right: shows the second case where a phase difference is introduced by the addition of a phase ϕ to the RF potential of an entire quadrupole (shown by dashed lines).

Several possible sources can introduce imbalance in the system, such as differences in connecting wire lengths or component capacitances. Before making corrections by adding electrical components to compensate for any imbalance, the level of imbalance that would

cause losses in the system was studied. These results provide an upper bound on the allowed level of imbalance without affecting the operation of the quadrupole, especially for the QMF. Pre-cooler and cooler are not as sensitive to imbalances since the buffer gas dampening improves, in general, the stability. The choice of potentials for operation is chosen as point 'A' in the stability diagram in Fig. 2.12. This also coincides with the simulated 100% transmission region shown in Fig. 4.3. Additionally, the ions generated at the QMF entrance are directed along the axis of the QMF without any angular spread to avoid losses from the instability of trajectories at the entrance. Thus, losses that occur are only due to RF imbalance. The simulation uniformly varies a phase ϕ in increments of 2°, added to the component being tested. The RF frequency used is 750 kHz, and amplitude (V) is set to 60 V, calculated using Eqn. 2.19 and q value of 0.5. The value of the differential DC voltage (U) is set to zero since higher transmission of ions is observed for $a = 0$. Taking the example for *within-quadrupole*, the applied voltages are

$$(+) \text{ Electrode pair} : \quad V \cos \Omega t, \tag{4.1}$$

$$(-) \text{ Electrode pair} : -V \cos (\Omega t + \phi), \quad \phi \in (0, 2\pi). \tag{4.2}$$

Simulation results shown in Fig. 4.5 show the variation of transmission efficiency as a function of imbalancing phase ϕ. Fig. 4.5a shows transmission losses above 60° phase lag within the two electrode pairs of quadrupole, which shows that under small imbalance, the transmission is unaffected. However, the balance between quadrupole segments is more important, as shown in Fig. 4.5b where losses are observed earlier at around 35° lag. Overall, both results show that the system allows for minor imbalances.

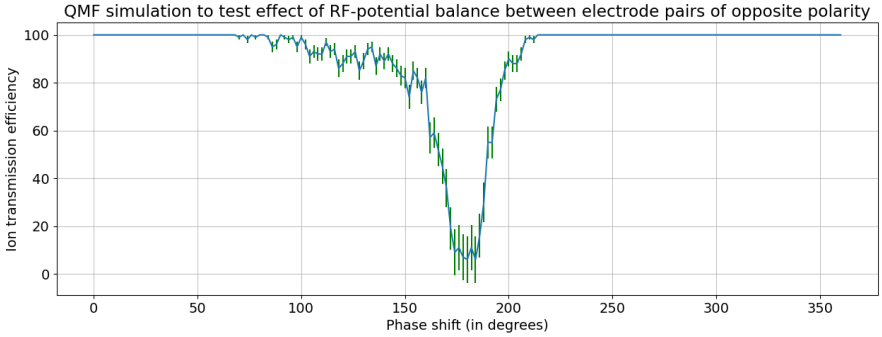

(a) Variation of ion transmission efficiency with changing phase difference between electrode pairs of different polarity in a quadrupole.

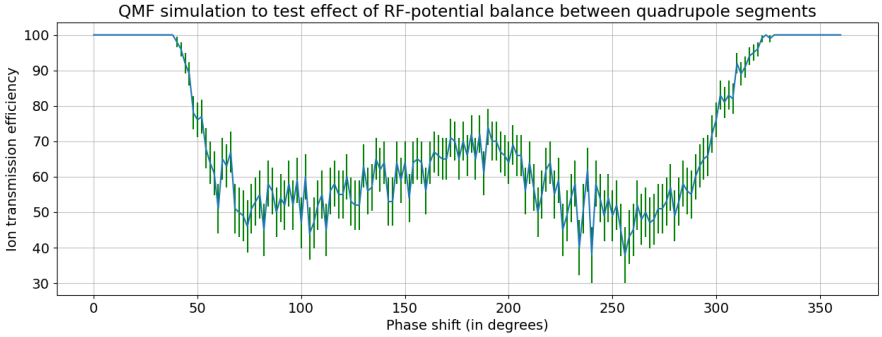

(b) Variation of ion transmission efficiency with changing phase difference between adjacent quadrupoles.

Figure 4.5: Simulated influence of RF potential imbalance on transmission efficiency.

4.3 Ion Cooling Simulations

The optimal buffer gas pressures required for the cooler and buncher were studied in detail in [79]. Ions being cooled lose kinetic energy to the helium buffer gas through collisions until they reach a steady-state. The steady-state energy corresponds to the minimum energy possible through a balance between the dissipation through buffer gas cooling and ion-heating by the RF potential [96]. A SIMION based hard-sphere model is used to simulate ion collision with background gas at pressure of 0.06 mbar (see [97] for detailed information on this model).

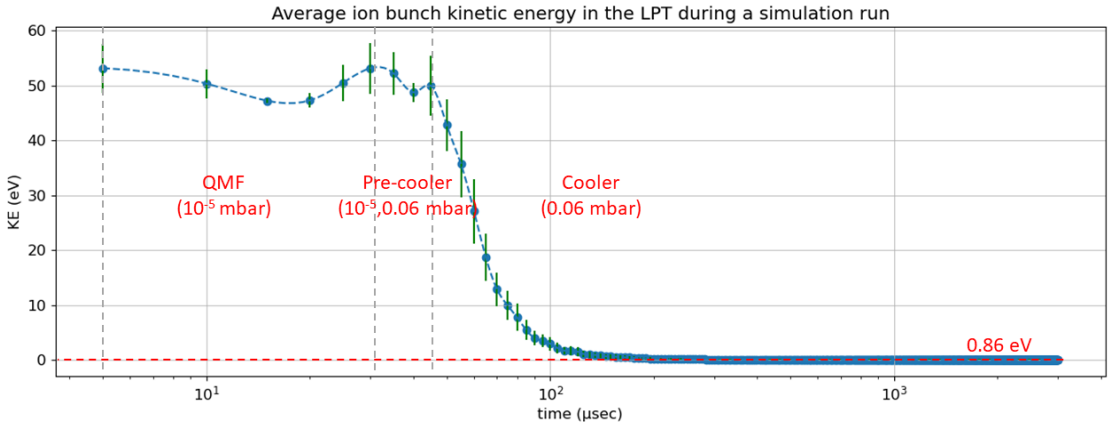

Figure 4.6: Ion bunch kinetic energy along the ion bunch trajectory. Group of 100 ions are injected through the QMF, and their average kinetic energy is plotted. The rising curves corresponds to the transition between sections. Here, the ions gain energy due to the DC potential being floated in order to prevent their back-flow.

The simulations for these segments investigate the time required for reaching steady-state and the distribution of the total cycle-time ($t_c = 1\,\text{ms}$) based on this requirement. Fig. 4.6 shows the variation kinetic energy varies as ions travel in the LPT setup. As mentioned in Chapter 3, each LPT segment (QMF, pre-cooler, and cooler) is being floated at sequentially lower potential to prevent backflow of ions (shown in Fig. 3.9). This results in ion acceleration and thus an increase in kinetic energy as ions transition from one section to the next. Inside the cooler, ions with 50 eV take under 200 μs to cool down.

Liouville's theorem introduced in Section 2.3 applies to the case of ion motion under the influence of electromagnetic forces, which are conservative in nature. Thus, buffer gas is used to reduce the spread of ion position and velocity. An efficient representation of the cooling efficiency of buffer gas is done by looking at ion emittance. As a quantity, emittance (ϵ) is the area (or more correctly, $\epsilon = (\text{Ellipse area})/\pi$) occupied by the ion beam in phase space of position and velocity. The emittance at different pressure regions of the LPT setup is shown in Fig. 4.7. A ellipse-envelope fitting function is used to calculate the phase space area (A),

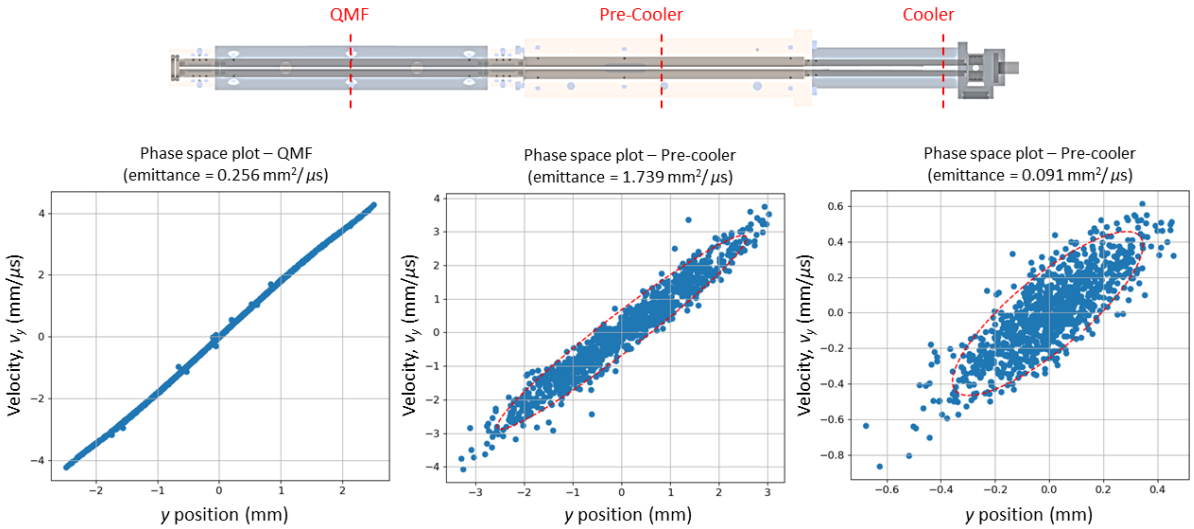

Figure 4.7: Phase space plot for 1000 ions traveling in the LPT. Ion bunch shows a strong correlation in the QMF coming from the ion initial definition. The lengths of the major and minor axes of the envelope ellipse are the eigenvalues of the data. These are also related to the standard deviations (σ) of the data along respective axes which is used here to plot the ellipse-envelope. The effect of cooling is apparent from the decrease in emittance upon going from pre-cooler to cooler.

based on Principal Component Analysis (PCA) method [98]. It calculates the major (a) and minor (b) axis length of the ellipse through the eigenvalues of the covariance matrix of the data points. Since $A = \pi ab$, $\epsilon = A/\pi$, with the length of the major and minor axes know, emittance is simply $\epsilon = ab$.

Ions generated show a strong correlation in the QMF since there are no non-conservative forces acting on the ions. On the other hand, we see a larger spread in the pre-cooler due to collisions with the helium gas. After about 500 μs in the cooler, the emittance significantly decreases. Not included in Fig. 4.7, is the buncher where transferred ions are further cooled to form an ion bunch with very low spatial and temporal spread. Low variance in ion parameters ensures that ions arrive at the MRTOF-MS at the same time and with minimum energy spread once ejected.

Chapter 5

Data and Results

Commissioning of the LPT setup is still ongoing at the time of writing this thesis. This chapter covers the results from the system checks and calibration. Section 5.1 covers initial tests of the QMF and ICB electronics. Section 5.2 summarises results and proceedings in the operation of the ion source and ion current measurements at the different segments of the LPT setup. Section 5.3 covers the tests of the QMF electronics and scanning capability. Tests involving buffer gas are not available, they are planned to be performed starting Fall 2021.

5.1 Electronics Check

An overview of the electronics used in operating the LPT setup was given in Section 3.3. Before the tests planned for the setup, all the connections were checked and tested. In addition to checking the connections and polarity, the quality of the signals being used was also tested as it directly affects the performance of the setup.

5.1.1 RF balance

The effect of RF balance on ion transport efficiency was studied in Section 4.2 for the entire range of phase shifts between different pairs of elements. Measurements shown in Table 5.1 are used to estimate the imbalance present in the setup electronics.

Electrode	QQ1 (V_{pp})		QQ2 (V_{pp})		QQ3 (V_{pp})	
Phase	a	b	a	b	a	b
Voltage	135.63	136.47	135.29	136.20	135.56	136.46
Pair Ratio (%)	0.62		0.67		0.60	
Segment Ratio (%)	0.25		0.20			

Table 5.1: RF amplitude measurements for QMF quadrupoles. The imbalance in the RF potentials of the three QMF quadrupole segments is compared using percentage difference of their peak-peak RF amplitudes.

The measurements in Table 5.1 shows the deviations in the RF amplitude is constrained to be within 1%. This is small compared to the imbalance required to cause losses according to simulation results of Section 4.2.2. Hence the LPT electronics are ready for operation without any correction required to balance the quadrupole RF potentials.

5.1.2 Switched DC ringing

The second electronic components to be tested are the voltage switches, used for providing switched DC voltage to the buncher for ion trapping and ejection. These voltage switches were designed to operate within the kV range and feature very fast switching upon receiving the square pulse signal (3.3 V) from FPGA. A ringing is observed in the switch-output, which lasts under 0.5 μs as shown in Fig. 5.1, which would affect the integrity of the ion bunch. Thus, potentiometers are added to the output of the switches to reduce the ringing. This results in a comparatively slower rise time of the order of $(0.2 - 0.3)\,\mu$s. Simulations were

done to observe the effects of rise time on the ion bunch, which concluded that a rise time $(< 1)\,\mu$s meets the ion bunch requirements for the MRTOF-MS.

Figure 5.1: Ringing in the output of the LPT voltage switch. The waveform in orange is the 3.3 V input for the voltage switch, and in purple is the output of the voltage switch which shows ∼44% overshoot when switching.

5.2 Ion Transmission Efficiency

During commissioning, the LPT setup is tested using ions produced by the ion source assembly. Since ions are thermally produced, they do not have any distinct timing signature to indicate their production time. Hence they need to be collected at an element inside the chamber, and the corresponding current is read by a multimeter sensitive to currents in the pA range. Fig. 5.2 shows the setup used for measuring an ion current on ion source and LPT elements. In the figure, ML1 is connected to a digital multimeter (34465A

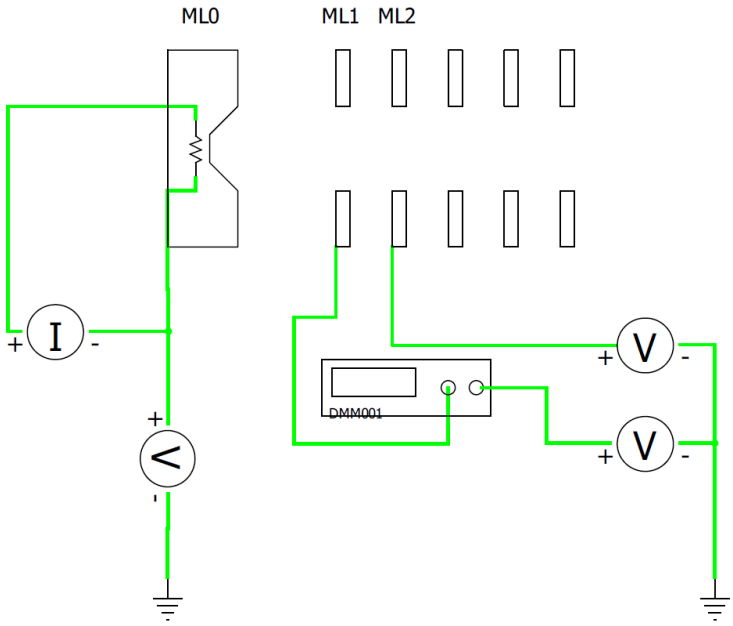

Figure 5.2: Schematic of the setup for testing ion transmission through ion current measurements at different electrodes. The electrode being measured is biased to a negative potential (shown here, ML1) to collect the ions, while the next electrode (here, ML2) is set to a high potential to block off the ions from passing through. Current from the ions collected is then measured using a digital multimeter which is sensitive to pA range currents.

Digital Multimeter, Keysight) for the current readout. Additionally, it is biased to a negative potential of -25 V using a voltage source (NGE103B power supply, Rhode & Schwarz). Ions are blocked beyond ML2 by setting ML2 voltage to greater than the ion energy (∼11.4 eV). Thus, all ions produced at ML0 are expected to be collected at ML1, where they are readout. A similar procedure is adopted for testing all elements. Using voltage settings obtained from simulations (Fig. 4.2), ion transmission efficiency is estimated between different electrodes, assuming constant ion production.

During tests, the source is first heated up to produce a steady ion current. The ion source requires a current supply for ohmic heating of the source material. Ions are generated when the source material reaches a certain temperature. Through multiple runs, it was found that

ion emission starts at approximately 2.8 A. The source quickly heats up and starts emitting ions at this supply current, as shown by the rising curve in Fig. 5.3. Since the high currents reduce the longevity of the source, once the ion current starts, the supply is lowered to 2.4 A. At this supply current, the ion current initially drops and later stabilizes after about 30 min. of operation with minimal increase in current overtime.

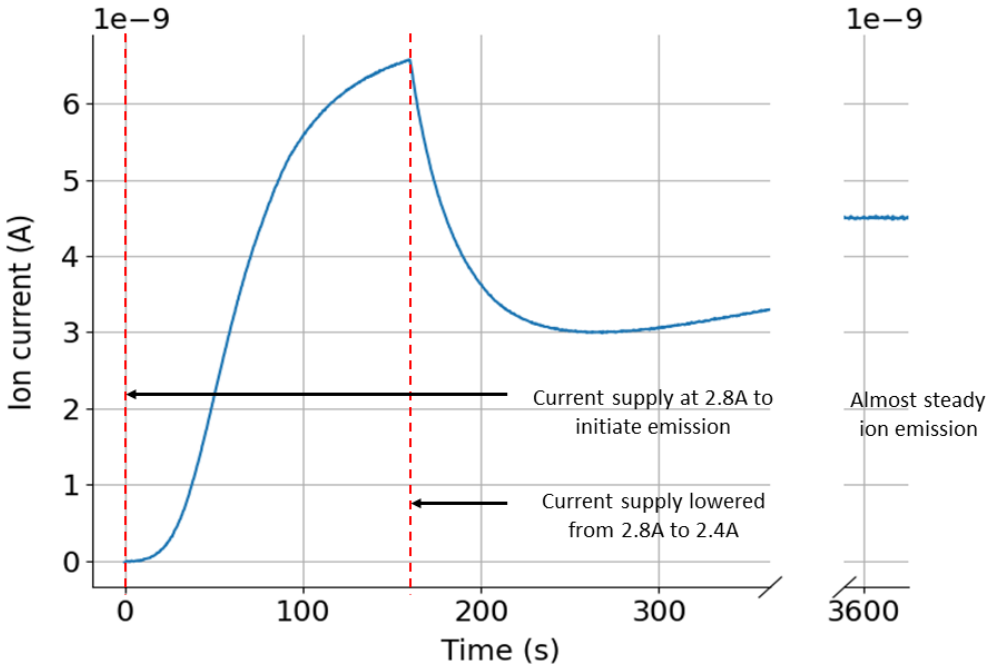

Figure 5.3: Ion current measurement at bender electrode 'ML7' taken during the heating up of the ion source. The ion source starts producing ions when supplied by a current of ∼2.8 A. Once ion production starts, the current is lowered, and ion production is allowed to stabilize before beginning use.

The measurement setup shown in Fig. 5.2 results in incorrect ion current measurements for some elements inside the LPT setup due to the RF voltage being induced onto the electrode being measured. This results in an offset in the measurements by the digital multimeter. The measured offset scales with the RF amplitude and shows variation with frequency making it difficult to calibrate the multimeter readings. An example of such offset

is a measured current of -5 nA on QQ3 aperture when QMF is running at 40 V_{pp} (1 MHz) RF voltage, which is several times greater than the nominal ion current. Fig. 5.4 shows a circuit designed by Eamon Egan, used to filter the induced RF potential before the current is measured by the multimeter. The measured current is then found equal to the measurement done in the absence of RF potential.

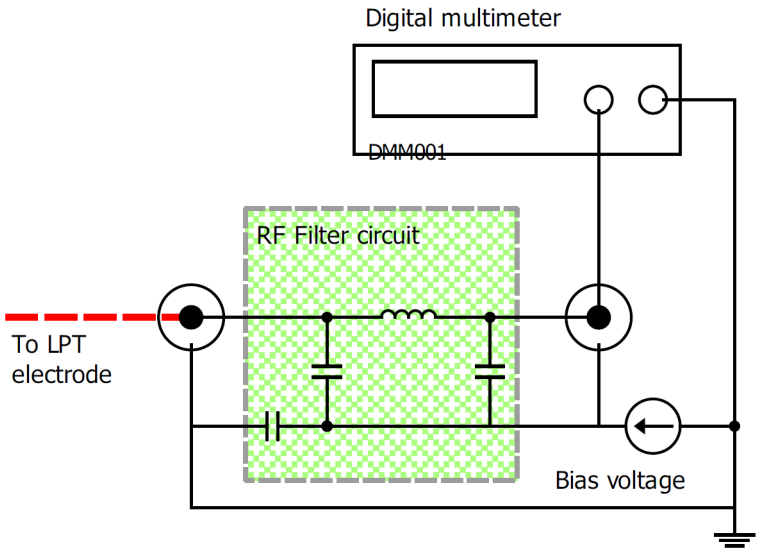

Figure 5.4: Electronic schematic of the circuit used for ion current measurements. The RF filter circuit removes the induced RF signal otherwise picked up from the neighboring quadrupole elements.

Fig. 5.5 shows ion current measurements taken at different electrodes inside the LPT setup. The highest current is measured at the ML1 lens, where almost all ions are expected to be collected. The ion current is then almost constant in the lens assembly (ML1 to ML5). Ions are then measured in the bender at electrodes ML7 or ML8 by biasing it to negative potential and setting all other electrodes to ground potential. Fig. 5.3 showed the current measured at ML7, which is lower than that measured at ML1, possibly due to losses upon entry to the bender through the slit. The ions are then passed through the bender with electrodes voltages set as shown in Fig. 4.2 and ion current measured at the entrance of

the QMF. Major losses occur between the bender and LPT due to the long drift region. Subsequently, only about 0.41 nA, which is ∼10% of the total current, makes it into the LPT setup. The ion current then measured along the LPT axis is found to remain constant.

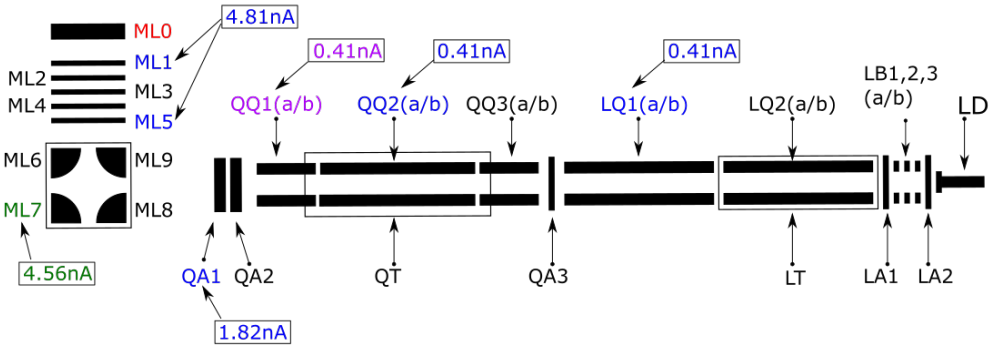

Figure 5.5: LPT schematic showing averaged ion current measurement at different electrodes during a ion transmission test run.

5.3 QMF Tests

The QMF was tested using the Cs-133 ion source. The theory developed in Section 2.1 is applied here to verify the performance by scanning the stable trajectory parameter space. This was investigated in Section 4.2 through SIMION simulation of the LPT setup.

For rod spacing of 7 mm, a frequency of 750 kHz, and a Cs-133 source (m=133 u), the voltages are related to the stability parameters as follows:

$$U = a \times (83.22\,\mathrm{V}) \times f^2(\mathrm{MHz}), \tag{5.1}$$

$$V = q \times (166.43\,\mathrm{V}) \times f^2(\mathrm{MHz}). \tag{5.2}$$

The DC (U) and RF (V) voltages for the QMF are varied using a LabVIEW program scanning over a range of (a, q) values belonging to the stability region shown in Fig. 2.5b. As the voltages (U, V) are varied, the ion current is measured using the circuit shown in Fig. 5.4

collecting ions at the pre-cooler (LQ1). After every voltage step, the ion current is given a window of a minimum of two seconds to stabilize, after which current measurements are recorded over the next 5 sec. The averaged current over this window is then recorded as a measurement value for that step and fluctuations to calculate the standard deviation.

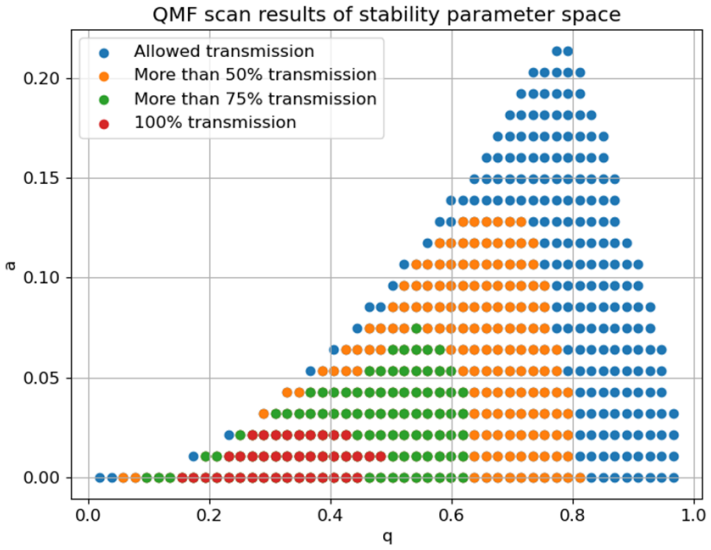

Figure 5.6: Plot showing results from the scanning of QMF voltages. Regions with different transmission efficiency are highlighted. The percentage transmission is calculated relative to the maximum measured ion current (0.41 nA) as reference. Points with average ion currents lower than 5 pA ($\approx$ fluctuations in ion current) are excluded from the stability region.

Fig. 5.6 shows the result of a scan of stability region for the QMF, with different levels of ion transport efficiencies highlighted, same as Fig. 4.3. Lower RF amplitudes corresponding to small q values (Eqn. 5.2) have higher transmission than high amplitudes, similar to the trend seen in Fig. 4.3. In Fig. 5.7a the results from simulated and experiment data are compared. While the general region is quite similar, the experiment data shows a shift to higher q values than the simulation. Comparing measurements of RF amplitude output from QMF-box and output of waveform generator, the gain in amplitude is ($G \approx 181$) over the entire range of the q parameter.

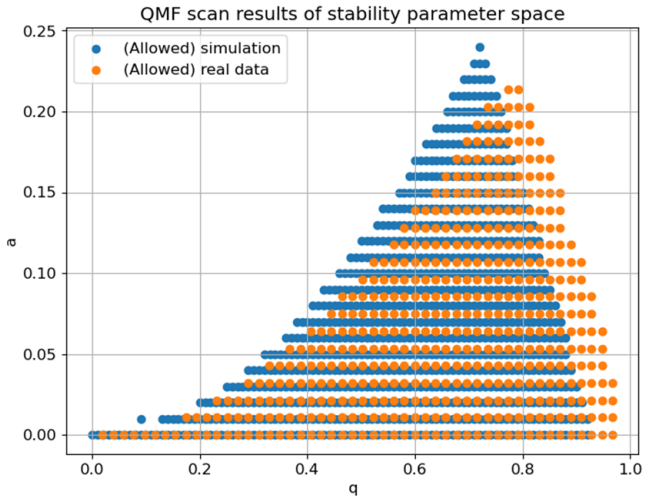

(a) The stability region from QMF scan data showing deviation from the region expected region from simulations. In yellow is data collected from scanning DC and RF voltages of the QMF, and (blue) are points from SIMION simulations done using the model of the QMF.

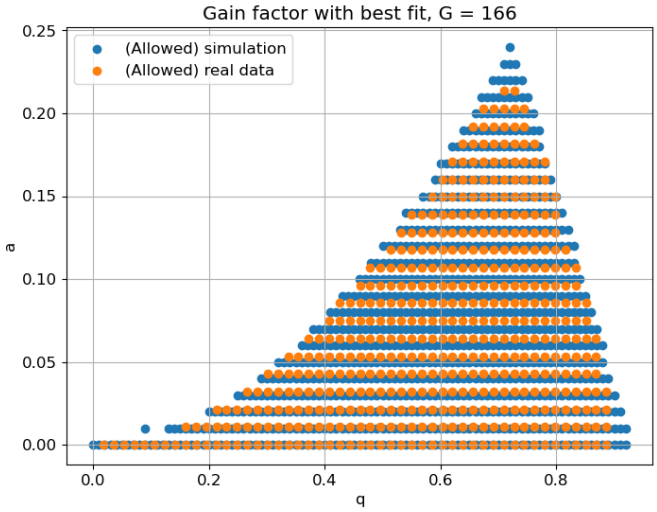

(b) Plot showing stability region of data after gain correction compared with simulation data. The distortion along the q parameter axis is corrected by modifying the gain factor when calculating q from corresponding RF amplitude.

Figure 5.7: Plots comparing QMF scan data with simulation from Section 4.2.

A possible source for the shift could be the overestimation of the gain. When trying to fit data with different values of gain, $G = 166$ corrects the distortion as shown in Fig. 5.7b. This could mean that the gain was either overestimated due to some reflection in the coaxial cable, or the gain of the amplifier may be dropping upon being fully loaded. This requires further investigation. However, from the map of stable parameters, a suitable operation voltage can be chosen to start filtering ions.

Chapter 6

Summary and Future Outlook

Neutrinoless double-beta decay is a weak process that may help unravel some of the secrets of the elusive neutrinos. Next-generation experiments hope to determine the nature of neutrinos as either Dirac or Majorana while extracting its absolute mass scale [44]. Due to the rare nature of this phenomenon, if it exists at all, large detector volumes with very low backgrounds are required.

The venture of tagging barium ions for background reduction in LXe detectors started with its conception in 1991 [57], to the current development of the technique for a proposed nEXO upgrade. This thesis outlines the efforts in the commissioning of a linear Paul trap which is a part of Ba-tagging development for the nEXO experiment. The LPT setup is being developed for the detection of the $0\nu\beta\beta$ and $2\nu\beta\beta$ decay product ^{136}Ba which has previously been extracted from the xenon-filled detector volume. The setup is currently being commissioned at McGill University by the author and other group members at the Brunner Neutrino Lab (Bnl). A 100% efficient Ba-tagging would result in a factor four improvement on the nEXO sensitivity to $0\nu\beta\beta$ decay half-life [56].

The theory describing the operation of radio-frequency ion guides is discussed with a focus on ion trajectory stability in Section 2.1. The stability is then used to describe the

operation of the QMF. Design and operation for all the different section of the LPT setup were discussed in detail along with electronics used. The time sequencing of switched voltages of the buncher are described in details along with pulse duration of TRANSFER (300 μs) and EJECT (100 μs) pulses for a net operation cycle time of 1 ms. The ion source assembly and LPT setup were modelled in SIMION 8.1 to optimize operating potentials of the electrodes for maximum possible transport efficiency of ions. Using the LPT setup simulation model, ion transmission efficiency of the QMF as a function of trajectory parameters was studied. The stability region obtained from the simulation showed good agreement from theoretical calculations. Simulations were also used to study the effect of RF voltage imbalance in a quadrupole. Results showed losses in ion transmission for a phase difference of more than 35° between adjacent quadrupoles, while within a quadrupole losses occur only beyond 60° phase difference.

Finally, preliminary tests were performed to characterize the functioning of the electronics and LPT setup as a whole. All electronics involved are tested for the quality of RF and switched signals. Imbalance in RF voltage measured for the QMF quadrupoles was found to be under 1%, which is much lower that the imbalance required to cause instability in ion trajectory. Additionally, ringing is observed in the switched voltages, which are compensated by the addition of potentiometers resulting in a slower rise time of about 200 ns compared to the $\sim$ 20 ns rise time with ringing. This rise time is still under 1 μs, which according to simulations of the MRTOF-MS [92] is small enough for the integrity of the ion bunches being ejected. The ion source assembly has been simulated and characterized with respect to ion production rate, optimal operating conditions for the thermal source, and net ion beam current entering the LPT setup. Although the source can produce a surplus of ions (max $\sim$30 nA recorded), there are significant internal losses in the large drift region between the quadrupole bender and QMF entrance. This is planned to be corrected by the addition of another Einzel lens after the 90° ion bender. The QMF is fully tested with a steady ion current of 0.41 nA supplied by the ion source. Results from a complete stability region scan

of the QMF show some deviation from simulations, which are later corrected by introducing a scale factor. The source of the factor is suspected to be related to the amplifier gain but needs further investigation for a definitive conclusion.

The goal of all these efforts is to study the extraction efficiency of barium ions from xenon gas and investigate the applicability of the Ba-tagging technique for a future nEXO upgrade. The future outlook of the project is to characterize the operation of the cooler and the buncher with helium buffer gas and study the bunching and ejection of ions. Once this study is completed, the setup will be operated in tandem with the upstream RF funnel, used for extracting barium ions from high pressures, and the downstream MRTOF-MS used for mass determination. Both devices are currently being developed in parallel.

Bibliography

[1] J. N. Bahcall, "How the sun shines," *arXiv preprint astro-ph/0009259*, 2000.

[2] S. E. Ramlo, "The Elusive Neutrino: A Subatomic Detective Story, by Nickolas Solomey," *The Physics Teacher*, vol. 37, pp. 503–503, Nov. 1999.

[3] K. Winter, "Neutrino physics," *Neutrino Physics*, 2008.

[4] P. Lipari, "Introduction to neutrino physics," *CERN European Organization for Nuclear Research-Reports-CERN*, no. 3, pp. 115–200, 2003.

[5] A. Franckowiak, "Multimessenger astronomy with neutrinos," in *Journal of Physics: Conference Series*, vol. 888, p. 012009, IOP Publishing, 2017.

[6] G. Fiorentini, M. Lissia, and F. Mantovani, "Geo-neutrinos and earth's interior," *Physics Reports*, vol. 453, no. 5-6, pp. 117–172, 2007.

[7] S. Bilenky, "Neutrino. History of a unique particle," *The European Physical Journal H*, vol. 38, no. 3, pp. 345–404, 2013.

[8] F. Reines and C. Cowan, "The Reines-Cowan experiments: Detecting the Poltergeist," *Los Alamos Science*, vol. 25, pp. 4–27, 1997.

[9] J. Steinberger, "The discovery of the second neutrino; La decouverte du second neutrino," *Bulletin de l'Union des Physiciens*, vol. 91, 1997.

[10] U. Dore, P. Loverre, and L. Ludovici, "History of accelerator neutrino beams," *The European Physical Journal H*, vol. 44, no. 4, pp. 271–305, 2019.

[11] M. L. Perl, "The Discovery of the tau lepton," *SLAC-PUB–5937*, 1992.

[12] R. Davis, "A review of the Homestake solar neutrino experiment," *Progress in Particle and Nuclear Physics*, vol. 32, pp. 13–32, 1994.

[13] W. Haxton, "The solar neutrino problem," *Annual Review of Astronomy and Astrophysics*, vol. 33, no. 1, pp. 459–503, 1995.

[14] K. S. Hirata, T. Kajita, T. Kifune, K. Kihara, M. Nakahata, K. Nakamura, S. Ohara, Y. Oyama, N. Sato, M. Takita, *et al.*, "Observation of B-8 solar neutrinos in the Kamiokande-II Detector," *Physical Review Letters*, vol. 63, no. 1, p. 16, 1989.

[15] Y. Fukuda, T. Hayakawa, E. Ichihara, K. Inoue, K. Ishihara, H. Ishino, Y. Itow, T. Kajita, J. Kameda, S. Kasuga, *et al.*, "Measurement of the flux and zenith-angle distribution of upward throughgoing muons by Super-Kamiokande," *Physical Review Letters*, vol. 82, no. 13, p. 2644, 1999.

[16] K. Eguchi, S. Enomoto, K. Furuno, J. Goldman, H. Hanada, H. Ikeda, K. Ikeda, K. Inoue, K. Ishihara, W. Itoh, *et al.*, "First results from KamLAND: evidence for reactor antineutrino disappearance," *Physical Review Letters*, vol. 90, no. 2, p. 021802, 2003.

[17] Q. R. Ahmad, R. Allen, T. Andersen, J. Anglin, J. Barton, E. Beier, M. Bercovitch, J. Bigu, S. Biller, R. Black, *et al.*, "Direct evidence for neutrino flavor transformation from neutral-current interactions in the Sudbury Neutrino Observatory," *Physical Review Letters*, vol. 89, no. 1, p. 011301, 2002.

[18] C. Giganti, S. Lavignac, and M. Zito, "Neutrino oscillations: the rise of the PMNS paradigm," *Progress in Particle and Nuclear Physics*, vol. 98, pp. 1–54, 2018.

[19] M. Tanabashi, K. Hagiwara, K. Hikasa, K. Nakamura, Y. Sumino, F. Takahashi, J. Tanaka, K. Agashe, G. Aielli, C. Amsler, *et al.*, "Review of particle physics," *Physical Review D*, vol. 98, no. 3, p. 030001, 2018.

[20] G. Drexlin, Katrin Collaboration, *et al.*, "KATRIN-direct measurement of a sub-eV neutrino mass," *Nuclear Physics B-Proceedings Supplements*, vol. 145, pp. 263–267, 2005.

[21] K. J. Kelly, P. A. Machado, S. J. Parke, Y. F. Perez-Gonzalez, and R. Z. Funchal, "Neutrino mass ordering in light of recent data," *Physical Review D*, vol. 103, no. 1, p. 013004, 2021.

[22] S. M. Bilenky and B. Pontecorvo, "Lepton mixing and neutrino oscillations," *Physics Reports*, vol. 41, no. 4, pp. 225–261, 1978.

[23] S. M. Bilenky and S. Petcov, "Massive neutrinos and neutrino oscillations," *Reviews of Modern Physics*, vol. 59, no. 3, p. 671, 1987.

[24] M. Dolinsky, "Neutrino Physics, Day 1," *TRISEP 2021*, 2021.

[25] M. Ahn, E. Aliu, S. Andringa, S. Aoki, Y. Aoyama, J. Argyriades, K. Asakura, R. Ashie, F. Berghaus, H. Berns, *et al.*, "Measurement of neutrino oscillation by the K2K experiment," *Physical Review D*, vol. 74, no. 7, p. 072003, 2006.

[26] J. Evans, "The MINOS experiment: results and prospects," *Advances in High Energy Physics*, vol. 2013, 2013.

[27] K. Abe, N. Abgrall, H. Aihara, Y. Ajima, J. Albert, D. Allan, P.-A. Amaudruz, C. Andreopoulos, B. Andrieu, M. Anerella, *et al.*, "The T2K experiment," *Nuclear Instruments and Methods in Physics Research Section A: Accelerators, Spectrometers, Detectors and Associated Equipment*, vol. 659, no. 1, pp. 106–135, 2011.

[28] F. An, J. Bai, A. Balantekin, H. Band, D. Beavis, W. Beriguete, M. Bishai, S. Blyth, K. Boddy, R. Brown, *et al.*, "Observation of electron-antineutrino disappearance at Daya Bay," *Physical Review Letters*, vol. 108, no. 17, p. 171803, 2012.

[29] M. Acero, P. Adamson, L. Aliaga, T. Alion, V. Allakhverdian, N. Anfimov, A. Antoshkin, E. Arrieta-Diaz, A. Aurisano, A. Back, *et al.*, "New constraints on oscillation parameters from ν_e appearance and ν_μ disappearance in the NOvA experiment," *Physical Review D*, vol. 98, no. 3, p. 032012, 2018.

[30] N. Aghanim, Y. Akrami, M. Ashdown, J. Aumont, C. Baccigalupi, M. Ballardini, A. Banday, R. Barreiro, N. Bartolo, S. Basak, *et al.*, "Planck 2018 results-VI. Cosmological parameters," *Astronomy & Astrophysics*, vol. 641, p. A6, 2020.

[31] S. F. King, "Neutrino mass models," *Reports on Progress in Physics*, vol. 67, no. 2, p. 107, 2003.

[32] S. Bilenky, "Neutrino in Standard Model and Beyond," *Physics of Particles and Nuclei*, vol. 46, no. 4, pp. 475–496, 2015.

[33] S. M. Bilenky and S. Petcov, "Massive neutrinos and neutrino oscillations," *Reviews of Modern Physics*, vol. 59, no. 3, p. 671, 1987.

[34] G. Gratta and N. Kurahashi, "In search of no neutrinos," *Physics World*, vol. 23, pp. 27–30, apr 2010.

[35] V. I. Tretyak and Y. G. Zdesenko, "Tables of double beta decay data—an update," *Atomic Data and Nuclear Data Tables*, vol. 80, no. 1, pp. 83–116, 2002.

[36] K. Asakura *et al.*, "Search for double-beta decay of ^{136}Xe to excited states of ^{136}Ba with the KamLAND-Zen experiment," *Nuclear Physics A*, vol. 946, pp. 171 – 181, 2016.

[37] F. F. Deppisch, M. Hirsch, and H. Päs, "Neutrinoless double-beta decay and physics beyond the standard model," *Journal of Physics G: Nuclear and Particle Physics*, vol. 39, no. 12, p. 124007, 2012.

[38] L. Canetti, M. Drewes, and M. Shaposhnikov, "Matter and Antimatter in the Universe," *New Journal of Physics*, vol. 14, no. 9, p. 095012, 2012.

[39] M. Agostini, G. Araujo, A. Bakalyarov, M. Balata, I. Barabanov, L. Baudis, C. Bauer, E. Bellotti, S. Belogurov, A. Bettini, *et al.*, "Final results of GERDA on the search for neutrinoless double-β decay," *Physical Review Letters*, vol. 125, no. 25, p. 252502, 2020.

[40] J. Albert, D. Auty, P. Barbeau, E. Beauchamp, D. Beck, V. Belov, C. Benitez-Medina, J. Bonatt, M. Breidenbach, T. Brunner, *et al.*, "Search for Majorana neutrinos with the first two years of EXO-200 data," *arXiv preprint arXiv:1402.6956*, 2014.

[41] S. Umehara, T. Kishimoto, I. Ogawa, R. Hazama, H. Miyawaki, S. Yoshida, K. Matsuoka, K. Kishimoto, A. Katsuki, H. Sakai, *et al.*, "Neutrino-less double-β decay of ^{48}Ca studied by CaF_2 (Eu) scintillators," *Physical Review C*, vol. 78, no. 5, p. 058501, 2008.

[42] D. Adams, C. Alduino, K. Alfonso, F. Avignone III, O. Azzolini, G. Bari, F. Bellini, G. Benato, M. Beretta, M. Biassoni, *et al.*, "High sensitivity neutrinoless double-beta decay search with one tonne-year of CUORE data," *arXiv preprint arXiv:2104.06906*, 2021.

[43] G. Anton, I. Badhrees, P. Barbeau, D. Beck, V. Belov, T. Bhatta, M. Breidenbach, T. Brunner, G. Cao, W. Cen, *et al.*, "Search for neutrinoless double-β decay with the complete EXO-200 dataset," *Physical Review Letters*, vol. 123, no. 16, p. 161802, 2019.

[44] Dolinski, Michelle J. and Poon, Alan W.P. and Rodejohann, Werner, "Neutrinoless double-beta decay: Status and prospects," *Annual Review of Nuclear and Particle Science*, vol. 69, no. 1, pp. 219–251, 2019.

[45] J. Kotila and F. Iachello, "Phase-space factors for double-β decay," *Physical Review C*, vol. 85, no. 3, p. 034316, 2012.

[46] S. Stoica and M. Mirea, "New calculations for phase space factors involved in double-β decay," *Physical Review C*, vol. 88, no. 3, p. 037303, 2013.

[47] S. A. Kharusi, A. Alamre, J. Albert, M. Alfaris, G. Anton, I. Arnquist, I. Badhrees, P. Barbeau, D. Beck, V. Belov, *et al.*, "nEXO pre-conceptual design report," *arXiv preprint arXiv:1805.11142*, 2018.

[48] R. Ford, "Snolab: Review of the facility and experiments," in *AIP Conference Proceedings*, vol. 1441, pp. 521–524, American Institute of Physics, 2012.

[49] T. Stiegler, S. Sangiorgio, J. Brodsky, M. Heffner, S. Al Kharusi, G. Anton, I. Arnquist, I. Badhrees, P. Barbeau, D. Beck, *et al.*, "Event reconstruction in a liquid xenon Time Projection Chamber with an optically-open field cage," *Nuclear Instruments and Methods in Physics Research Section A: Accelerators, Spectrometers, Detectors and Associated Equipment*, p. 165239, 2021.

[50] E. Aprile and T. Doke, "Liquid xenon detectors for particle physics and astrophysics," *Reviews of Modern Physics*, vol. 82, no. 3, p. 2053, 2010.

[51] M. Wagenpfeil, T. Ziegler, A. Fieguth, J. Schneider, T. Michel, and C. Weinheimer, "Reflectance of VUV-sensitive SiPM surfaces in liquid xenon," *Nuclear Instruments and Methods in Physics Research Section A: Accelerators, Spectrometers, Detectors and Associated Equipment*, vol. 936, pp. 577–579, 2019.

[52] J. Albert, P. Barbeau, D. Beck, V. Belov, M. Breidenbach, T. Brunner, A. Burenkov, G. Cao, W. Cen, C. Chambers, *et al.*, "Measurement of the drift velocity and transverse diffusion of electrons in liquid xenon with the EXO-200 detector," *Physical Review C*, vol. 95, no. 2, p. 025502, 2017.

[53] O. Njoya, T. Tsang, M. Tarka, W. Fairbank, K. Kumar, T. Rao, T. Wager, S. Al Kharusi, G. Anton, I. J. Arnquist, *et al.*, "Measurements of electron transport in liquid and gas Xenon using a laser-driven photocathode," *Nuclear Instruments and Methods in Physics Research Section A: Accelerators, Spectrometers, Detectors and Associated Equipment*, vol. 972, p. 163965, 2020.

[54] G. Adhikari, S. A. Kharusi, E. Angelico, G. Anton, I. Arnquist, I. Badhrees, J. Bane, V. Belov, E. Bernard, T. Bhatta, *et al.*, "nEXO: Neutrinoless double beta decay search beyond 10^{28} year half-life sensitivity," *arXiv preprint arXiv:2106.16243*, 2021.

[55] E. Conti, R. DeVoe, G. Gratta, T. Koffas, S. Waldman, J. Wodin, D. Akimov, G. Bower, M. Breidenbach, R. Conley, *et al.*, "Correlated fluctuations between luminescence and ionization in liquid xenon," *Physical Review B*, vol. 68, no. 5, p. 054201, 2003.

[56] J. Albert, G. Anton, I. Arnquist, I. Badhrees, P. Barbeau, D. Beck, V. Belov, F. Bourque, J. Brodsky, E. Brown, *et al.*, "Sensitivity and discovery potential of the proposed nEXO experiment to neutrinoless double-β decay," *Physical Review C*, vol. 97, no. 6, p. 065503, 2018.

[57] M. Moe, "Detection of neutrinoless double-beta decay," *Physical Review C*, vol. 44, no. 3, p. R931, 1991.

[58] Neuhauser, W and Hohenstatt, M and Toschek, PE and Dehmelt, H, "Localized visible Ba^+ mono-ion oscillator," *Physical Review A*, vol. 22, no. 3, p. 1137, 1980.

[59] M. Green, J. Wodin, R. DeVoe, P. Fierlinger, B. Flatt, G. Gratta, F. LePort, M. M. Díez, R. Neilson, K. O'Sullivan, *et al.*, "Observation of single collisionally cooled trapped ions in a buffer gas," *Physical Review A*, vol. 76, no. 2, p. 023404, 2007.

[60] R. S. Killick, *Observation of Singly Charged Barium Ions in a Buffer Gas: Towards a Functional Barium-Tagging System for Use in the Enriched Xenon Observatory*. PhD thesis, Carleton University, 2015.

[61] T. Brunner, D. Fudenberg, V. Varentsov, A. Sabourov, G. Gratta, J. Dilling, R. DeVoe, D. Sinclair, W. Fairbank Jr, J. B. Albert, *et al.*, "An RF-only ion-funnel for extraction from high-pressure gases," *International Journal of Mass Spectrometry*, vol. 379, pp. 110–120, 2015.

[62] K. Twelker, S. Kravitz, M. M. Díez, G. Gratta, W. Fairbank Jr, J. Albert, D. Auty, P. Barbeau, D. Beck, C. Benitez-Medina, *et al.*, "An apparatus to manipulate and identify individual Ba ions from bulk liquid Xe," *Review of Scientific Instruments*, vol. 85, no. 9, p. 095114, 2014.

[63] C. Chambers, T. Walton, D. Fairbank, A. Craycraft, D. Yahne, J. Todd, A. Iverson, W. Fairbank, A. Alamare, J. Albert, *et al.*, "Imaging individual barium atoms in solid xenon for barium tagging in nEXO," *Nature*, vol. 569, no. 7755, pp. 203–207, 2019.

[64] B. Mong, S. Cook, T. Walton, C. Chambers, A. Craycraft, C. Benitez-Medina, K. Hall, W. Fairbank Jr, J. Albert, D. Auty, *et al.*, "Spectroscopy of Ba and Ba^+ deposits in solid xenon for barium tagging in nEXO," *Physical Review A*, vol. 91, no. 2, p. 022505, 2015.

[65] N. Byrnes, A. Denisenko, F. Foss Jr, B. Jones, A. McDonald, D. Nygren, P. Thapa, and K. Woodruff, "Barium tagging with selective, dry-functional, single molecule sensitive on-off fluorophores for the next experiment," *arXiv preprint arXiv:1909.04677*, 2019.

[66] K. Murray, J. Dilling, R. Gornea, Y. Ito, T. Koffas, A. Kwiatkowski, Y. Lan, M. Reiter, V. Varentsov, and T. Brunner, "Design of a multiple-reflection time-of-flight mass spectrometer for barium-tagging," *Hyperfine Interactions*, vol. 240, no. 1, pp. 1–9, 2019.

[67] M. H. Holzscheiter, "A brief history in time of ion traps and their achievements in science," *Physica Scripta*, vol. 1995, no. T59, p. 69, 1995.

[68] W. Paul, "Electromagnetic traps for charged and neutral particles," *Reviews of Modern Physics*, vol. 62, no. 3, p. 531, 1990.

[69] D. Kielpinski, C. Monroe, and D. J. Wineland, "Architecture for a large-scale ion-trap quantum computer," *Nature*, vol. 417, no. 6890, pp. 709–711, 2002.

[70] C. Baker, W. Bertsche, A. Capra, C. Carruth, C. Cesar, M. Charlton, A. Christensen, R. Collister, A. C. Mathad, S. Eriksson, *et al.*, "Laser cooling of antihydrogen atoms," *Nature*, vol. 592, no. 7852, pp. 35–42, 2021.

[71] D. J. Griffiths, *Introduction to electrodynamics*. Prentice Hall New Jersey, 1962.

[72] G. Werth, V. N. Gheorghe, and F. G. Major, *Charged particle traps II*. Springer, 2009.

[73] "Paul traps, Martina Knoop, CNRS/Université d'Aix-Marseille.." https://indico.cern.ch/event/315947/sessions/61194/attachments/606588/834751/Paul_traps_until_page_79.pdf. Last Accessed: 2021-08-19.

[74] S. Earnshaw, "On the nature of the molecular forces which regulate the constitution of the luminiferous ether," *Transactions of the Cambridge Philosophical Society*, vol. 7, p. 97, 1848.

[75] S. Schwarz, *Manipulation of Radioactive Ion Beams using a Paul Trap and Direct Mass Measurements of Neutron-Deficient Mercury Isotopes at the ISOLTRAP-Experiment*. PhD thesis, Fachbereich Physik der Johannes Gutenberg-Universitat, 1998.

[76] F. G. Major, V. N. Gheorghe, S. P. F. G. Major, G. Werth, G. Werth, *et al.*, *Charged particle traps: physics and techniques of charged particle field confinement*, vol. 37. Springer Science & Business Media, 2005.

[77] R. E. March and J. F. Todd, *Quadrupole ion trap mass spectrometry*, vol. 165. John Wiley & Sons, 2005.

[78] J. Campana, "Elementary theory of the quadrupole mass filter," *International Journal of Mass Spectrometry and Ion Physics*, vol. 33, no. 2, pp. 101–117, 1980.

[79] Y. Lan, *A linear Paul trap for barium tagging of neutrinoless double beta decay in nEXO*. PhD thesis, University of British Columbia, 2020.

[80] G. F. Brabeck and P. T. Reilly, "Computational analysis of quadrupole mass filters employing nontraditional waveforms," *Journal of The American Society for Mass Spectrometry*, vol. 27, no. 6, pp. 1122–1127, 2016.

[81] D. Douglas, "Linear quadrupoles in mass spectrometry," *Mass Spectrometry Reviews*, vol. 28, no. 6, pp. 937–960, 2009.

[82] J. Buon, "Beam phase space and emittance," tech. rep., Paris-11 Univ., 1992.

[83] A. Kellerbauer, T. Kim, R. Moore, and P. Varfalvy, "Buffer gas cooling of ion beams," *Nuclear Instruments and Methods in Physics Research Section A: Accelerators, Spectrometers, Detectors and Associated Equipment*, vol. 469, no. 2, pp. 276–285, 2001.

[84] F. Major and H. Dehmelt, "Exchange-collision technique for the rf spectroscopy of stored ions," *Physical Review*, vol. 170, no. 1, p. 91, 1968.

[85] T. Hasegawa and K. Uehara, "Dynamics of a single particle in a Paul trap in the presence of the damping force," *Applied Physics B*, vol. 61, no. 2, pp. 159–163, 1995.

[86] B. Wolf, *Handbook of ion sources*. CRC press, 1995.

[87] P. Mahaffy and K. Lai, "An electrostatic quadrupole deflector for mass spectrometer applications," *Journal of Vacuum Science & Technology A: Vacuum, Surfaces, and Films*, vol. 8, no. 4, pp. 3244–3246, 1990.

[88] D. Douglas and N. Konenkov, "Mass resolution of linear quadrupole ion traps with round rods," *Rapid Communications in Mass Spectrometry*, vol. 28, no. 21, pp. 2252–2258, 2014.

[89] B. Toftmann, J. Schou, and S. Canulescu, "Energy distribution of ions produced by laser ablation of silver in vacuum," *Applied Surface Science*, vol. 278, pp. 273–277, 2013.

[90] K. Murray, C. Chambers, D. Chen, Z. Feng, J. Fraser, Y. Ito, Y. Lan, S. Mendez, M. M. Peregrina, H. Rasiwala, *et al.*, "Characterization of a spatially resolved multi-element laser ablation ion source," *arXiv preprint arXiv:2108.10758*, 2021.

[91] P. Dawson, "Fringing fields in the quadrupole mass filter," *International Journal of Mass Spectrometry and Ion Physics*, vol. 6, no. 1-2, pp. 33–44, 1971.

[92] K. Murray, *The Design and Optimization of a Multi-Reflection Time-of-Flight Mass-Spectrometer for Barium Tagging with nEXO and Optimization of the ^{137}Xe veto with EXO-200*. PhD thesis, McGill University (Canada), 2018.

[93] C. Jesch, *The multiple-reflection time-of-flight isobar separator for TITAN and direct mass measurements at the FRS Ion Catcher*. PhD thesis, Justus-Liebig-Universität Gießen, 06 2016.

[94] "Potential Array, SIMION Online Supplemental documentation.." https://simion.com/info/potential_array.html. Last Accessed: 2021-08-19.

[95] H. Liebl, *Applied charged particle optics*, vol. 2012. Springer, 2008.

[96] X. Zhou, X. Liu, W. Cao, X. Wang, M. Li, H. Qiao, and Z. Ouyang, "Study of in-trap ion clouds by ion trajectory simulations," *Journal of The American Society for Mass Spectrometry*, vol. 29, no. 2, pp. 223–229, 2017.

[97] "Collision Model - HS1, SIMION Online Supplemental documentation.." https://simion.com/info/collision_model_hs1.html. Last Accessed: 2021-08-19.

[98] I. T. Jolliffe and J. Cadima, "Principal component analysis: A review and recent developments," *Philosophical Transactions of the Royal Society A: Mathematical, Physical and Engineering Sciences*, vol. 374, no. 2065, p. 20150202, 2016.

Appendices

Appendix A

Vacuum part cleaning protocol

In order to maintain a standard during the cleaning process, the following procedure is applied:

- Scrub and clean parts first with soap solution. Rinse with water and set parts to dry.
- Upon drying, place the parts in a clean tray and fill it with acetone until entire part is completely submerged[1]. Set the part to sonicate for 30 min.
- When the sonication stops, transfer acetone to the appropriate disposal container and fill the tray with either ethanol or isopropanol. Set the parts to sonicate for another 30 min.
- Transfer parts onto a fresh (KIMTECH) Kimwipe sheet or aluminium foil and use after alcohol has completely evaporated.

[1]Note: Check water level in the sonicator-machine, level should be above 'min' mark. Too much water should also be avoided as it may cause the tray to float

Appendix B

Commissioned electronics and circuitry

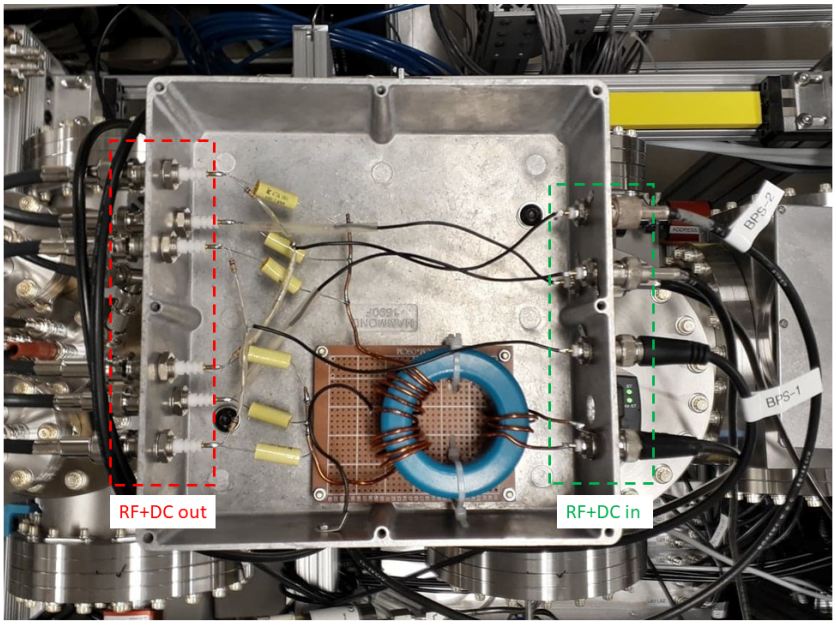

Figure B.1: Electronics for QMF electrodes housed inside a metal box for electric shielding from external interference/noise as well as preventing interference of other lab equipment from the QMF RF voltage.

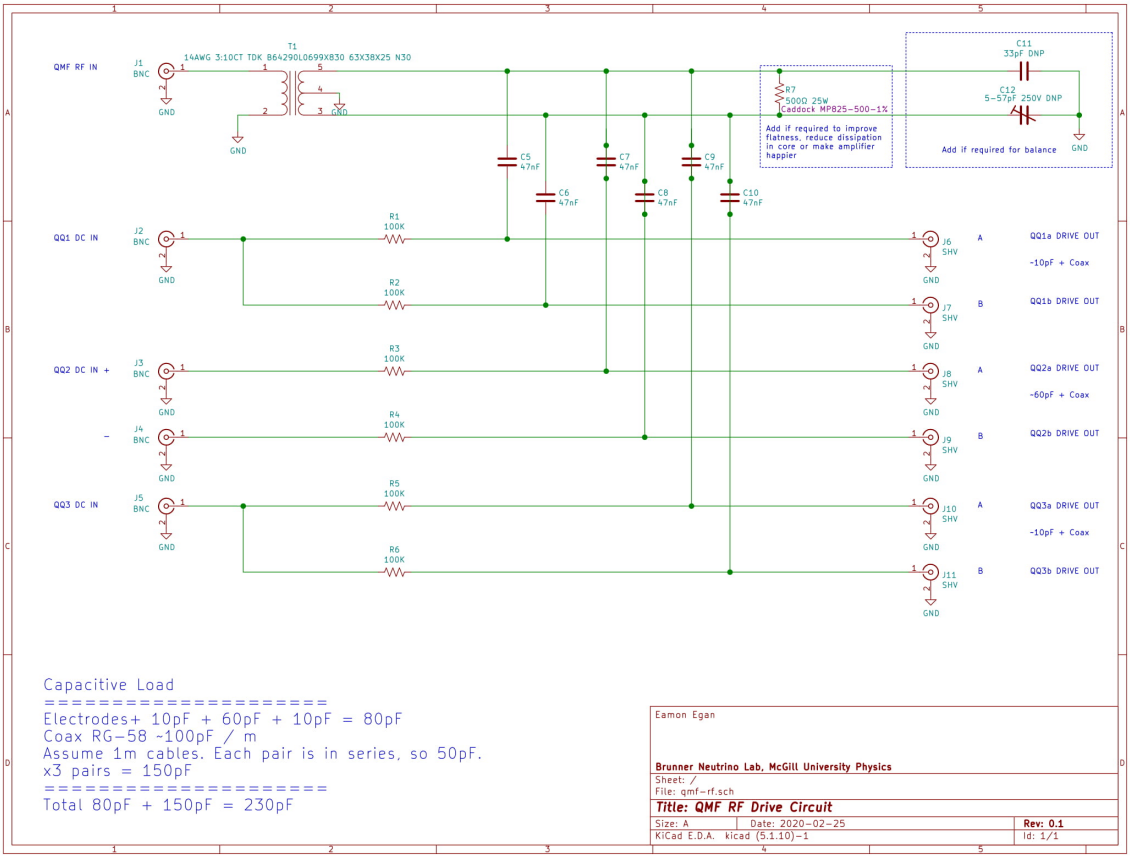

Figure B.2: Circuit diagram for the QMF-box. DC inputs on the left are coupled to the RF voltage separately for the different quadrupole segments. The filter segment, in particular, has differential DC and hence has two separate inputs, QQ2 DC IN (+/-).

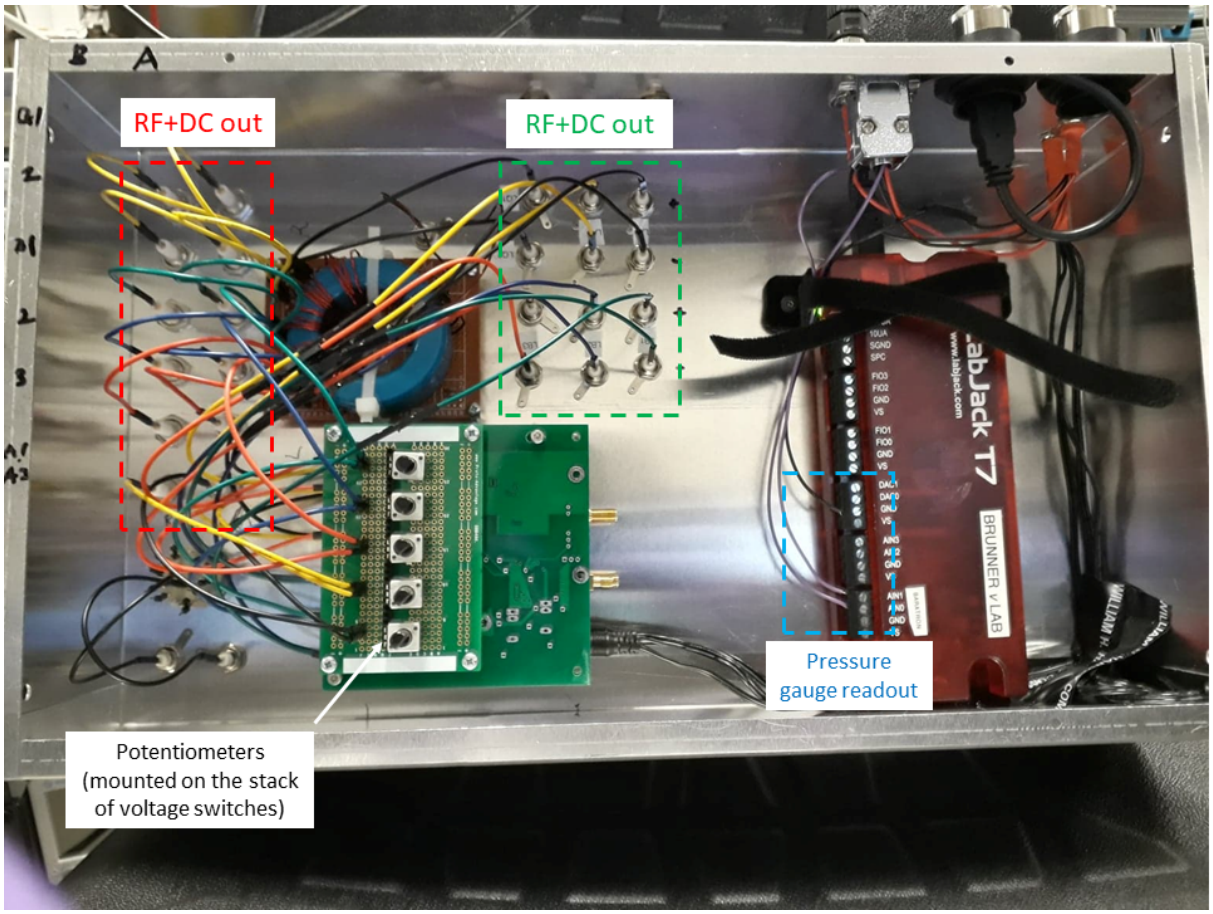

Figure B.3: Picture shows the ICB box which houses the electronics for cooler and buncher electrodes. The feedthroughs and bulkheads (M5, M8, USB2.0) are also visible towards the top right. The wires bundles connect the voltage switches to the DC voltage bulkheads (center) to the output (left side). The 5 potentiometers mounted on the stack of voltage switches are for reducing the ringing produced by the switches. Shown to the right is a LabJack T7 unit for data-acquisition from pressure gauges as well as scanning multiplexer channels of the monitoring circuit currently under development.

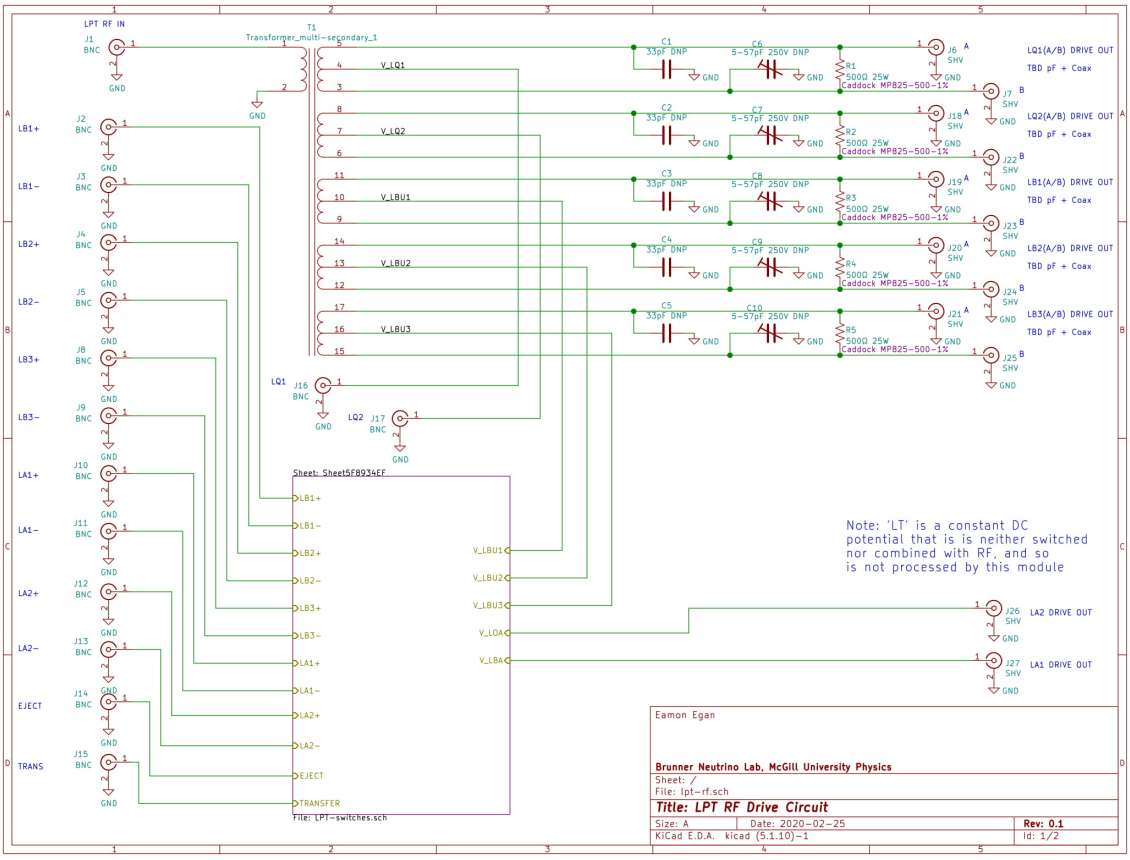

Figure B.4: Circuit diagram for the ICB-box. The ICB has many more DC inputs due to the switching of buncher electrode potentials. Switched DC voltages are supplied through the ICB voltage switches which are controlled by 'EJECT' and 'TRANS' signals from the FPGA. The control signals are discussed in detail in Section 3.4.

Appendix C

Pictures of ion source assembly

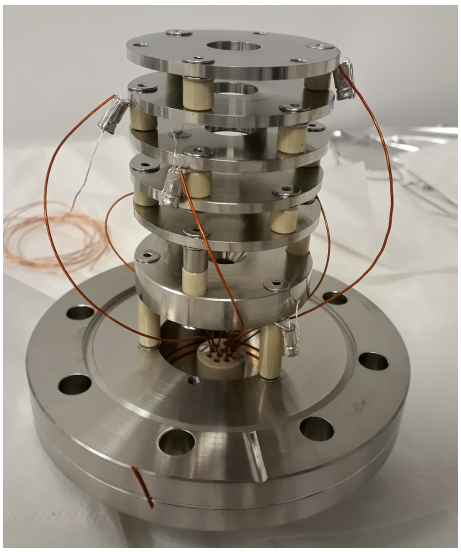

(a) Source assembly with 9-pin feedthrough installed in 4.5”-2.75” reducer flange. The source holder is mounted using tapped holes in the flange and ceramic standoffs are used to isolate the different elements.

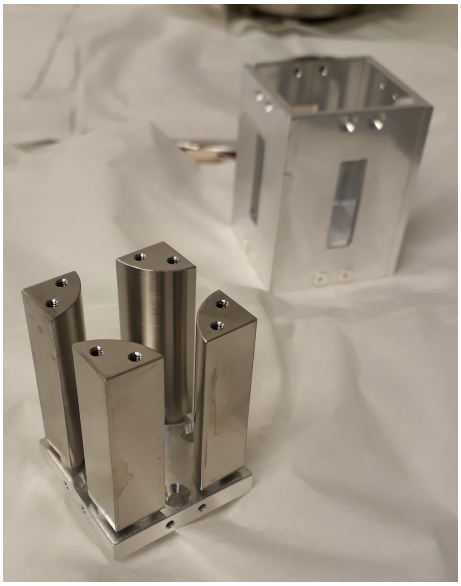

(b) Quadrupole bender and metal shielding box. Ceramic hat washers are used to insulate the bender electrodes from the shielding box.

Figure C.1: Photographs of ion source assembly and bender prior to assembly.

Appendix D

LPT electronics reference table

Electrode Description	Code	Voltage type	Voltage range (V)
Ion source assembly			
Source Holder	ML0	DC + current	10 to 15
Lens1	ML1	DC	-30 to -50
Lens2	ML2	DC	-30 to -50
Lens3	ML3	DC	0 to 5
Lens4	ML4	DC	-50 to -75
Lens5	ML5	DC	0 to 5
Bender			
Bender elec. 1	ML6	DC	0 to 20
Bender elec. 2	ML7	DC	-20 to -10
Bender elec. 3	ML8	DC	0 to 20
Bender elec. 4	ML9	DC	-30 to -10

Table D.1: Reference table for component description and their assigned codes. Also included is the operating voltage and voltage type of the electrodes.

Electrode Description	Code	Voltage type	Voltage range (V)
LPT - QMF			
Aperture1	QA1	DC	-50 to -20
Aperture2	QA2	DC	-50 to -20
Quad1 (ramp)	QQ1(a/b)	DC + RF	-20 to -10; upto $150V_{pp}$(0.75 MHz)
Quad2 (filter)	QQ2(a/b)	RF + DC (diff.)	-50 to 10; upto $150V_{pp}$(0.75 MHz)
Quad3 (ramp)	QQ3(a/b)	DC + RF	-20 to -10; upto $150V_{pp}$(0.75 MHz)
QMF shield	QT	DC	0 (ground potential)
Aperture3	QA3	DC	-20 to -10
LPT - ICB			
Pre-cooler	LQ1(a/b)	DC + RF	-20 to -10; upto $100V_{pp}$(1.0 MHz)
Cooler	LQ2(a/b)	DC + RF	-20 to -10; upto $100V_{pp}$(1.0 MHz)
Square tube	LT	DC	-100 to -50
Aperture1	LA1	Switched DC	10 to 20, -20 to -10 (transfer)
Buncher-Quad1	LB1(a/b)	Switched DC+RF	-20 to -10, 150 to 100 (eject); $100V_{pp}$ (1.0 MHz)
Buncher-Quad2	LB2(a/b)	Switched DC+RF	-20 to -10, -10 to 0 (eject); $100V_{pp}$ (1.0 MHz)
Buncher-Quad3	LB3(a/b)	Switched DC+RF	-20 to -10, 150 to 100 (eject); $100V_{pp}$ (1.0 MHz)
Aperture2	LA2	Switched DC	10 to 20, -150 to -100 (eject)
Drift-tube	LD	Switched DC	-150 to -100, 1500 to 1000 (eject)

Table D.2: Reference table for component description and their assigned codes (cont.). Also included is the operating voltage and voltage type of the electrodes.

Appendix E

List of hardware components

Code	Device Type, Name
Vacuum hardware	
TMP001(002)	Turbo molecular pump, HiPace 700, Pfeiffer Vacuum
FRG005(007)	Full range gauge, Pfeiffer Vacuum
PIR010	Pirani gauge, Pfeiffer Vacuum
OMG008/BPT009	Pressure transducers
Electronic equipment	
WFM-GEN	Waveform generator, T344 Highland Technology
RFA001(002)	RF Power Amplifier, 325LA ENI RF amplifier
VPS001(002)	High-voltage power supply, ISEG EBS C0 30
DMM001	34465A Digital Multimeter, Keysight
RSLV001(004)	NGE103B, Rhode & Schwarz power supply
–	DAQ hardware, LabJack T7
–	FAB-3226 FPGA

Table E.1: Complete list of hardware required for the operation of the LPT setup.